



Centre for
Advanced 2D Materials



MULTI-LAYER 2D NANOPORES FOR BLUE ENERGY HARVESTING: DESIGN, NANOFABRICATION AND NANOFLUIDIC TRANSPORT

Nanotechnologies for ICTs - Master Thesis - a.a "2019/2020"

Author: *Dario Bonincontro*

Supervisors:

Prof. Matteo Cocuzza (Polito)

Prof. Slaven Garaj (NUS)

Dr. Massimo Spina (NUS)

Co-supervisor:

Dr. Andrea Lamberti (Polito)



Contents

1	Abstract	4
2	Introduction	6
2.1	<i>The Problem - Energy resources crisis</i>	8
2.1.1	Availability	8
2.1.2	Polluting capability	12
2.2	<i>The Solution - Energy Harvesting</i>	14
2.2.1	Blue Energy Harvesting	14
2.3	<i>State-of-the-art Devices</i>	17
3	Physics	23
3.1	<i>Nanofluidics</i>	23
3.1.1	Continuum description limit	23
3.1.2	Main Nanofluidic length scales	24
3.2	<i>EDL-based transport and effects</i>	28
3.2.1	Ion-specific surface transport	28
3.2.2	Surface Conductance	31
3.2.3	Enhanced energy generation efficiency	34
3.3	<i>Device's Physics - Reverse Electrodialysis</i>	36
3.3.1	Donnan equilibrium	38
3.3.2	PNP equations	40
3.3.3	Power generation	42
3.3.4	Ion selectivity	45
4	Nanofabrication	46
4.1	<i>Graphite mechanical exfoliation</i>	47
4.2	<i>Flake's optical check and selection</i>	48
4.3	<i>2D Material manipulation and transfer</i>	51
4.3.1	PDMS manual dry transfer	51
4.3.2	PMMA Semi-automatic Dry Transfer	53
4.4	<i>PMMA cleaning and spin coating</i>	58
4.5	<i>Electron Beam Lithography</i>	60
4.6	<i>TEM lithography</i>	62
4.7	<i>Plasma Etching</i>	65
4.7.1	Etching analysis	66

5	Measurements and Results	<i>69</i>
5.1	<i>Experimental setup</i>	69
5.1.1	Characterization routine	70
5.2	<i>Electrophoretic transport in equimolar medium</i>	71
5.2.1	I/V Characteristics	72
5.2.2	Diode-based effects on power generation	76
5.2.3	Ionic conductance	78
5.2.4	Access Resistance and Surface Conductance	80
5.3	<i>Electro-Osmotic transport</i>	84
5.3.1	Osmotic power generation and conversion efficiency	90
5.3.2	Pressure-Driven ionic transport	94
6	Conclusion	<i>100</i>
	Bibliography	<i>102</i>

1 Abstract

Two-dimensional (2D) materials have allowed the fabrication of few-atom thick, atomically smooth nanopores and nanochannels.

The anomalous transport of ions and molecules within such extreme nanostructures strongly depends on the physical confinement, the geometry of the nanofluidic device and the physicochemical properties of the materials used. Understanding the importance of those parameters and controlling them at the atomic scale will enable the design of breakthrough technologies in filtration, biology, nanomedicine and energy harvesting.

This work focuses on the design, nanofabrication, and characterization of nanopores based on 2D materials (Graphene and Hexagonal Boron Nitride) for transducing the electrochemical potential difference between fresh water and seawater into an electrical current, with the ambition to be an alternative novel building block for the Blue Energy harvester of the future.

We engineered the shape, geometry and material properties of graphene and boron nitride multi-layer nanopores and studied the influence that each of these parameters have on the energy harvesting efficiency and ionic transport.

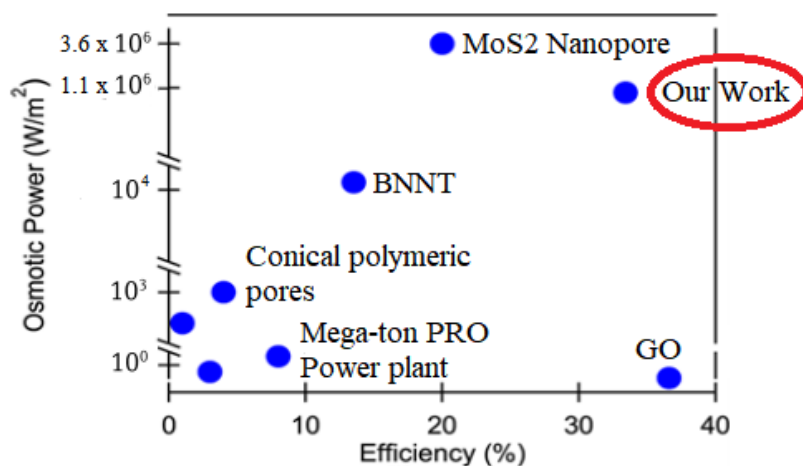


Figure 1: Comparison between power generation vs power generation efficiency for different nanofluidic systems. BNNT stands for "Boron Nitride nanotube", GO is the acronym for Graphene Oxide.

Our devices have proven to be resilient to environmental conditions, mechanically robust and able to harvest from few kW/m^2 up to a maximum of $1.1MW/m^2$ with high efficiency (up to 38%): 6 orders of magnitude higher than commercially available membranes and comparable to the leading monolayer MoS_2 nanopores both in terms of power generation and energy conversion efficiency.

Finally, we developed a scalable nanofabrication process to build both highly selective ionic conductors, nanofluidic diodes and, at the best of my knowledge, the first nanopore-based pressure sensor: Fundamental building blocks of the emerging field of iontronics where ions are used as signal carriers to bridge solid-state electronics with biological system with significant implications for bio-compatible logic circuits, for sensing and brain-machine interfacing.

2 Introduction

As of today, humans have used more resources than Planet Earth can regenerate in a year

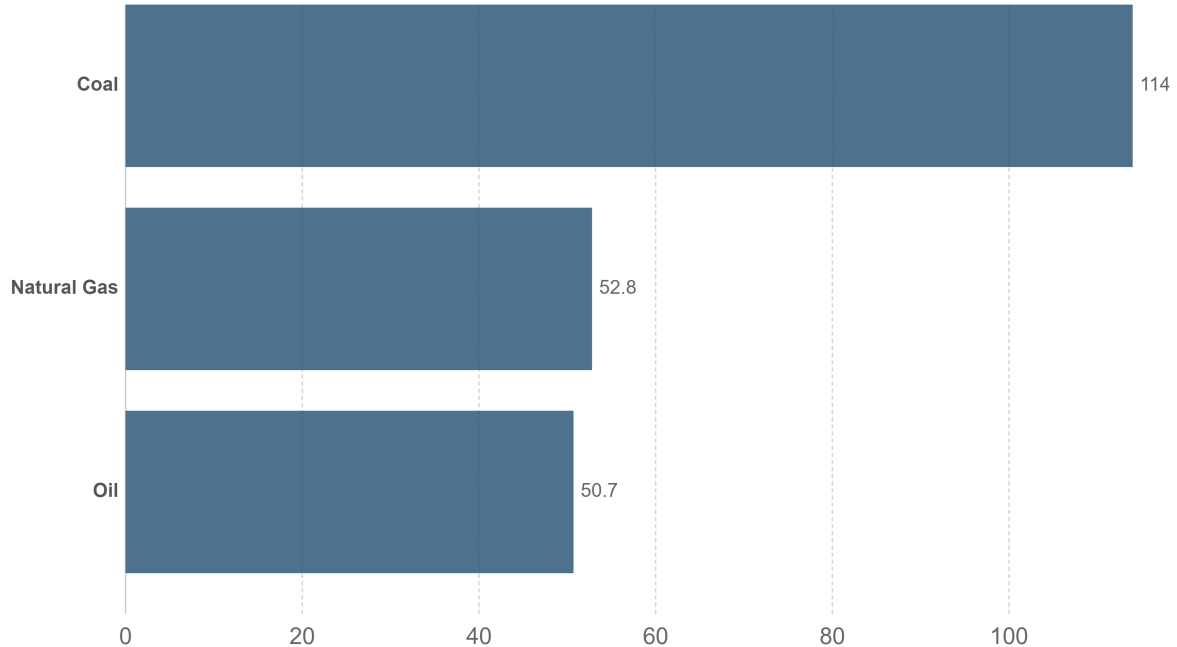


In a age in which the global energy demand keeps rising at an incredible speed, most of the time even mining the environmental safety and without considering the nowadays limited amount of natural resources, the development of cutting-edge systems capable to efficiently generate renewable and clean energy becomes the priority.^{1,2}

Years of fossil fuel reserves left



Years of global coal, oil and natural gas left, reported as the reserves-to-product (R/P) ratio which measures the number of years of production left based on known reserves and annual production levels in 2015. Note that these values can change with time based on the discovery of new reserves, and changes in annual production



Source: BP Statistical Review of World Energy 2016

OurWorldInData.org/how-long-before-we-run-out-of-fossil-fuels/ • CC BY

Figure 2: Reserve-to-product ratio that can be directly interpreted as the remaining years of source's availability based on 2015 energy consumption.

The main core idea upon which this thesis is based relies on the **Blue Energy Harvesting**, a promising renewable energy source that is able to generate exploitable electrical power directly from the water, having an almost null impact on the environment. The project in particular, represent my personal sheer will to investigate how the properties of the revolutionary 2D nanomaterials, such as Graphene, Boron Nitride, the solid-state membrane geometry and dimensionality, as well as the internal surface charge distribution, influence the system's power generation. The final result would be the possibility to obtain an economically viable device capable to substitute or to support at a deeper level of integration the traditional polymeric-based membranes. Furthermore all the data obtained as well as the design and fabrication solutions, lay the foundations to design the primal "building blocks" of the much complex and industrially-

exploitable Blue Energy harvester of the future. I personally went through the whole design process from the nanofabrication until their characterization, data analysis and modelling of the results.

2.1 The Problem - Energy resources crisis

Per definition the "energy crisis" is the global distress which takes up when the limited non-renewable natural resources, which are used to power mainly industrial societies, could end as the demand keep rising at a much higher pace.

It is a problematic very hard to objectively describe since, especially in recent years, became a broad topic intimately related also to other issues like the overpopulation and the climate change. Moreover it could be perceived from one country to another in a very different way, perspective and level of concern, usually due to an inherited thinking philosophy, which is directly linked to much more humanistic aspects than scientific ones.

For instance countries who strongly depend on the second and third sector, such as America or China, do not seem to be worried about the fast decline of fossil fuels, keeping their manufacturing rate at an unsustainable level. Instead other countries that strongly rely on the primary sector, or had developed a strong connection with the surrounding nature (usually the third world countries), are trying to expose such disruption.

Despite all, conscious or not, it is undeniable that the humankind is quickly moving towards the exhaustion of non-renewable energy resources and even though this knowledge contains a message that we fear, it is vital to avoid burying our heads in the sand and keep pushing the research onto new sustainable energy choices.³

2.1.1 Availability

Before starting to talk about the remaining availability of the energy sources it is necessary to depict the general trend regarding the primary energies consumption. The data collected and made of public access by **USA Energy Information Administration** are presented in **Tab.1**

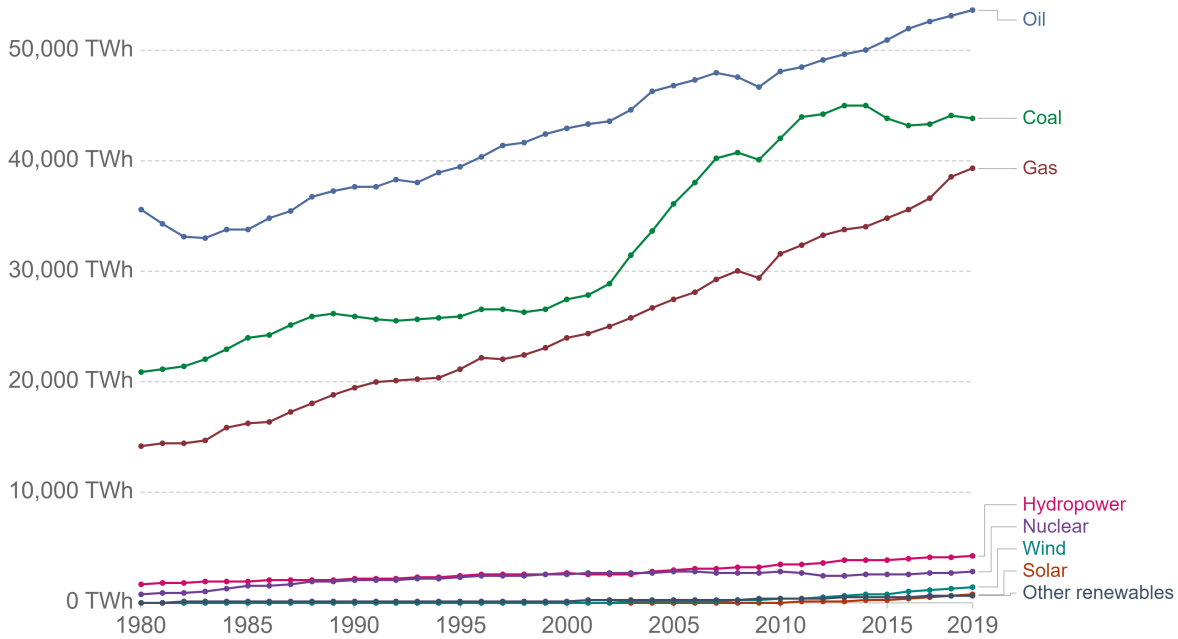
	1980	2008	2018	2019
Oil	35,577 TWh	47,566 TWh	53,181 TWh	53,620 TWh
Coal	20,858 TWh	40,770 TWh	44,109 TWh	43,849 TWh
Natural Gas	14,239 TWh	30,025 TWh	38,517 TWh	39,292 TWh
Nuclear	712 TWh	2,738 TWh	2,700 TWh	2,796 TWh
Non renewables	85.84%	88.20%	88.02%	87.87%
Modern Biofuels	0 TWh	574 TWh	1,109 TWh	1,143 TWh
Other renewables	49 TWh	316 TWh	615 TWh	652 TWh
Solar	0 TWh	13 TWh	583 TWh	724 TWh
Wind	0 TWh	221 TWh	1,270 TWh	1,430 TWh
Hydropower	1,732 TWh	3,257 TWh	4,171 TWh	4,222 TWh
Traditional Biomass	10,000 TWh	11,829 TWh	11,111 TWh	11,111 TWh
Renewable	14.16%	11.80%	11.98%	12.13%
Total	83,167 TWh	137,309 TWh	157,366 TWh	158,839 TWh

Table 1: Summary table of all renewables and non renewables energy sources consumption from 1980 to 2020

From this table it is possible to extract some interesting data. The consumption of energy worldwide keeps increasing. Specifically, it was measured a relative increment equal to 65.10% during the period from 1980 to 2008, or a total of 91% during the last 40 years, with an absolute global increase of 75,672 *TWh*. What should warn is that most of the increase comes from non-renewable energies. As a matter of fact, even if the specific relative increment in the renewable sector could appear higher compared to the one related of the non-renewables, in reality during almost 40 years of technological development the absolute usage of renewable sources as a part of the worldwide energy consumption has seen a decrease of -2.03% keeping the majority of energy consumption to non-renewable energies. (87.87%). In **Fig.3** is possible to visually appreciate the huge gap that still exists in terms of energy sources exploitation.

Primary direct energy consumption by source, World

Energy consumption is shown as direct primary energy. This means this does not correct for fossil fuel inefficiencies in conversion to useful energy estimates.



Source: BP Statistical Review of Global Energy

Note: Includes only commercially-traded fuels (coal, oil, gas), nuclear and modern renewables. As such, it does not include traditional biomass sources.

OurWorldInData.org/energy • CC BY

Figure 3: Worldwide Primary Energies consumption by source from 1980 to 2019

The total energy consumption trend maintained its fairly linear behaviour with a growth rate of 1.5% per year from 2008 to 2017 and the strongest increase of all time within the 2018-2020 equal to 2.9%, almost doubling the previous 10 years average. To further impress and underline the data cited above, in **Fig.4** it was sketched in form of pie chart the relative exploitation rate of the main world's energy sources.

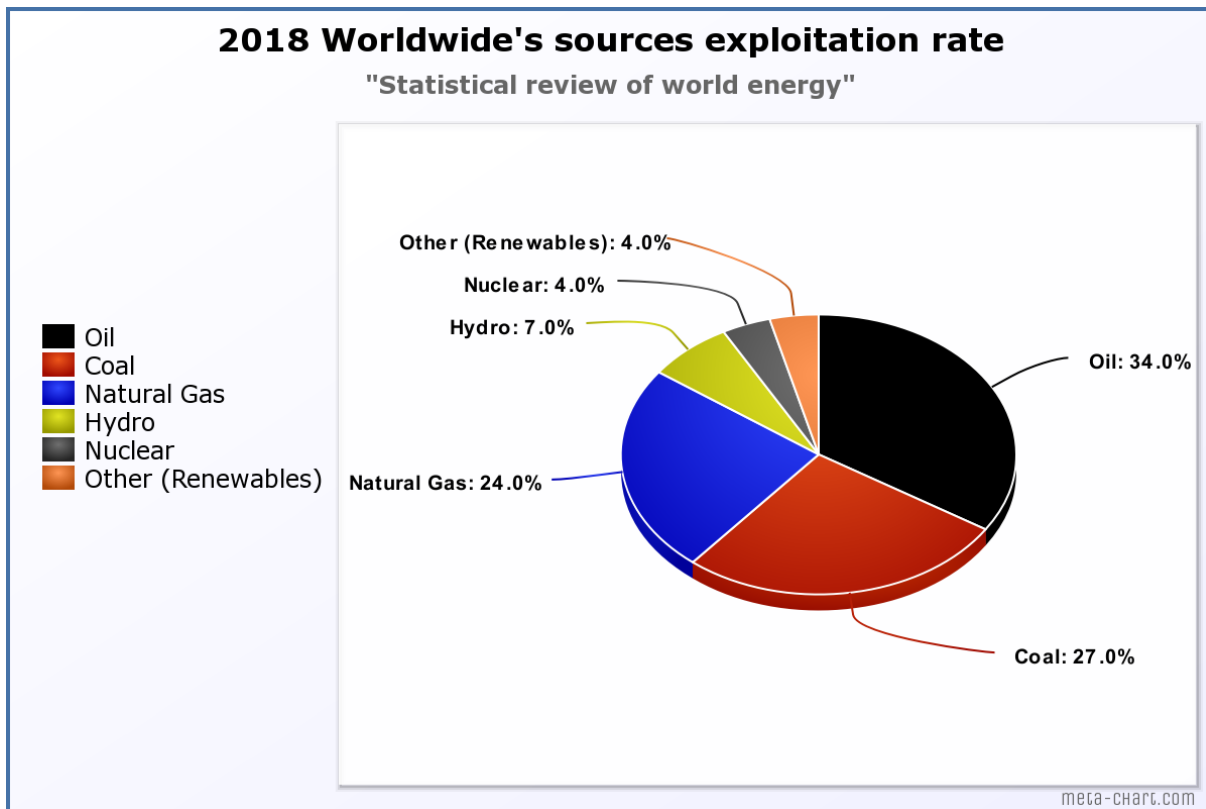


Figure 4: Relative exploitation rate of all world's resources in 2018

As it is possible to evince from **Fig.4** Fossil fuels, Coal and Natural Gas are non-renewable sources of energy which, from the last century up to these days, cover most part of the energy supply for the already rich developed and fast developing societies. Therefore it is very important to evaluate how much the reserves of each of these resources may last if we consider the actual consumption rate.

To give a static estimation of how long it could be feasibly possible to consume fossil fuels to produce energy one need to calculate the Reserves-to-Production (R/P) ratio. It was presented at the beginning in **Fig.2**. Calculator in his hands one may argue that still more than half of the total reserves are left and that this would not be a pressing problem for the next 50 years. Nevertheless considering the current consumption and growing rhythms, plus the new production peak that the world is reaching (**Fig.5**), humanity will likely completely run out of fossil fuels in less than 30 years.

Hubbert's peak prediction vs. actual oil production in the United States

Hubbert's hypothesis of peak oil production in the United States, alongside actual oil production trends in the United States, both measured in barrels per year.

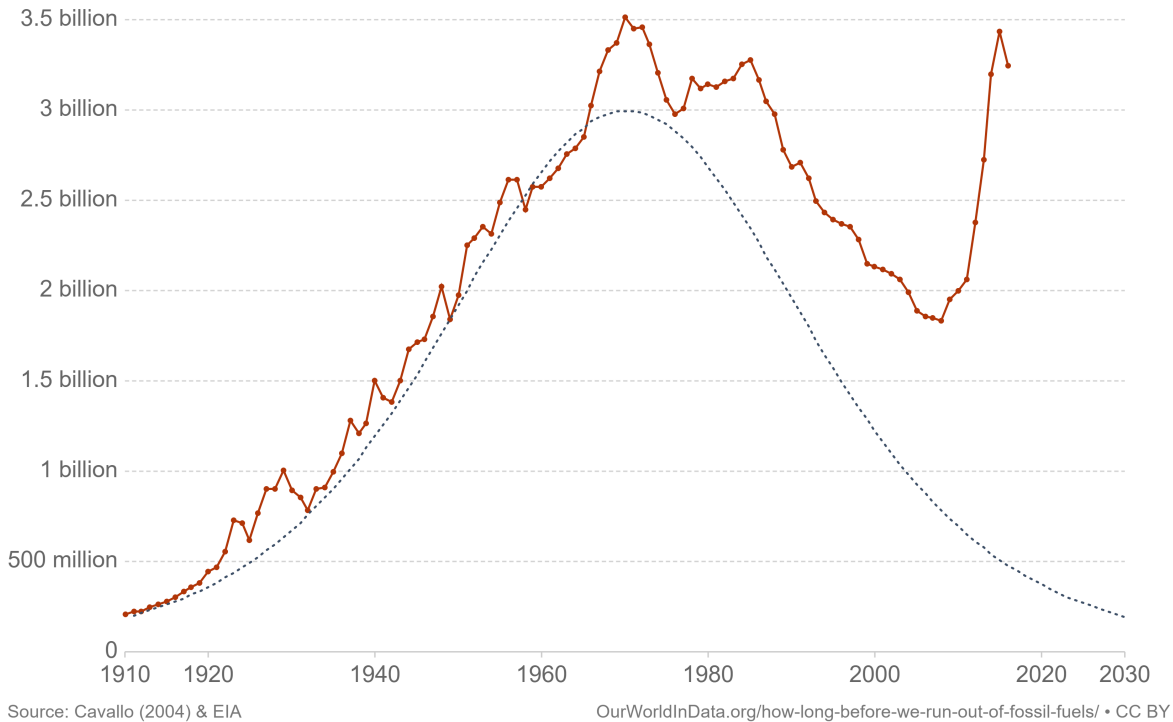


Figure 5: *American fossil fuels peak prediction*

The actual crisis and all the data obtained during this Covid-19 pandemic announces the beginning of the end.

2.1.2 Polluting capability

Although exhausting energy's reserves could turn out to be a critical problematic only 50 years from nowadays, it is still present another significant issue linked to fossil fuel production: The Climate change.

Effectively, it has been recognized from many years that carbon-based energies and the climate change belong inevitably to the same equation. Just citing the **Global energy & CO₂ status report**, mostly driven by a higher energy demand in 2018, the global energy-related CO₂ emissions rate grew of 1.7% points, thus bringing to a historic high of 33.1 Gt of CO₂. It was calculated that, while emission from all fossil fuels increased, the total power sector accounted for almost two-thirds of CO₂ emissions growth.

That is why if one wants to solve or at least slow down the climate change issue, governments have to learn to completely resign to fossil fuels usage and try to develop new technologies able to extract clean and sustainable energy. As collected in the chart of **Fig.6**

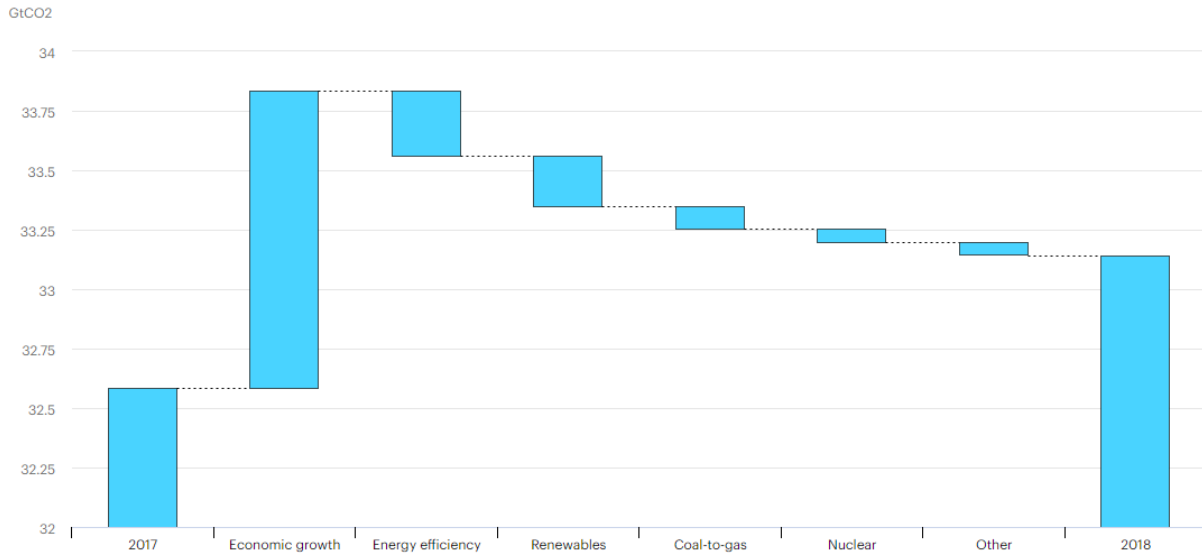


Figure 6: Visual representation of CO₂ emission reduction due to the technological development, switch in energy source and renewable energy usage. "IEA, Change in global energy-related CO₂ emissions and avoided emissions, 2017-2018, IEA, Paris"

energy efficiency technologies were the real first important break on emissions growth after the economical growth of 2018, nevertheless its contribution was around 40% lower than in 2017, mainly due to a political slowdown in implementing energy efficiency policies. After that an increased use of renewables in 2018 had a greater impact on CO₂ emissions, lowering the total value of an amount equal to 215 Mt, the vast majority of which is due to a specific transition to renewables in the power sector. It was estimated that without this evolution to low-carbon sources and new renewable energy extraction approaches, emissions growth would have been 50% higher than the one the world experiences in 2017. This focused lookout underline even more that if any action would be taken the entire humanity will pay the first-world countries "voracity" with unknown and unpredictable consequences with absolute no way back at a human time scale. Such ecologic footprint is no longer sustainable. We all should work on reducing the overall energy consumption and by changing the energy

supply with renewable, non-combustion and locally available alternative energy sources. An alternative source that is growing more and more now is commonly known as **Renewable Energy Harvesting**.

2.2 The Solution - Energy Harvesting

An Energy harvesting technology is a device that yields a specific type of ambient energy and converts it into electrical energy. Such technology has been recently considered as one of the most attractive renewable power source. It is so mainly because it wide opens different new ways of extracting clean energy from many sources, which nowadays are still not considered or used. In addition what is really appealing about those solutions is that, coupling this new way of harvesting energy directly with the discoveries and brand new effects rising at the nanometric scale, permits to develop very interesting and clever solutions in a wide range of different fields, such as: Remote sensing, Biomedical implants, Smartphones, IoT.^{4,5} As introduced above there are various ambient energy sources for portable energy harvesting systems, just citing some that are included: mechanical work, pressure gradient, temperature gradient and ionic concentration gradient. The device that has been developed by me during these six months for my Master Thesis basically relies on multiple effects: The Gibbs free energy arising during the mixing of two solutions with different salt concentrations, but also by the consequent osmotic pressure that contemporary builds up. This type of process is now known as **Blue Energy Harvesting**.

2.2.1 Blue Energy Harvesting

This promising process belongs to the chemical harvesting cluster, particularly known as Blue Energy (because involves the use of water), and exploits an energy recovery procedure called Reverse Electrodialysis (RED).

Energy Harvesting (EH)

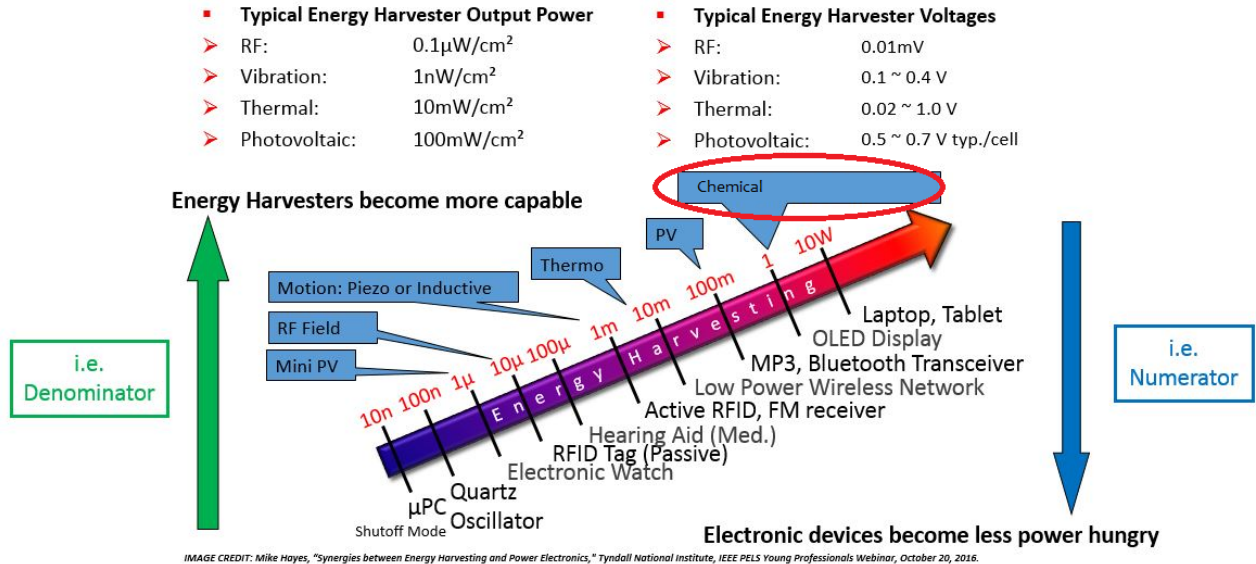


Figure 7: Energy harvesting sources and typical Output Power/Voltages

In particular it allows to recover electrical power from the concentration gradient between a highly concentrated solution (i.e. brine, seawater, etc) and a much more diluted solution (i.e. fresh water of a river). The transport of anions and cations through the membrane may be determined by two different mechanism: The application of an external electric field, by the means of two electrodes, that determines a "drift" motion and a natural **diffusion-driven** transport due to the above cited salt concentration gradient. As depicted in **Fig.8** the RED energy recovery process is entirely based on the latter process.

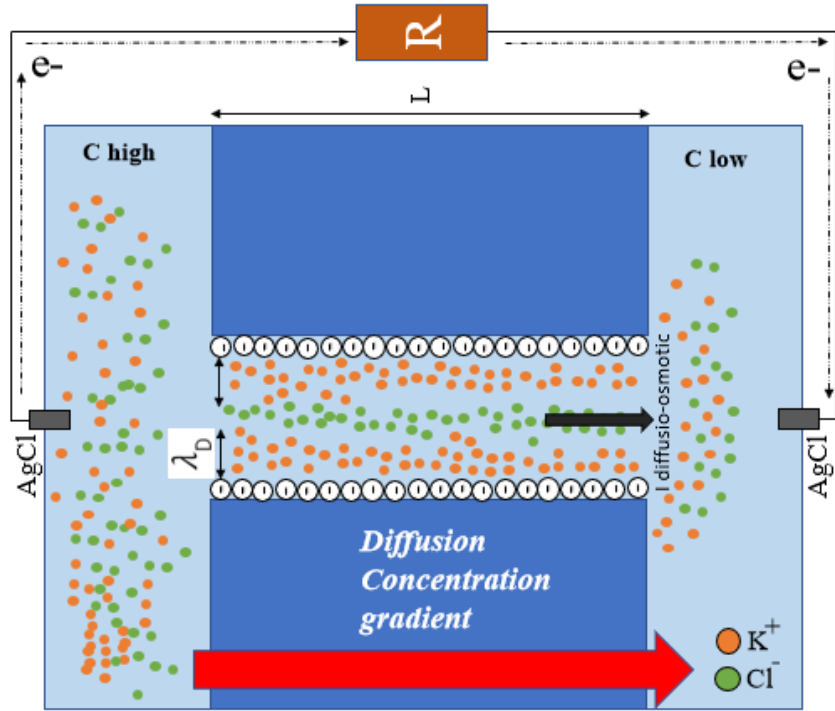


Figure 8: Example of a solid state nanochannel membrane developing a selective ion transport for Blue Energy generation. The cell is composed by a high-concentration (HC) and low-concentration (LC) reservoir, both separated by a Graphitic nanochannel that acts as a permselective ionic membrane

At zero applied voltage, the ions passage is mainly controlled by the concentration difference and the membrane itself. Specifically thanks to the formation of a positive or negative surface charge distribution called **Electrical Double Layer** (EDL) that electrostatically screens out the ion with the same charge. Since only a specific type of ions will pass through the membrane, a net ion current is formed and the system electroneutrality broken. In order to recover the equilibrium condition a net electronic current is consequently established and maintained by red-ox reactions at the electrodes, finally balancing the overall charge. The resulting electrical current and the membrane potential can be used to actively generate electrical power through an external load. The system is indeed harvesting clean blue energy.⁶

The Blue Energy Harvesting is characterized by many advantages, including the sustainability of energy sources (since the natural mixing of seawater and pure water is very common in our planet in different spots, like an

estuary), great mechanical reliability due to no moving parts, and above all a high energy efficiency thank to the direct conversion from chemical energy to electrical energy.

The amount of free energy that may be extracted from the mixing is very promising. Theoretically it was estimated that the energy harvesting yield will be equal to $3kJ$ per mixed litre of salty and pure water or equivalently to $0.8kWh/m^3$, which could be harvested by prospective power generators.^{7,8} Furthermore the general estimate for the global potential of this new energy source (**World Energy Resources 2016**) reaches up to 8500 *TWh*. This plus all the available renewable energy technologies could cover over the 80% of the current global electricity demand^{6,9,10,11} contemporary reducing the gas emissions due to conventional electrical energy production of almost 40%.¹² Nowadays, according to the **International Energy Agency** the hydraulic energy production reaches an amount of 4,000 *TWh*, the nuclear energy lies around 2,600 *TWh*, while the wind and solar energies sources collect 1,100 *TWh* if added up together.

It is now straightforward to think that in the global energy balance, **Blue Energy**, can be thought as a renewable and non-intermittent source of energy with a great developing potential.

2.3 State-of-the-art Devices

After being hyped by all the promising theoretical numbers that may be extracted from literature, it is time to face the reality. In practice RED technologies are not problems-free. The main bottleneck lies in fact in the intrinsic trade-off between the energy harvesting efficiency and achievable osmotic power output.¹³ Furthermore it must be said that the actual technologies (such as many bulky membranes), exploited even at the large-scale level, presents some drawbacks, which are determining several challenges for a economically-viable application. Some examples are the high cost, the short lifetime of the membranes and the bio-fouling.^{14,15}

In the last years people moved from novel ceramics^{16,17}, polymers^{18,19} and thick porous nanomaterials²⁰ (characteristics summarized in **Fig.10**) to the precisely microfabricated thin nanofluidic membranes such as Nanopores, Nanochannels or Nanotubes made of different and interesting materials such as Graphene, Molibdenum Disulfide (MoS_2) or Boron Nitride (BN).

All outstanding examples of the current state-of-the-art in the field (characteristics summarized in **Fig.11**).

Functionalized nanofluidic channels or nanopores are a possible and practical solution to avoid all those drawbacks. For example to easily reduce the membrane cost, nanofluidic channels or nanopores can be easily modified during the nanofabrication, by means of different gas plasmas, to achieve a high and ultra specific ion selectivity and also an enhanced flow rate (thus a low membrane resistivity) exploiting new physical behaviours due to the nanoscale, as it will be explained in chapter 3.

Just to give some more details about the evolution of the state-of-the-art nanofluidic devices, the first considerable increase in generated power density reported in the literature was obtained in 2013 by using well-defined geometry boron nitride nanotubes (BNNTs) presented in **Fig.9**. In that case *A. Siria et al.*²¹ reached up power densities up to $4kW/m^2$ in a RED configuration.

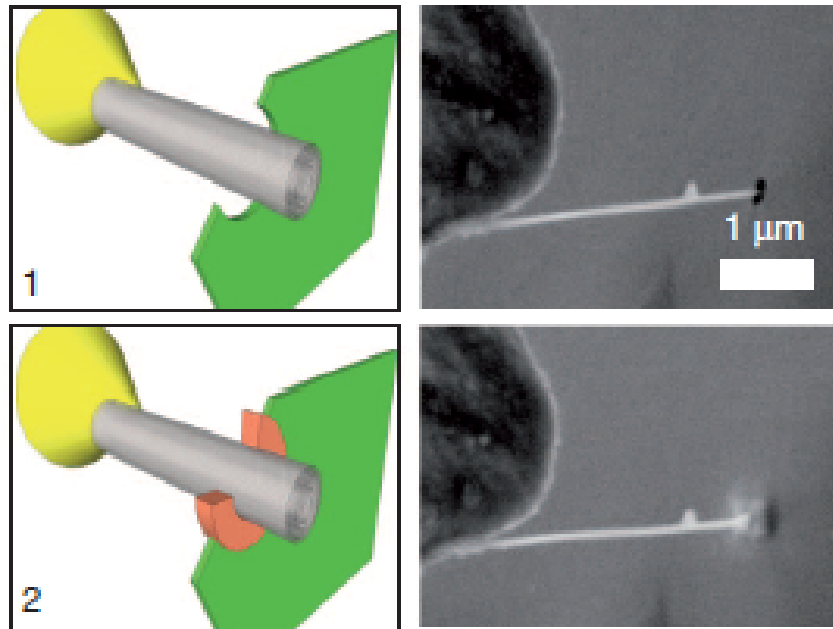


Figure 9: Hierarchical single nanotube nanofluidic set-up. In situ nanomanipulation of a BNNT: 1) insertion of a BNNT through a nanopore drilled in a SiN membrane (green) using a focused ion beam, 2) carbon sealing of the FIB-drilled hole using local electron-beam-induced deposition (orange)²¹

After the BN nanotube, in 2016, the 2D material MoS_2 was used to

fabricate atomically thin membranes, the work of *Feng, J et al.*²² reached a simulated power density of $3\text{MW}/\text{m}^2$ with conversion efficiency of 20%. Then, to complete the brief presentation of the state-of-the-art devices based on 2D materials, in 2019 it was reported from *Yanjun Fua et al.* an efficient Graphene-based RED system able to reach up competitive power densities in the order of the kW/m^2 , but this time with a record-high energy conversion efficiency η of 40%.²³ These results demonstrate improvements of orders of magnitude as compared with ‘thick’ solid-state membranes, making the 2D nanomaterials particularly promising for osmotic energy harvesting applications.²⁴

Material	Pore diameter	Pore Length	Porosity	pH	Type of experiment	Power density at specific salt concentration	Power per pore	Osmotic conductivity per pore	Electro-kinetic energy conversion efficiency
Commercial applications									
Statkraft PRO power plant	–	–	–	–	–	1W m^{-2}	–	–	–
Mega-ton PRO power plant	–	–	–	–	–	13W m^{-2}	–	–	–
Global MVP project	–	–	–	–	–	5W m^{-2}	–	–	–
REAPower RED power plant	–	–	–	–	–	0.83W m^{-2}	–	–	–
Solid-state pores									
Silica	$4\text{nm} \times 25\mu\text{m}$	$140\mu\text{m}$ (Channels)	Nano-channels ^a	5.6	Experimental studies	2.7W m^{-2} 0.0001/1 M	0.16pW 0.1/1 mM	73.4 pS	31%
	2–3 nm	90 nm	4×10^{12} pores cm^{-2}	~7	Experimental studies	0.024W m^{-2} 0.01/0.5 M	$6 \times 10^{-7}\text{pW}$	1.53 fS	–
Porous alumina	10–100 nm	$4\mu\text{m}$	10^8 – 10^9 pores cm^{-2}	5.4	Numerical studies	9.9W m^{-2} 0.001/0.1 M	0.14pW 0.1/1 mM	256.8 pS	–
	10 nm	$60\mu\text{m}$	1.18×10^{11} pores cm^{-2}	5.4	Experimental studies	542nW^b 10/100mM	–	–	–
	100 nm	$60\mu\text{m}$	1.2×10^9 pores cm^{-2}	5.4	Experimental studies	0.98mW m^{-2} 0.1/10mM 0.59mW m^{-2} 0.1/1mM	4.9 – $8.2 \times 10^{-5}\text{pW}$	150–360 fS	16%
	200 nm	$60\mu\text{m}$	1.2×10^9 pores cm^{-2}	–	Experimental studies	17.3mW m^{-2} 0.017/0.51M	$1.5 \times 10^{-3}\text{pW}$	4.9 pS	–

Figure 10: Properties and performance of different bulky platforms for osmotic power generation

Material	Pore diameter	Pore Length	Porosity	pH	Type of experiment	Power density at specific salt concentration	Power per pore	Osmotic conductivity per pore	Electrokinetic energy conversion efficiency
Solid-state pores (cont.)									
Nafion perfluorinated membrane	>10 nm	24 × 500 μm	10 ¹¹ pores cm ^{-2d}	5.6	Experimental studies	0.7 W m ⁻² 0.001/2 M	7.0 × 10 ⁻⁴ pW	471.4 fS	36%
hBN nanotube	15–40 nm	1 μm	Single pore	11	Experimental studies	4 × 10 ⁴ W m ^{-2e} 0.001/1 M	20 pW	16.3 nS	–
2D nanopores									
GO flake RED cells	0.9 nm	0.5–100 μm (stacks)	–	5.6	Experimental studies	0.77 W m ⁻²	–	–	36.60%
Graphene	0.4–10.0 nm	0.34 nm	Intrinsic defects	7	Experimental studies	700 W m ^{-2f} 0.001/1 M	10 pW 0.01/1 M	18.4 nS	–
MoS ₂	2–20 nm	0.65 nm	Single pore	11	Experimental studies	3 × 10 ⁶ W m ^{-2g} 0.001/1 M	1 nW	815.4 nS	20%
	3 nm	0.65 nm	Single pore	7.4	Experimental studies	0.01/0.1 M	1.2–2.8 pW	22.5–51.4 nS	8–44%
	10 nm						130–160 pW	238.5–293.6 nS	40–45%
	1 nm	0.65 nm	Single pore	5	Numerical studies	7.1 × 10 ⁵ W m ^{-2h} 0.001/1 M	–	–	–

Figure 11: Properties and performance of different 2D platforms for osmotic power generation

In general, just considering the differences between a nanopore and a nanochannel (in **Fig.14**) from a pure nanofabrication and physical standpoint, it is possible to point out that in most of the cases a nanopore is characterized by the characteristics summarized in **Fig.12**^{25,26,27}

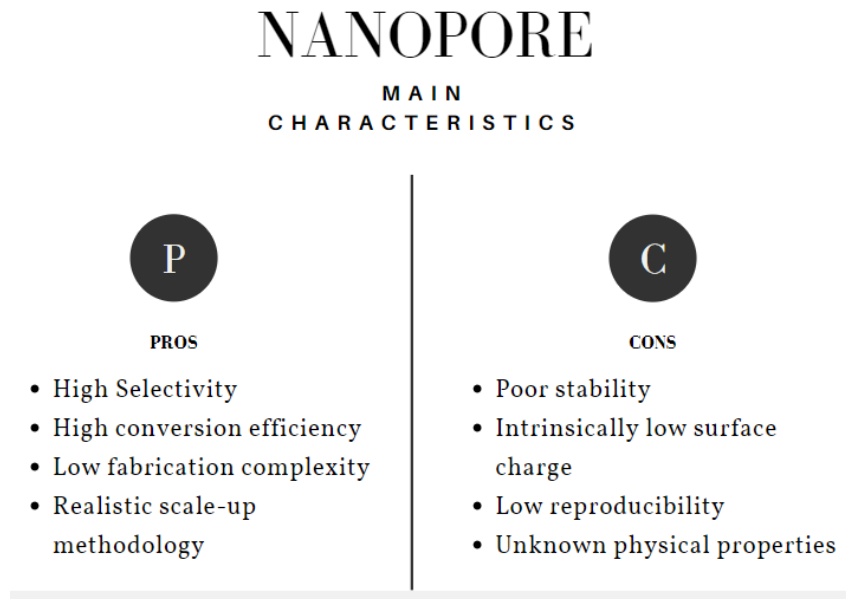


Figure 12: Advantages and drawbacks of common nanopore-based RED energy harvester

As a complementary counterpart there are instead nanochannels and nanotubes, which characteristics are summarized in **Fig.13**.^{28,29,21,30}

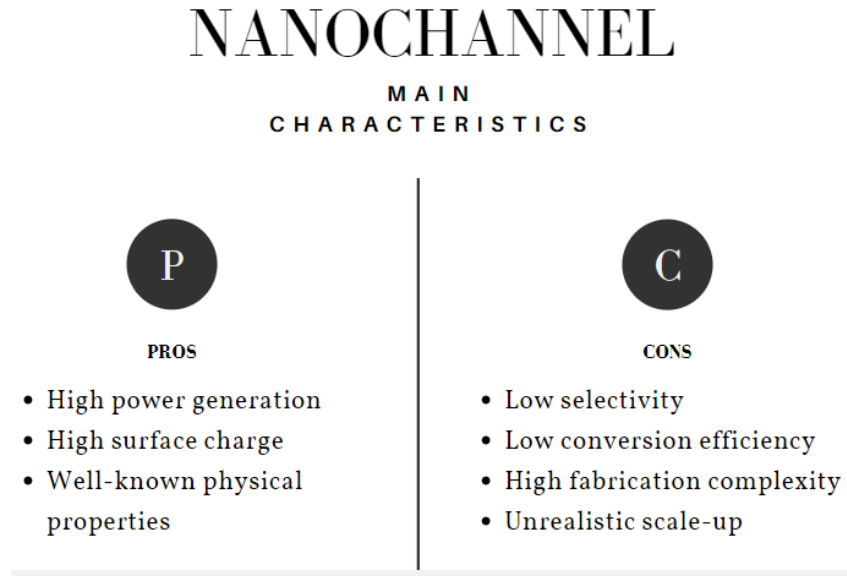


Figure 13: Advantages and drawbacks of common nanochannel-based RED energy harvester

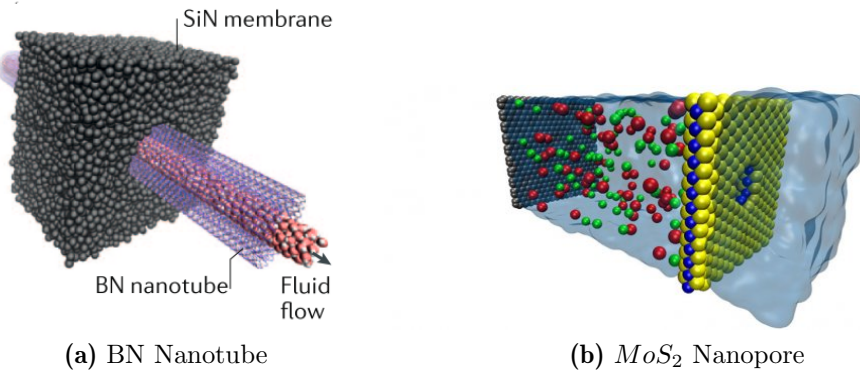


Figure 14: 3D image of a nanotube and a nanopore from: "2D materials as an emerging platform for nanopore- based power generation"

Presented those characteristics one could expect that a new device geometrically defined as something in between these two systems, a thick nanopore or an ultra-short nanochannel, would present different advantages and/or drawbacks from the classes just described above, or at least that could be interesting study and characterize it to have a complete and

clear vision of the resulting nanofluidics in different regimes. That is why after a deep and focused analysis of the different aspects linked to both the devices, which will be also presented in the future chapters, it was decided to move this master thesis experience towards something new, a device that has not been investigated yet, but is still able to offer, to the best of my knowledge, a set of interesting characteristics and physical behaviours.

3 Physics

From the introduction chapter above, even just presenting a general description of the matter, it appears clear that both the system's geometry and structure, as well as the inner surface properties, play an irreplaceable role in the Blue Energy harvesting process.

Moreover the importance of these aspects will be further underlined presenting the physical framework on which my study is based, the **Nanofluidics**.

3.1 Nanofluidics

The word "Nanofluidics" defines a specific research field, where all the attention is directed toward the study of the fluidic transport and dynamics when approaching the nanometric scale down to the molecular confinement. Forcing the limits of fluidic downsizing, as the expected scale reduction that is performed in many other micro and nanotechnologies, is an appealing goal that will benefit many different applications.^{31,32}

From a merely fluidic stand point, the nanometric scaling allows to discover or exploit new functionalities, which directly come from the beneficial predominance of the surface-to-volume ratio.³³

Some of the common examples are the development of nanofluidic transistors or the newer fluidic diodes^{34,35}, or the emerging of specific phenomena observable only at the smallest scales, where the physical behaviour totally diverge from the normal physical expectations. A nice example to present are the biological thick nanopores present in the cellular membrane, known as aquaporins, which present extreme permeability to water while contemporary ensuring almost total selectivity for other ion species.

3.1.1 Continuum description limit

When talking about Nanofluidics one may retrieve mainly two different origins for the finite-size effect generated by the nanometric confinement. The first one is a purely *Bulk* effect, while the second one is much more related to the *Surface* influence. The former is intimately linked to the question of validity of the classical continuum framework, which is totally

described by the Navier-Stokes equations and in particular starts to be effective when the canonical classical model breaks down and the molecular nature of fluid begins to be relevant. The latter instead starts to play a role when the confinement is still at the nanoscale, but can be normally described by the classical hydrodynamics equations. The important question at this point becomes: When does the Navier-Stokes description start to break down? A lot of experiments or Molecular dynamics simulations suggest that a typical fluidic parameter, such as the fluid viscosity, maintains its classical description up to a length scale of ~ 3 nm.^{36,37} Theoretically speaking, Navier-Stokes equations rely on the assumption of a separation within the observed length scale and the molecular dynamics, thus permitting the averaging out of all the fast variables. Doing so the equations describing the microscopic behaviour, which are associated to an enormous number of degrees of freedom, depend now only on very few parameters. To mathematically perform this simplification it is needed to write the transport coefficient with a Green-Kubo relation. As an example:

$$\eta = \frac{1}{Vk_B T} \int \langle \sigma_{xy}(t) \sigma_{xy}(0) \rangle_{equ} dt \quad (1)$$

where σ_{xy} is the non-diagonal component of the stress tensor³⁸ and $\langle \cdot \rangle_{equ}$ is an equilibrium average. The time-scale separation for the validity of equation **Eq.1** needs that the microscopic time scale of the stress-stress correlation function (τ_σ) has to be much smaller than the hydrodynamic time scale $\tau_q = (vq^2)^{-1}$ with $v = \frac{\eta}{\rho}$ where η is the cinematic viscosity and ρ the mass density. The time-scale separation, and thus the continuum description validity, holds for confinement higher than a continuum limit variable l_c . $w > l_c = \sqrt{v\tau_\sigma}$ that in water is roughly equal to 1 nm.³³

3.1.2 Main Nanofluidic length scales

Besides the continuum limit l_c it is possible to find a wide range of different length scale related to various nanofluidic behaviours. Nevertheless since up to now reaching a type of confinement that goes below the continuum limit is very challenging for the actual nanofabrication's techniques, only a limited amount of those fundamental length scale will be described in the following paragraph. The first group collect all the **Electrostatic lengths**

that still have an influence in the fluid transport dynamic. They specifically describes long range interaction between the flowing ions through a nanopore and the inner charged surface, as well as the direct ion-ion interaction. Must be underlined that, due to the long range nature of these type of interactions, all the effects appearing at a smaller scale actually climb up to larger scales, having a direct impact even in larger systems.

- **Bjerrum length**

The Bjerrum length (l_B) is defined as the distance at which the electrostatic interaction between two charged species becomes equal, or of the same order, to the the thermal energy $E_{th} = k_B T$. The mathematical expression for two ions, with a valence Z , immersed in a dielectric medium (ϵ) is described by **Eq.2**:

$$l_B = \frac{Z^2 e^2}{4\pi \epsilon k_B T} \quad (2)$$

In water this values in equal to $l_B = 0.7nm$. this means that having an aqueous solution filled of monovalent ions, and this is forced to pass through a channel with a dimension smaller than the Bjerrum length, the energy cost to undress the ions of their hydration shell and make it pass will be larger than the thermal energy furnished by the surrounding environment. This means that we have a system that is passively filtering ions, as it happens in biological ion channels.

- **Debye length**

From the introduction it appears clear that the **Electrical Double Layer** (EDL) is one of the most important concept in many nanofluidic applications. The EDL, sketched in **Fig.15**, is defined as the proximal region to a charged surface where a "cloud" of counterions balance the net surface charge of a solid system. It is thus obvious that in this region the electroneutrality condition is completely broken.^{39,33}

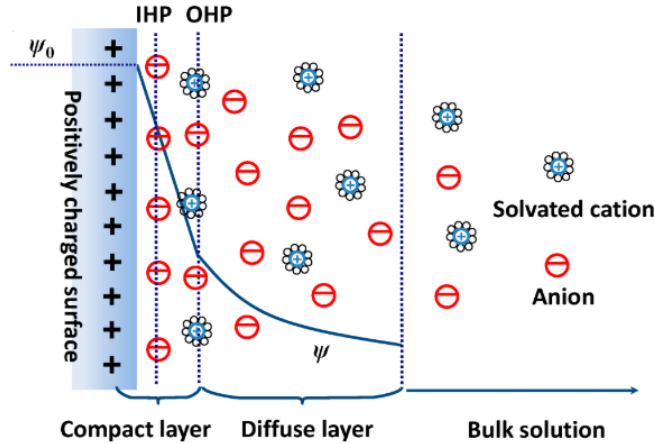


Figure 15: Schematics of the EDL (Compact + Diffuse layer) in a solid-liquid interface. IHP and OHP stand for Inner and Outer Helmholtz plane. Φ_0 is instead the surface potential given by the net surface charge

Using the *Poisson-Boltzman* theory, which is particularly suited for the analysis of electrolytes free ion's motion in the vicinity of a charged surface, it is possible to extract the mathematical formula of the Debye length.^{40,41} Combining the Poisson equation for the electrostatic potential and the Boltzmann equation for the distribution of diffusing ions, after some mathematical steps, it emerges that the electrostatic screening in the electrolyte, defined in terms of the salt concentration ρ_s is:

$$\lambda_D = \frac{1}{\sqrt{(8\pi l_B \rho_s)}} \quad (3)$$

The Debye length, describes the extension of the **Electric Double Layer** (EDL) inside the channel. Appears to be independent of the surface charge and fixed by salt concentration in the reservoir. To give some values, normally it lays in a range comprised 1 nm up to 60 nm respectively for a 1 M and 0.1 mM solution.

This length play a fundamental role in nanofluidic. For instance when applying an external electric field, the Debye region is the only one that actually experience the volume electric forces $f_e = \rho_e E_e$, with ρ_e being the charge density and E_e of course the applied electric field. That is why tuning the fluid properties within this region will affect the system's response under the same applied electric field, but also will have a macroscopic repercussion at much larger scales. Furthermore this simple description

underline the importance of this parameter, followed by the right geometrical dimension of the channel, for what concern the Permselectivity of the system. Just as reminder, in the introduction it was said that to enhance the power generation and the energy conversion efficiency one of the main parameter to properly tune is, in fact, the system's permelectivity. When the dimension of a nanopore is comparable to the Debye length ($r < \lambda_D$), the EDL overlap, determining a selective and surface regulated ion passage, which will efficiently drive the whole RED process.

- **Dukhin length**

The Dukhin length is a very interesting parameter that permits to analyze at which scale the surface conduction overcome and dominates the pure bulk conduction. It can be expressed in many different ways. One for instance could be just the ration between the surface conductivity κ_S and the bulk conductivity κ_B . Or in a more interesting way, showing the direct dependency on the Surface charge Σ as $l_{Du} = \frac{\Sigma}{\rho_S}$. This length particularly plays its role when describing the conductance (G) in nanochannels or nanopores, where surface effects strongly affect that parameter.⁴²

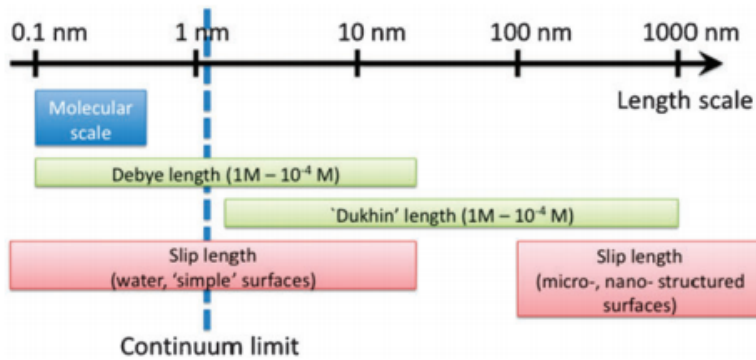


Figure 16: Graphical collection of all the main length scales in the Nanofluidics field

Wrapping up what it was presented in this chapter, it is possible to say that, even if most of the time the nanofluidic systems that we are dealing with can be described in a safe way by the classical Navier-Stokes theory, excluding numerous effects that diverge from the normal expectation and all the scientific breakthroughs related with them, just by analyzing the existence and the roots of these length scales there is no doubt that is

still possible to exploit and benefit of the surface effects entering in the game at technically-achievable scales. That is why being able to proper control, engineer or even just characterize and study the surface charge of such nanosystems and how it affects, in our case, the power generation or energy harvesting efficiency is still crucial and significant.

3.2 EDL-based transport and effects

The study of the electric diffuse layer from a bulk perspective has been already carried out by many research groups, both theoretically and experimentally. Nevertheless, as how it should be clear now, when dealing with such reduced dimensionality it is mandatory to rethink what is known and to describe it from a molecular point of view. Doing so it is likely to obtain and discover new unique concepts and phenomena. In the Debye length sections it was said that to extract this parameter, but also many others, one can safely use the Poisson-Boltzmann theory. Although this remains valid for many nanofluidic aspects, there is still a whole class of effects, intimately related to the specific ion nature, that cannot be caught or depicted in this continuum-conventional way. Such ion-specificity effects have profound effects on the ion-transport process within the EDL region.

3.2.1 Ion-specific surface transport

The EDL is the original root of distincts electrokinetic phenomena linked to the ion dynamics inside the nanometric EDL. More precisely it is time to write about two important symmetric phenomena, the **electro-osmosis** and the **streaming current**.

With the term **electro-osmosis** we refer to the electrically-driven flow of a liquid when subjected to an applied electric field E_{app} .

To retrieve the relation between the fluid velocity and E_{app} we should start from the stationary Stokes equation, presented in **Eq.4**, valid in conditions of such confinement (small Reynolds number):

$$\eta \nabla_z^2 v_x + \rho_e E_{app} = 0 \quad (4)$$

Where, the charge density $\rho_e = e(\rho_+ - \rho_-)$ completely vanishes within the EDL, E_{app} is applied along an axis parallel to the surface plane, direction x , and the fluid's velocity in the same direction just depend on the direction z perpendicular to E_{app} .

Considering that charge density in non-null only the EDL the whole driving force that actually moves the fluid develops in that nanometric region and can be expressed as **Eq.5**:

$$F_{app} = \rho_e E_{app} \quad (5)$$

Now if one wants to obtain the velocity expression from the Stokes equation, has to integrate it twice over the z direction. this also mean that a pair set of initial conditions to apply is needed. Before going further in the demonstration it might be useful to introduce another important length scale, coming out from the fact that under a nanometric confinement the classical assumptions need to be properly modified. This is the case of the no-slip ($v_f|| = 0$) boundary condition at the interface between a flowing fluid and the solid surface at its proximity. In case of strong confinement, as it was theorized and proved experimentally in hydrophobic interfaces, the tangential velocity at the interface appears to be non-null and equal to a *slippage* velocity (v_{slip}), while it becomes null at a length value, called slip length l_{slip} ^{43,44}, inside the solid surface as in **Fig.17**

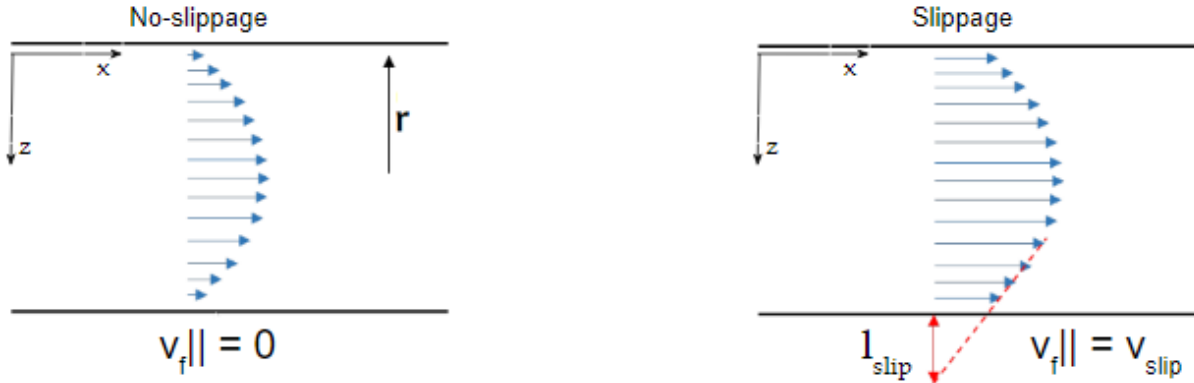


Figure 17: Sketch of the velocity field in a nanopore with an aperture radius r , in a No-slippage condition (left) and with a finite slip length l_{slip} (right). The x direction is the one parallel to the surface, while the z direction is the one normal to the surface along the radius

Considering what it has been briefly introduced above, the two initial conditions are expressed in **Eq.6** and **Eq.7**:

$$\partial_z v_{fluid}|_{z=0} = v_{slip} \quad (6)$$

$$\partial_z v_{fluid}|_{z=\infty} = 0 \quad (7)$$

At this point combining the Poisson equation (**Eq.8**)

$$\nabla^2 \phi = -\frac{\rho_e}{\epsilon} \quad (8)$$

and the Plank equation (**Eq.4**), also considering the two new initial conditions, one obtain the velocity profile along z-direction as **Eq.9**

$$v(z) = -\frac{-\epsilon\zeta}{E_{app}} [-\phi(z) + \zeta] \quad (9)$$

and that can further simplified by the Smoluchowski formula underlining the linear relation between the fluid velocity and E_{app} as presented in **Eq.10**:⁴⁵

$$v_{\infty} = \frac{-\epsilon\zeta}{\eta} E_{app} \quad (10)$$

with ϵ , η , ζ being respectively, the dielectric constant and the viscosity of the fluid and the electrostatic potential also called Zeta-potential, which for weak potentials can be mathematically expressed as in **Eq.11**.

$$\zeta = \phi_0 \times \left(1 + \frac{l_{slip}}{\lambda_D} \right) \quad (11)$$

But what does **Eq.9** points out? It says that the velocity magnitude of a fluid inside a nanopore depends on the equilibrium between an electrical force, which drives the system, and the antagonist friction force developed at the inner walls interface. This balance per unit area writes:³³

$$\eta \frac{v_{\infty}}{\lambda_D + l_{slip}} \sim e\Sigma \times E_{app} \quad (12)$$

with σ being the surface charge density (C/m^2). The **Eq.12** point out that in the slippage condition the velocity gradients develops for a distance

from the surface equal to $\lambda_D + l_{slip}$ thus enhancing the fluid flow. Presenting some usual values for these two parameter, it is immediate to notice how much large this enhancement could be. As presented previously λ_D ranges from 1 nm up to 60 nm while l_{slip} has been reported to be equal to 30nm in hydrophobic surfaces. A clear sketch is presented in **Fig.18**

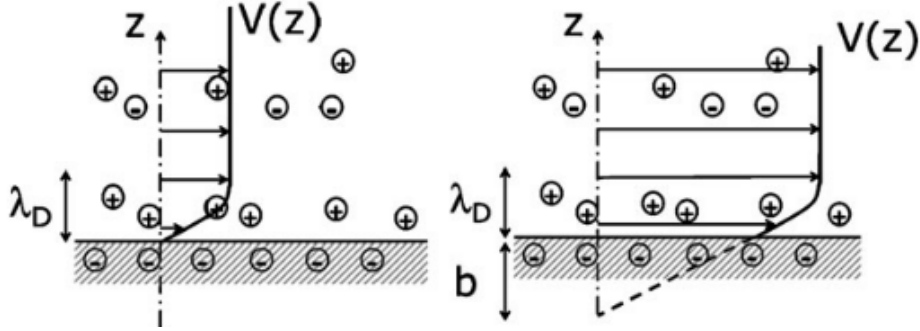


Figure 18: *slippage effect on the electro-osmotic flow. The viscous friction in the EDL is reduced, as the hydrodynamic velocity gradient develops on a larger length $\lambda_D + l_{slip}$. Flow is accordingly enhanced by a factor $1 + \frac{l_{slip}}{\lambda_D}$*

Once again a phenomenon obtained at the nanometric scale combined with a controlled surface physico-chemistry used to improve and control the electro-osmotic transport suggests that this is the correct way to pursue if one wants to reach larger efficiency of energy conversion devices based on electrokinetic effect.^{46,47}

3.2.2 Surface Conductance

By general definition it is known that the conductance (G) of a system characterise the relationship within the measured electrical current and the applied voltage. In this workframe it particularly describes the number of free ions that actually build up the ionic current inside the channel. Knowing so one could thus expect that it directly depends on the ionic strength of the salt ρ_s , thus naively owing all the conduction process just to the bulk component of the system. Nevertheless as introduced by Stein et al.³⁹ even in a nanochannel it is also possible to calculate a supplementary influence of the surfaces on the overall conductance. Having already introduced the concept of Dukhin length that, just to resume quantifies

the competition between a bulk or surface-driven conductance, it is easy to imagine that in whichever system whose confining dimension is smaller than $l_D u$, the surface conductance totally dominates over the bulk conductance, scaling some of the related effects even at larger dimensions, but more importantly noticing that this condition does not depend on the Debye layer overlap. Experimentally this effect is translated in the saturation of the conductance especially in the low salt concentration regime, as presented in **Fig.17**

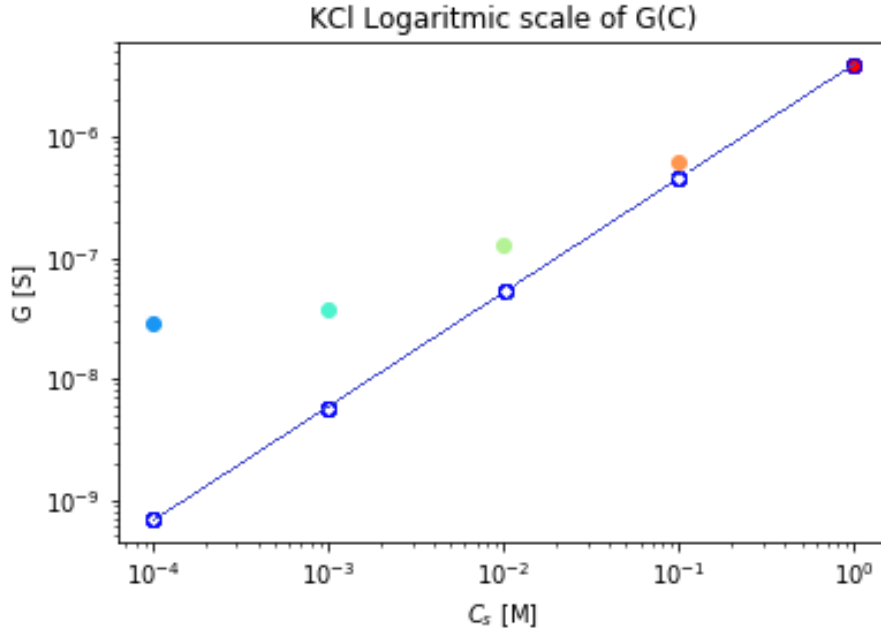


Figure 19: $G [S]$ vs $C [M]$ curves for a hBN nanopore. $D = 55\text{nm}$, $L = 10 \text{ nm}$, $\text{pH} = 10.6$, number of pores = 9. The blue line represents the classical bulk-driven conductance without considering any surface conductance effect (**Eq.43**). The colored dot instead represents the experimental conductance extracted from the device's analysis.

The saturation effect originates in the quantity of free ions directly attracted by the surface charge Σ , the number of which is of course independent of the salt concentration. In general, after some math, one could write that G can be described by an equation of this type:

$$G = 2e^2 \rho_s \mu A (1 + C_G) \quad (13)$$

Where A is the the channel cross-section and C_G represents a correction

term for the conductance that takes into account also the surface influence.

$$C_G = \cosh\left(\frac{eV_c}{k_B T}\right) - 1 + \frac{\epsilon}{4\rho_s k_B T r} \left(1 + \frac{1}{2\pi l_B \mu \eta}\right) \quad (14)$$

Where V_c is the electrical potential at the center of the channel and ϵ in this case represents the electrostatic energy. Now considering the main three length scales in the nanofluidic framework and the ultra-low salt concentration regime, thus with $\rho_s - > 0$, also recovering the value given in the dedicated chapter, it is possible to express that:

$$l_{GC} < \lambda_D < l_{Du} \quad (15)$$

$$\frac{\lambda_D}{l_{GC}} = \frac{l_{Du}}{\lambda_D} \gg 1 \quad (16)$$

The saturation will occur when the channel confining dimension will be smaller than l_{Du} independently on the order of the EDL extension and overlap, and in particular at a value of:

$$G_{sat} = 2e^2 \mu \frac{r}{t} |\Sigma| \left(1 + \frac{1}{2\pi l_B \mu \eta}\right) \quad (17)$$

From this discussion two important remarks must be pointed out in the same philosophy of the previous chapters. First is that, once again, the surface electrical properties determined via the the surface charge Σ determine a further degree of freedom and new strategies in the external control and tuning of the nanochannel's transport properties, as done for instance by *Karnik et al.*³⁵ in the microfluidic transistor development, or as *Siwy et al.*⁴⁸ or *Yeh et al.*⁴⁹ in the much more interesting nanofluidic diode harvester. Second that the surface conductance contribution can be enhanced by the slippage effect with a new contribution of:

$$G_{slip} = 2e^2 r \frac{\Sigma^2}{\eta} l_{slip} \quad (18)$$

And just to give an order of magnitude of the enhancement, if one consider the $\frac{G_{slip}}{G_{sat}}$ ratio knowing that $G_{sat} \sim \mu \Sigma$ (with $\mu \sim d_{ion}^{-1}$) and $G_{slip} \sim$

l_{slip} , then it is clear that:

$$\frac{G_{slip}}{G_{sat}} \sim |\Sigma|d_{ion} \times l_{slip} \sim \frac{l_{slip}}{l_{GC}} \quad (19)$$

Being the l_{GC} nanometric or even sub-nanometric, the enhancement factor becomes very large. But what does this directly imply? It means that having a higher conductance on the contrary the channel's resistance is reduced of the same amount bringing interesting results and further trade-off to consider in the context of the electrokinetic energy conversion.

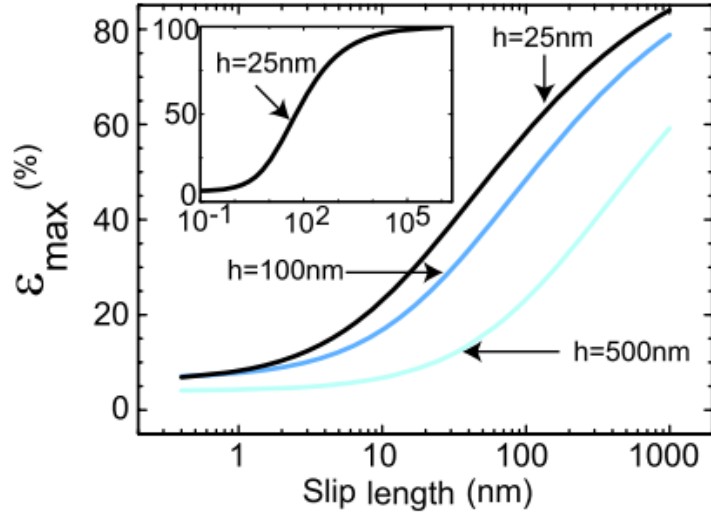
3.2.3 Enhanced energy generation efficiency

At the end of the previous chapter it was pointed out the importance of the ion-specific surface transport in relation with the energy generation efficiency. In my opinion could be interesting to better understand why and grasp these concepts, even just by the means of a theoretical analysis. Prior to the advent of the outstanding 2D materials and the creation of new nanofabrication or chemi-variation techniques, the energy conversion efficiency registered in the common used Silica nanochannel had not surpassed the range from 3% to 7%.⁵⁰ Therefore an increasing will to understand which nanofluidic mechanisms could help in refining those values has been continually funding the research in this field. For the first time it was theorized that an energy conversion efficiency of the 35% could have been achieved by the slip at charged surfaces due to a higher advection of counterions.⁴⁷ In [46] another reason has been theorized. Increasing the slip length practically means that the electrical resistance R_{ch} is reduced (lower power dissipation through joule effect) and opposite the streaming conductance S_{str} increased. These two parameters, which appear in the linear relation of the ionic current I in **Eq.20** and flow rate Q in **Eq.21**, particularly depends just on the nanosystem geometry, surface charge distribution and the fluid flow within it.

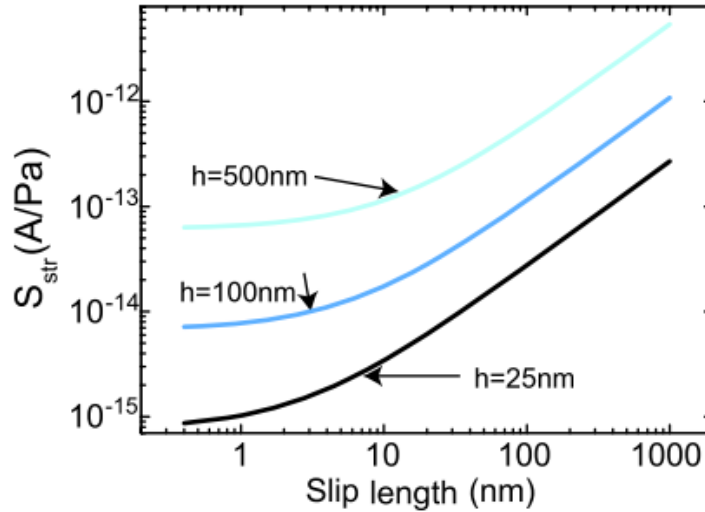
$$I = S_{str}\Delta p + \frac{\Delta V}{R_{ch}} \quad (20)$$

$$Q = \frac{\Delta P}{Z_{ch}} + S_{str}\Delta V \quad (21)$$

In the following plots, particularly **20(b)**, it is also possible to appreciate that When the fluid near the wall acquires a finite velocity, depicted with an increasing slip length, the high concentration of counterions there can contribute to the streaming conductance.



(a)



(b)

Figure 20: Slip-length dependence of electrokinetic transport and energy conversion efficiency, parametrized for different channel heights in low salt regime

In **Fig.21** instead it is shown that in the case of no-slip, S_{str} increases with Σ because this determines that the whole channel is fulfilled by more

counterions, nevertheless this increase saturates somewhat at higher Σ , this latter behaviour could be explained by the fact that all the additional counterions are collected in a very thin layer directly near the charged surface, this means that in a no-slip condition they will be weakly or not advected at all, thus not contributing to the overall energy conversion.

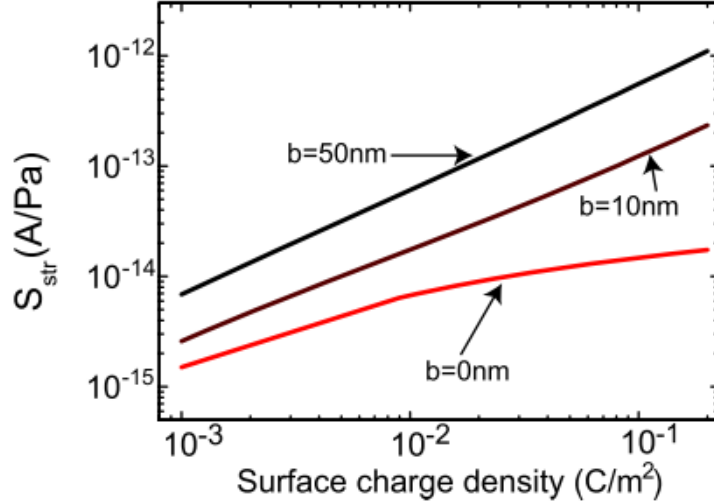


Figure 21: Surface-charge dependence of energy conversion efficiency

Furthermore it must be pointed out the presence of a certain peak in the efficiency plot. This express the subtle competition between the efficiency gain, from the increasing counterions advection in the EDL, and the antagonist increased resistive dissipation caused by those additional ions, whose are actually the electric resistance R_{ch} .

$$P_{diss} = \frac{V^2}{R_{ch}} \quad (22)$$

It is now more clear how many side parameters enter in the game and must be accurately engineered when one wants to find the best trade-off.

3.3 Device's Physics - Reverse Electrodialysis

In this section are described the main working principle of a typical Reverse Electrodialysis Harvester (REDH), and all the physical effects related to the transition of an ion's flow within a nanometric channel, which finally

bring to the harvesting of a usable electrical power.

The mechanism of the RED device with nanofluidic channels or nanopores is sketched in **Fig.22**:

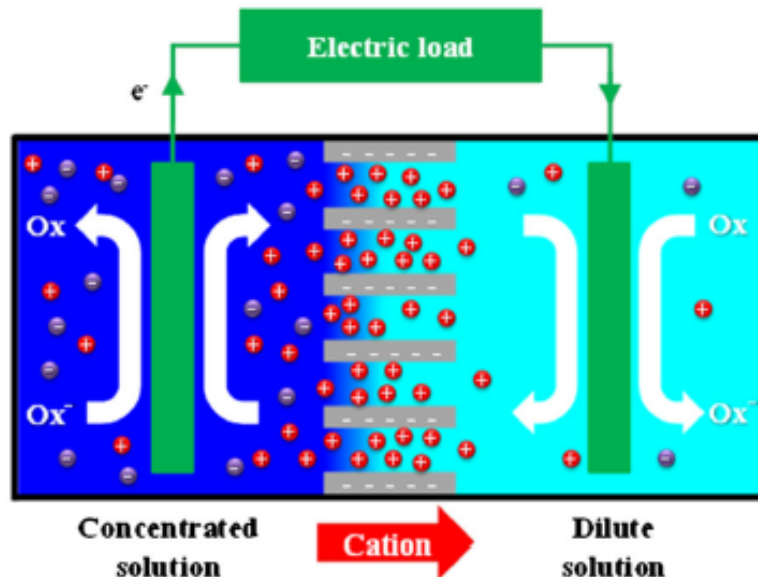


Figure 22: Basic illustration of a RED cell

A typical design of a RED cell involves a salinity gradient between two tanks separated by a membrane, with single or multiple nanochannels that permits the selective passage of ions from a side to the other, thus directly generating an ionic currents by separating the corresponding ion fluxes. It is thus evident that the whole general mechanism is based on the separation of ions from water, and therefore it is required a subnanometric filtering structure, which does not permit the easy flowing of water fluxes and as a result diminishes the total energetic efficiency. Nevertheless the first state-of-the-art RED system it was reported to achieve up to $8W/m^2$ in a specific laboratory controlled environment.⁵¹ Furthermore as already pointed out many and many times in the past chapters the usage of new nanomaterials, such as Graphene, Boron Nitride (BN) or Molybdenum Disulfide (MoS_2), and novel nanofluidic transport effects constitute new important tools that allow to boost the overall performances of many orders of magnitude.

To grasp a more physical insight, as a general picture, it can be initially

said that considering a linear behaviour, an internal electromotive force ϵ_{osm} (known as *Osmotic Potential*) generates a driving force through the whole nanochannel, which is characterized by a proper conductance G_{osm} , thus producing as a result of the action of this force an osmotic current I_{osm} , intimately related to the previous quantities by the usual Ohm's Law. The driving force, of course, directly derives from the mixing of the two salt solutions at different concentration and on the selectivity of the system. In ideal solutions this can be easily described in the framework of the *Donnan equilibrium* and by the means of the Poisson-Nernst-Planck (PNP) equations, which will be presented in the following chapters.

3.3.1 Donnan equilibrium

As already presented in the chapter regarding the Debye length, when a charged solid interface, the nanochannel in this case, is immersed in a liquid determines the build up of a potential difference between the inner surface and the solution reservoirs. This process is mainly due to the necessity of maintaining a spatially constant ion's chemical potential, in analogy with the uniform Fermi level in a semiconductor. If one assumes a dilute ion system the chemical potential $\mu(\rho)$, both for the anions and cations, can be mathematically expressed as:

$$\mu(\rho) = \mu_0 + k_B T \log(\rho_s) \quad (23)$$

ρ_s being of course the salt concentration in the reservoirs. Considering then the electroneutrality condition of the system, it can be written that:

$$\int_{-d/2}^{+d/2} (\rho_+(z) - \rho_-(z)) dz = 2\Sigma \quad (24)$$

being z the radial direction, as sketched in **Fig.23 (a)**

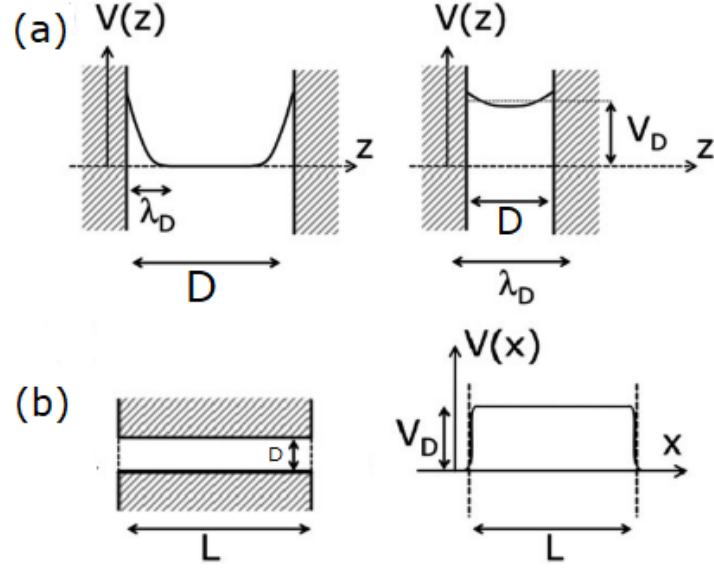


Figure 23: (a) Representation of the electrostatic potential $V(z)$ in a charged nanochannel. The left image represent a non-overlapping condition ($D > 2\lambda_D$), while the right one the EDL overlap ($D < 2\lambda_D$) (b) A charged nanochannel, with diameter D and length L . In the EDL overlap condition, a Donnan potential V_D builds up along the nanochannel.

Considering now the EDL overlap condition, which happens when $D < 2\lambda_D$, it is reasonable to assume that both the ion distribution and the electrostatic potential are spatially constant all over nanochannel thickness. For the ions densities it is possible to write:

$$\rho_+ \times \rho_- = \rho_s^2 \quad (25)$$

$$\rho_+ - \rho_- = \frac{2\Sigma}{D} \quad (26)$$

obtaining as a final result an ion density and a Donnan potential V_D expressed as:

$$\rho = \sqrt{\rho_s^2 + \left(\frac{\Sigma}{D}\right)^2} \pm \frac{\Sigma}{D} \quad (27)$$

$$V_D = \frac{K_B T}{2e} \log\left(\frac{\rho_-}{\rho_+}\right) \quad (28)$$

The presence of this potential difference determines the arising of many interesting effects, one above all which is particularly interesting in this work is the tunable and controllable Permselectivity of the system. Furthermore from a pure physical point of view, it is very interesting to remark the close analogy that exist within the Donnan equilibrium theory and the equilibrium of carriers in doped semi-conductors. In the SCs theory the electron (n_n) and hole (n_p) densities are described by **Eq.25** aswell, while the electrolyte density is replaced by the total carrier density in the intrinsic semiconductor (n_0). The surface charge in the nanochannel is actually acting as the added dopant that furnish additional impurities, N-doping if $\Sigma > 0$ and P-doping if $\Sigma < 0$. The Donnan potential finally represents the analogous of the shift in the Fermi energy toward the valence or the conduction bands due to the impurities addition, which determines the building up of a net voltage difference at the equilibrium between regions of different doping level.

3.3.2 PNP equations

Recovering the EDL overlap condition ($D < 2\lambda_D$) and imposing some assumptions, such as treating the flowing ions as a perfect univalent gas and not considering the ion-ion correlation, it is possible to write a set of equations that describe the motion of those charged particles in a confined space. Must be underlined that the confinement should always be larger than the continuum limit ($D > 1 - 2nm$) to ensure the validity of the assumptions above.

Describing the anion and cation fluxes as:

$$J_{\pm} = -D_{\pm}\partial_x\rho_{\pm}(x) \pm \mu_{\pm}e\rho_{\pm}(x)(-\partial_x V(x)) \quad (29)$$

with D and μ related one to other through the well-known Einstein relation:

$$D_{\pm} = \mu_{\pm}k_B T \quad (30)$$

Considering x as the direction along the nanochannel's axis, as described in **Fig.23(b)**, it is possible to rewrite the local formulation for the

electroneutrality **Eq.26** simply as:

$$\rho_+(x) - \rho_-(x) = \frac{2\Sigma(x)}{D} \quad (31)$$

Remembering that thank to the EDL overlap a uniform V_D built up along the channel due to the uniform ion density, if now a perturbation of electrical or chemical nature is actively imposed to the nanochannel within the two reservoirs, such a ΔV or $\Delta\rho_s$, the ion fluxes will naturally change in order to counteract the perturbation and to reach a new equilibrium condition. When the stationary state is reached, thus it is not present any change with respect the flowing time, the ion flux is spatially uniform, permitting to solve both **Eq.29** and **Eq.31** for ion densities and local potential. At this point the generated current $I = Ae(J_+ - J_-)$ and the overall Ion flux $\Phi_T = A(J_+ - J_-)$, where A is the nanochannel cross-section, can be computed as-well, and if one consider the limit of small perturbation regime a linear relation may be extracted with the resultant ionic fluxes and the thermodynamic 'agents' that caused them:

$$\begin{bmatrix} I \\ \Phi_T \end{bmatrix} = \frac{A}{L} \begin{bmatrix} K & \mu_K \\ \mu_K & \mu_{eff} \end{bmatrix} \begin{bmatrix} -\Delta V \\ -k_B T \log \frac{\Delta\rho_s}{\rho_s} \end{bmatrix} \quad (32)$$

In the same philosophy of the chapter above, it is interesting to notice some relations to the semiconductor basic theory. The **Eq.29** is mathematically the same as the typical transport equations for electrons and holes in a semiconductor. This practically implies that, as long as any possible fluid flow or convective term is neglected, nanofluidic devices can theoretically reproduce standard semiconductor devices. In literature there are plenty of example regarding the microfluidic transistor, nevertheless the intrinsic performances of a fluidic system make it totally worthless if compared with solid state semiconductor-based transistors. Totally different is instead the importance of a microfluidic diode related to the osmotic power generation field, recently theoretically studied and simulated by many groups, whose found many interesting results regarding power generation and energy efficiency boosting, still need to be analyzed experimentally. That is why in my project I also included such structure in my nanofabrication process flow and performed some experiments on it. As presented in the *Measurement* chapter.

3.3.3 Power generation

In this chapter I would like to present a practical situation in which the understanding of the Donnan equilibrium theory and the PNP equations actually help us to describe the basic principle on which the whole RED system, as per already said countless times, is completely based to generate usable energy. It is needed to start from a more general equation that describes the ionic flux of i ion species, each one with its own valence z_i and concentration c_i :

$$J_i = -D_i \left[\nabla C_i + \frac{z_i e c_i}{k_B T} (\nabla V) \right] + c_i v_i \quad (33)$$

where the first term of the equation represents the concentration gradient describing the diffusio-osmotic process, the second one the electro-osmotic process when applying an external potential difference and the last term instead related to the ion convection linked to the flowing of the fluid. As already pointed out before if one wants to solve the PNP equation and find linear cause-effect relationship, when applying external perturbations, it is needed to neglect the fluid flow, cancelling out the last term from the above equation. The system taken into account is the usual one, composed by the two reservoirs with a symmetrical salt solution at different concentration (first perturbation; $\Delta\rho_s$) divided by a charged nanopore, which acts as an electrostatic charge filter, and with two electrodes through which it is possible to impose an external potential (second perturbation: ΔV) as depicted in **Fig.24**

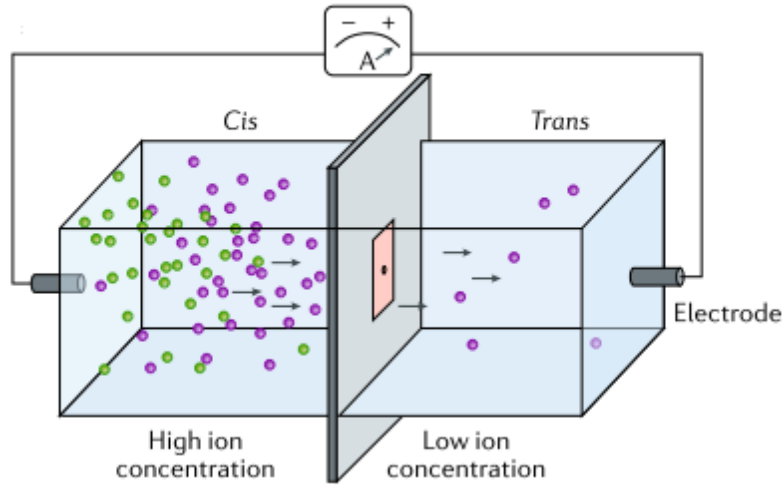


Figure 24: Typical RED system composed by two reservoirs, two AgCl/AgCl electrodes and SiN free-standing membrane (Blue square) with a 2D-material nanopore (Pink square) used as a selective channel

Ions with the same charge as the nanopore surface presents a lower permeability, being of course electrostatically screened out as depicted in **Fig.26**, while ions of the opposite charge can be described by a higher permeability. This permselective transport is a direct consequence of the building up of the Donnan potential due to the presence of a non-null surface charge owing to a depletion or an enrichment of co-ions and counter-ions all along the channel, as sketched in **Fig.25**

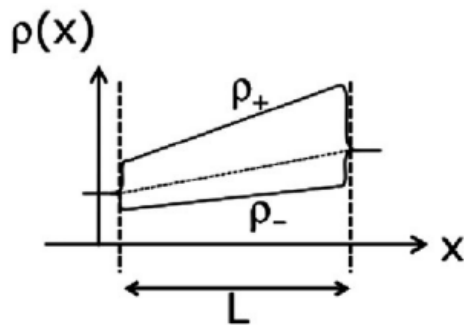


Figure 25: Concentration profile of co-ions and counter-ions inside the nanopore when in presence of a negative surface charge

Due to the difference in ion permeability throughout the channel, a charge separation process will be generated within the two reservoirs. As

a result to maintain the overall equilibrium, imposing also a condition of electroneutrality to the system, one obtains the generation of reacting electric field, proportional to logarithm of the local ion concentration, which dynamically compensate the selective passage of charges. It can be expressed as $E_{reac} = \nabla \log(c(r))$.

From this, by integrating, it is possible to recover the expression for the potential difference at the membrane's sides:

$$\epsilon_{osm} = \frac{k_b T}{ze} S \ln \frac{c_h}{c_l} \quad (34)$$

where $S = \frac{D_+ - D_-}{D_+ + D_-}$ describes the ion selectivity of the system, which can be expressed also in term of the transference number t , while D_+ and D_- represent the effective diffusion constant for cation and anion respectively. It is easy to understand that if the two effective diffusion constants are equal, because the system is not selective, the osmotic driving force for the energy production will be null, thus all the Gibbs free energy of mixing is converted into thermal energy (heat dissipation). If instead the nanochannel is ion selective, then it is possible to have a net flux of one charged ion specie larger than the other hence producing a non-null potential difference acting as a battery. This very asymmetric ion exchange process leads to an electrochemical red-ox reactions directly on the electrode surfaces (Ag/AgCl) to maintain the global electroneutrality of the solution. Indeed electrons are consequently transferred to an external electrical circuit, actively producing electrical power.⁵²

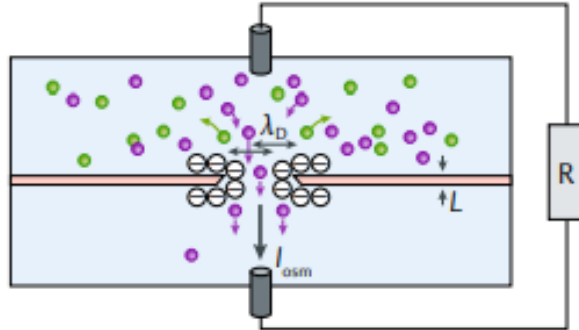


Figure 26: EDL overlapping for Ion Selectivity in a nanopore system

3.3.4 Ion selectivity

From the previous paragraphs it was possible to grasp the importance of the Ion selectivity under a salt gradient and its response to the driving force G_{osm} regarding the osmotic power generation defined through the extracted osmotic current and the resulting osmotic potential. It is also now clear how this important parameter is intimately related to the electrostatic screening length and surface charges, thus in general mainly from local salt concentration and the solution pH for instance. Generally selectivity is inversely proportional to the pore diameter, directly proportional to the pore length and the surface charge density.^{26,30} Selectivity also directly influences one of the two most important performance parameter when talking about energy harvesting, the energy conversion efficiency η , as a rule of thumb it is proportional to the square of the selectivity $\eta = S^2/2$ Furthermore just to recover something that was already presented previously if one writes the equation for the maximum generated power:

$$P_{max} = \frac{1}{4} \times G_{osm} \epsilon_{osm}^2 \quad (35)$$

And considering that as a first approximation the osmotic potential equation can be expressed as:

$$\epsilon_{osm} = \frac{K_B T}{Z e} S \ln \left(\frac{C_{high}}{C_{low}} \right) \quad (36)$$

It directly comes that higher is S, higher will be the resulting ϵ_{osm} thus directly increasing the maximum power density.

4 Nanofabrication

In this chapter are described and showed all the fabrication steps needed to obtain the atomically smooth ultra-short nanochannels, the exploited instrumentation and their general working principle.

To better understand the following description regarding the entire nanofabrication process flow, in **Fig.27** it is sketched the basic model of a completed device that shows a Graphite/Graphene flake on top of a SiN opening (could be circular or slit-shaped). In **Fig.28** instead are presented two different shape's solutions for the TEM (Left) or EBL (Right) drilled nanochannel.

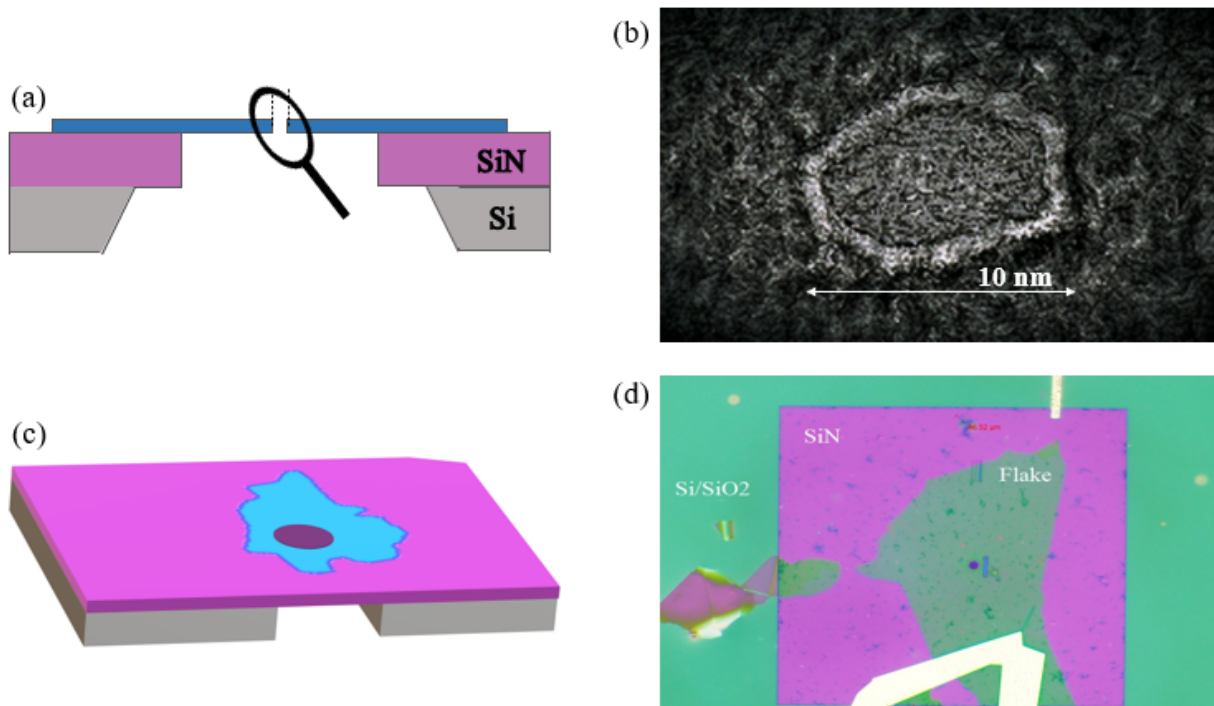


Figure 27: (a) Sketch of the completed device formed by a Graphene flake on top of SiN membrane (violet) backside-etched on a Si/SiO₂ substrate (grey). (b) TEM image of the drilled nanopore. (c) 3D representation of the triple Si/SiN/Graphene stack (d) Filtered light optical micrograph of a completed device.

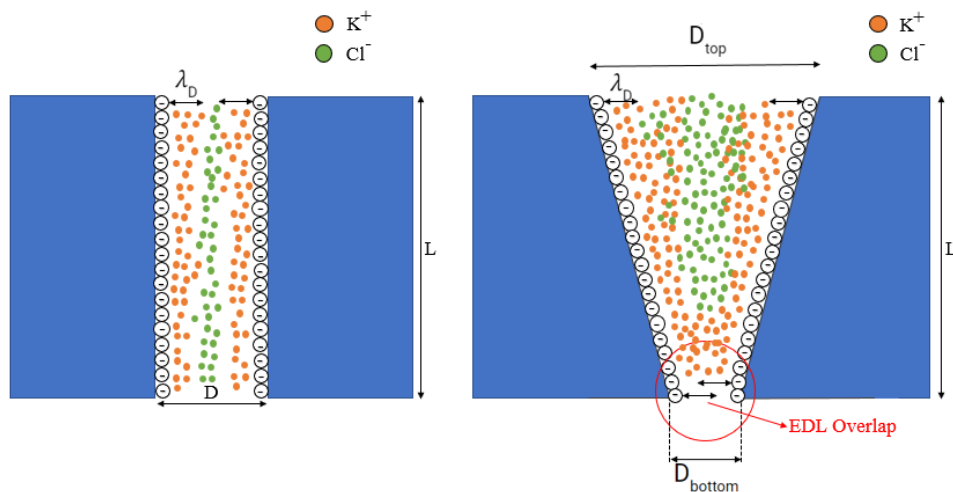


Figure 28: Sketch of the two specific shapes that one can use to obtain power generation. (Left) Cylindrical symmetric cross section. (Right) Conical asymmetric cross section

4.1 Graphite mechanical exfoliation

The first thing to do is the mechanical exfoliation of the graphite. This initial step, even if it could appear simple and straightforward, is absolutely crucial to obtain flat and high-quality graphene or graphite flakes. This pretty explain why every single laboratory, that deal with graphene, exploits very different techniques in order to reach the best possible quality accordingly with their own lab environment and application.

Among many techniques that include: **sonication** of a solution containing graphite crystals in form of powder⁵³, the use of particular chemicals to effectively peel layers from the bulky structure known as **chemical exfoliation**⁵⁴, or some *bottom-up* approaches such as the well-known **chemical vapor deposition**⁵⁵ or the **flash Joule heating**.⁵⁶

Since we perform fundamental research, where the ultra cleanliness for each process is the main priority, followed by the necessity to have and ensure always a defect-free or crack-free flake, it was preferred to exploit the following simple, clean and effective method.

Starting from a piece of bulky graphite, this is cleaned with a controlled nitrogen blow dry technique and then the first 4 to 5 initial layers carefully removed.

Once the preliminary preparation is done, it is placed inside a rectangular-shaped piece of adhesive plastic blue tape (PVC made by Ultron Systems, inc.), it is important to underline that the tape is Silicon-free to ensure a cleaner process and more consistent adhesive properties.

At this point the graphite is pressed against different spots of the tape and exfoliated directly there, when finished all the film is consequently forced against the substrate for about 3 minutes as depicted in the following image:

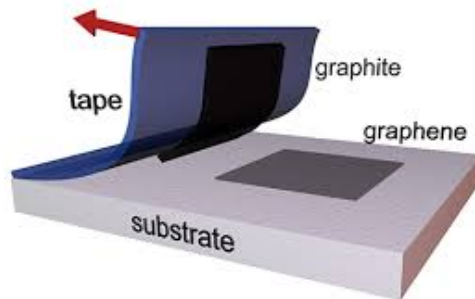


Figure 29: *example of a direct graphite exfoliation on a Silicon substrate*

Waiting some minutes helps the thin graphite flakes to properly adhere onto the substrate and enhance the probability to do not detach them during the film peeling-off or crack them into pieces, due to a possible partial attachment. To further avoid any of the issues presented before, it is suggested to remove the tape with a low contact angle keeping it always at the maximum tension.

4.2 Flake's optical check and selection

It is important to underline at the very beginning that, finding small graphene's flakes within of millions of thicker graphitic ones is both extremely difficult and time consuming. That remains true even using alternative modern visualization techniques such as: Atomic Force microscopy, Scanning Electron microscopy or Electron microscopy.

Actually, as discovered and studied by Novoselov, Geim, Castro Neto et al.⁵⁷ the fastest way to optically isolate graphene is to exfoliate graphite chunk directly on top of a 100-300 nm thick oxidized Si wafer (Si/SiO_2

stack) and then scan its surface at the optical microscope with the proper light filter activated. As pointed out in the paper the 100 nm thick SiO_2 wafer are most suitable for its visual detection that is made even clear when paired with an optical filter that select light with a wavelength comprised in a range of 380-500 nm. Once the exfoliation step is over, as anticipated above, it is possible to directly check the result at the optical microscope. The first thing to do is setting the virtual axis origin at the top left corner of the chip, that is a useful passage to retrieve easily the position in a second moment. After that, just moving the stage by means of the dedicated knobs, the proper optical check starts. In **Fig.30** are presented some images taken from samples with different thicknesses:

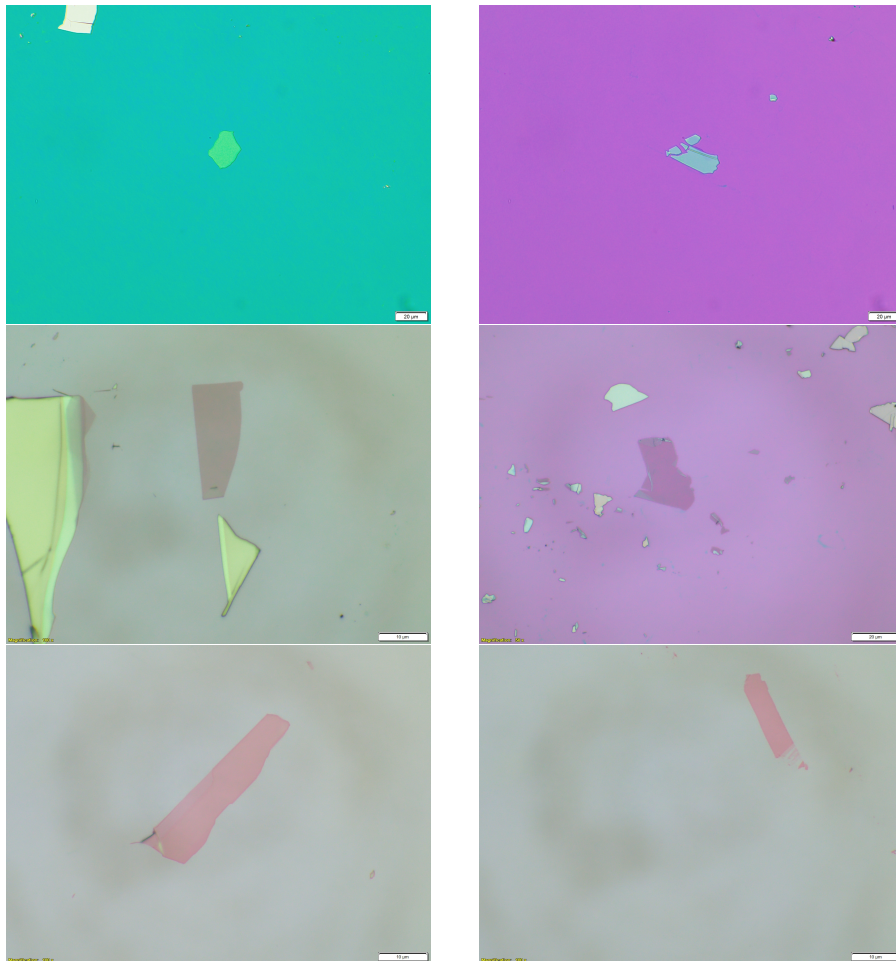


Figure 30: Optical images at 50x and 100x magnification of different chosen flakes for the creation of the final devices

The selection is done taking into account the presence of the defects (minimal possible number), cracks and impurities, which may be analyzed through the Dark Field setting of the microscope, but also taking into account the estimated thickness of the flake and the required geometrical dimensions (width, length, area), which may be extracted by a simple atomic force microscopy image and the use of a specialized software, as presented below.

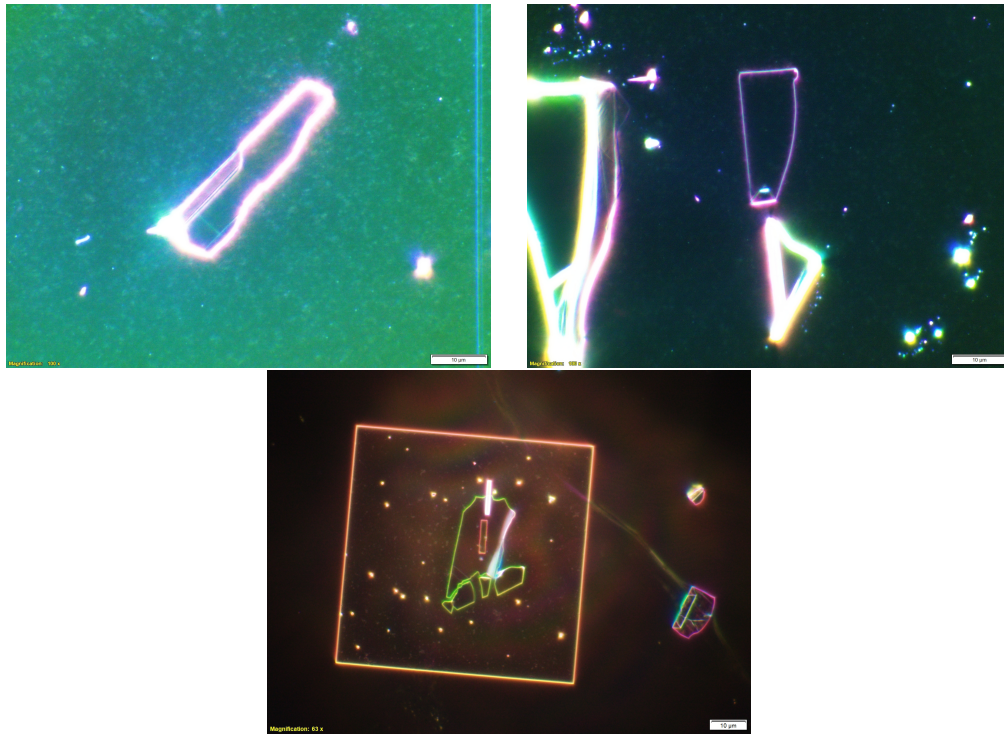


Figure 31: *Optical images in Dark Field configuration at 50x and 100x magnification of different chosen flakes for the creation of the final devices*

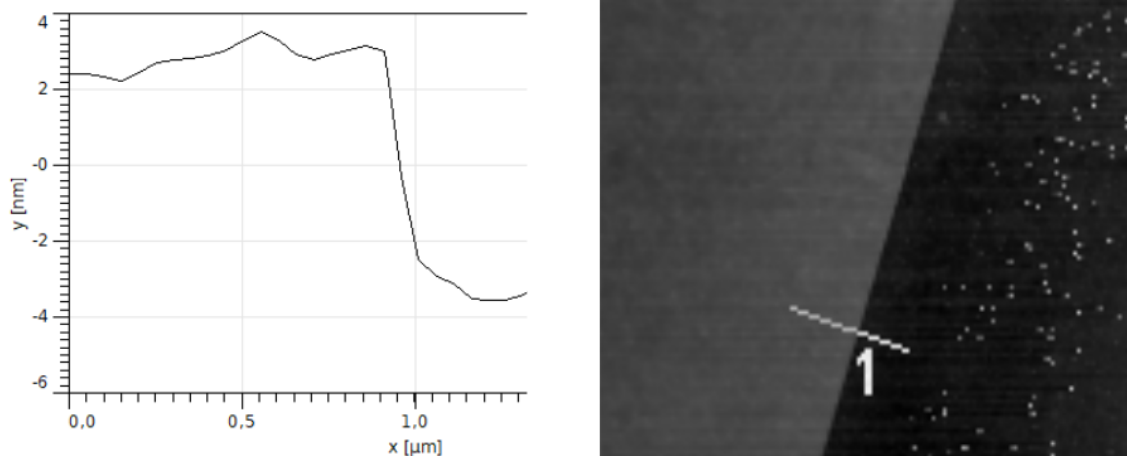


Figure 32: *AFM height images for thickness and geometrical parameters extraction*

4.3 2D Material manipulation and transfer

At this point it is necessary to transfer and place in a deterministic way the chosen flake on top of the prepared SiN membrane, taking care of covering the entire etched slit or aperture.

The manipulation and placement of any 2D material relies intensively on polymer science and its polymeric-based compounds. Within many examples of so often used polymers we may find the polymethylmethacrylate (commonly known as **PMMA** and the Polydimethylsiloxane (**PDMS**). Of course accordingly to the field of application or the results needed for the fabrication of specific micro and nanostructures it is possible to find many other examples as well as an incredibly wide range of transfer techniques with their own advantages and drawbacks.⁵⁸ Despite the interesting characteristics of each one of those processes, which would deserve a separate chapter, for the sake of concision, only the main two methods directly used during the nanofabrication process flow will be described in detail.

4.3.1 PDMS manual dry transfer

The former process that is going to be described is called "PDMS Manual Dry Transfer", it is very fast, simple but not extremely clean.

Before going deeply into the description of this type of transfer it is important to give some generic information about the PDMS.

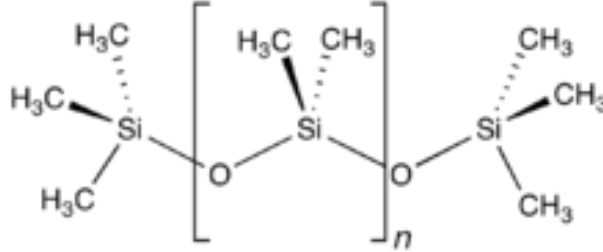


Figure 33: PDMS structure. Chemical formula: $(C_2H_6OSi)_n$

It is a polymeric silicon used in many field for its mechanical and physical properties, its non-toxicity and easy formation. In fact the PDMS is obtained by mixing elastomers with a so called "curing agent" that defines the number of cross-links between the basic monomers. The mixing ratio of those two elements characterizes the material and its final properties.

Prior to the actual dry transfer itself, as a needed preliminary action it is required that the graphene/graphite flakes need to be exfoliated and pressed against a micrometric thick PDMS substrate instead of the conventional Si/SiO_2 stack. Contrary to what was expressed previously, the flake release onto the PDMS slab must be performed very quickly and with a high contact angle. It is so because after many tryouts, we found out that the best flake's quality is obtained only with a fast peeling and minimum thumb pressure.

The PDMS is consequently allocated inside the sample holder of a manually controlled arm in and then the surface with the flakes is slowly and gently put in a conformal contact with the membrane. Since this technique deals with micrometric samples all the procedure is optically checked by means of an optical microscope at 20x/50x magnification.



Figure 34: *NUS cleanroom's manual transfer station*



Figure 35: *summary sketch of PDMS dry transfer*

4.3.2 PMMA Semi-automatic Dry Transfer

This latter process, if compared to the previous one, is much more time consuming and complex to perform, but presents also the highest level of cleanliness and environmental control.

In order to be performed it needs a dedicated type of wafer substrate, which cannot be PMDS or a simple Si/ SiO_2 stack.

In this case it is needed to prepare a triple stack substrate made of from top to bottom: PMMA, polydimethylglutarimide (**PMGI**), Silicon.

The PMGI is a particular resist that permits to have a high yield during both film or metal lift-off processing. The PMMA instead is a transparent thermoplastic used in the nanotechnology industry in film form as a incredibly lightweight and biocompatible alternative to glass or as a positive resist in electron beam lithography.

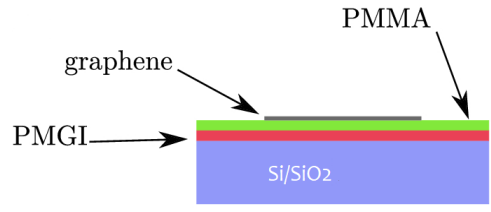


Figure 36: *Si/SiO₂ and PMGI/PMMA triple stack*

The process starts by engraving a circle all around the optically inspected and chosen flake by means of very sharp tip. The right dimension of the circle is given by the 5x magnification lens of the microscope.



Figure 37: *Particular of a circular scratch around the chosen flake*

Once the circle is completed a droplet of a PMGI developer, Microposit MF-319, is released on top and all around the scratch, paying attention to not "flood" the flake's area. This starts slowly to spread underneath the PMMA thin layer and dissolving the PMGI layer.

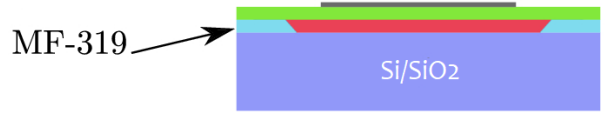


Figure 38: *PMGI dissolution example*

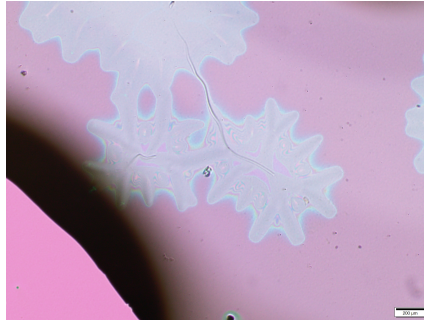


Figure 39: *PMGI solvent spreading under the PMMA thin layer*

The PMGI dissolution permits the formation of a free-standing PMMA membrane

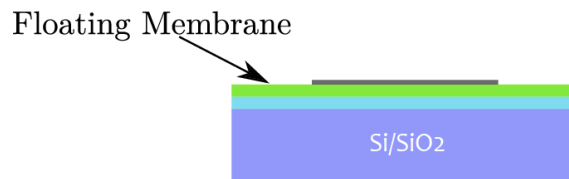


Figure 40: *example of a free-standing PMMA membrane*

this step occurs relatively fast and it's possible to analyze it directly at the optical microscope as seen in the following images:

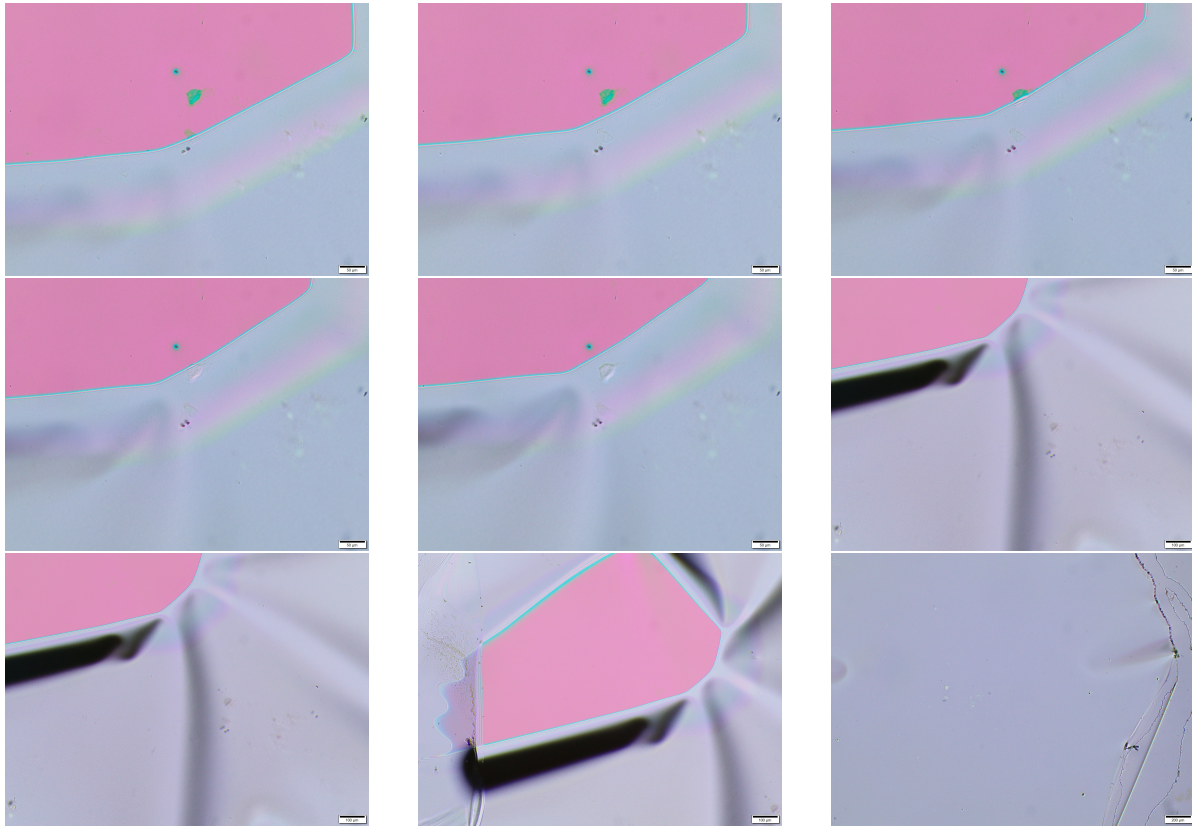


Figure 41: *Images sequence of a PMMA free-standing membrane formation*

at this point the membrane is ready to be released on top the deionized and purified water (DI), floating on the DI's surface still uncontaminated like depicted below

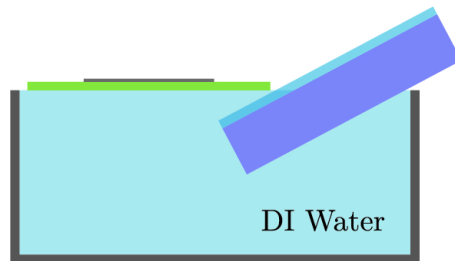


Figure 42: *Floating membrane release in deionized water*

and consequently "fished" by means of a circular metallic support, which was previously cleaned in a sonicated bath of respectively Ethanol, IPA and DI.



Figure 43: *Floating film "fishing"*

At this point the metallic ring is placed inside a vacuum-sealed Glove Box Transfer Station and manipulated by means of automatic microactuators until it is pressed against the SiN slit, ensuring the best precision and cleanliness during the whole transfer.

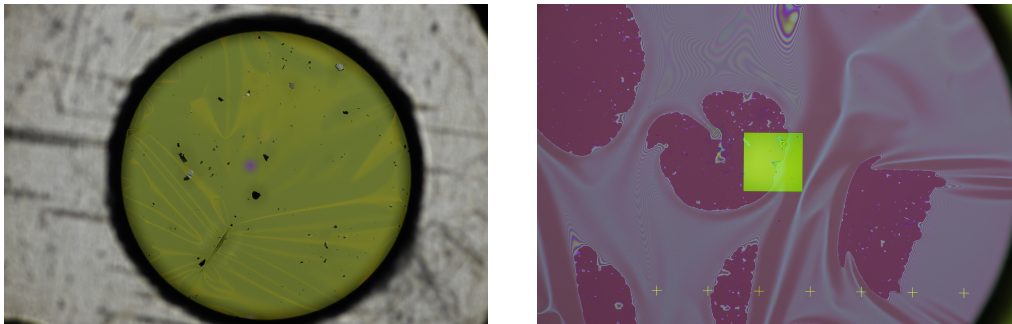


Figure 44: *PMMA film with chosen flakes inside the metallic ring (left). PMMA film transfer with semi-automatic transfer station (right)*

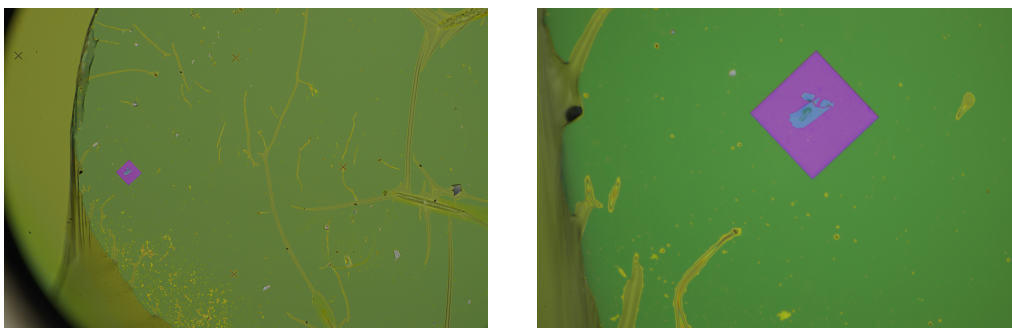


Figure 45: *PMMA film release onto the SiN slit)*

The overall transfer can also be performed both at room or at higher temperature by means of an integrated hotplate, also useful to speed up

and make the process easier to perform, nevertheless is important to remember that higher temperature means a large quantity of molten residual PMMA on top of the SiN membrane, thus mining the resulting cleanliness or requiring a loss of time due too additional cleaning steps. Finally must be said that this method is preferred because the flake never makes contact with any solvent or polymer, keeping its atomic flatness of pristine graphitic surfaces.

4.4 PMMA cleaning and spin coating

Once the transfer is completed, whether it is the semi-automatic or the manual one, a deep cleaning process is of main importance before stepping on in the process flow.

The main way to remove polymers or impurities is too perform an Acetone hot bath with a maximum fixed temperature of 65°C, this process should be done multiple times for several hours and also alternated with cold Acetone bath at room temperature. After 3 to 4 cycles of acetone cleaning it is fundamental to perform in addition a 5 minutes bath in Isopropanol (IPA), then DI thus ending with Ethanol before finally blow dry it with a nitrogen gun. This additional steps are fundamental to avoid any possible PMMA residues to contaminate the flake thus changing the electronic properties of the final device.⁵⁹

At this point the chip is ready to be spin coated with a nanometric film of PMMA that will be used as positive photoresist after the EBL lithography. The rotational velocity of the stage, the process time as well as the type of PMMA used strictly depend on the flake's thickness and on the required pattern to photoactivate. This step is performed through a spin-coater, a particular machine composed by a sample holder (where the wafer/chip can be placed) that rotates for a determined amount of time at a set velocity. In Fig.46 below is shown a typical spin-coating machine:

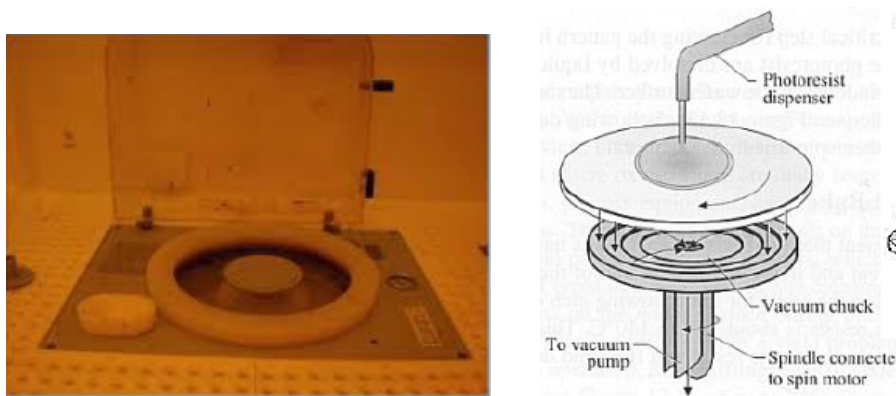


Figure 46: (Left) Spincoater used in a class 100 room of the cleanroom. (Right) Sketch of the structure of a spincoater.

The spin-coating process may be resumed in:

- **Deposition** - Delivery of a excesses of the photoresist polymer onto the substrate
- **Spin-up** - The liquids is dispersed radially toward all the location of the wafer under the centrifugal force generated by the spinning disk
- **Spin-off** - The excess liquid flies off the extremities of the wafer. It slowly thins down up to reach an uniform equilibrium thickness
- **Evaporation** - Liquid solidifies due to solvent evaporation

To obtain the wanted thickness many parameters must be properly controlled. In general the thickness can be calculated through this formula:

$$t = KS \left(\frac{\nu}{\omega^2 R^2} \right) \quad (37)$$

where K is a constant, S the fraction of solid, ν the viscosity, ω the angular velocity and R the wafer radius. The main parameter to control is of course the angular velocity (expressed in rpm) for a well defined amount of time. Usually the spinning velocity is reached after a certain ramp-up and decreased through a ramp-down period to endure a better uniformity.

4.5 Electron Beam Lithography

At this point the chip is ready to be patterned and effectively create the base for the final device.

The patterning of such materials (mainly 2D) can be achieved with a large number of techniques, simpler or harder to setup depending on the final objective, it could use directly light, electron or ion beams.

Photosensitive polymers, as the PMMA, usually tend to leave a "footprint" in form of residues on the patterned 2D material and their final resolution strongly depends on wavelength of the irradiation source. Techniques that are based on Ion or direct electron beams instead achieve a very high resolution, even down to few nanometers⁶⁰ but are harder to implement and control, owing to a poor reproducibility.

Electron beam lithography (EBL) thus appears to be the best trade-off, achieving a sub-100 nm resolution while being still flexible and much more suited for a future scaling up.

The objective is to generate a multi-layered nanopore, with a diameter of $\sim 20nm$ in diameter or even less, over a micrometric slit, in form of single conduit, array or matrix with the best precision, quality and repeatability possible. This may be done by using the Electron Beam Lithography, which up to now is considered the finest direct patterning solution in a nanofabrication process thank to its resolution that is in the range of few nanometers mainly due to electrons-substrate interactions.

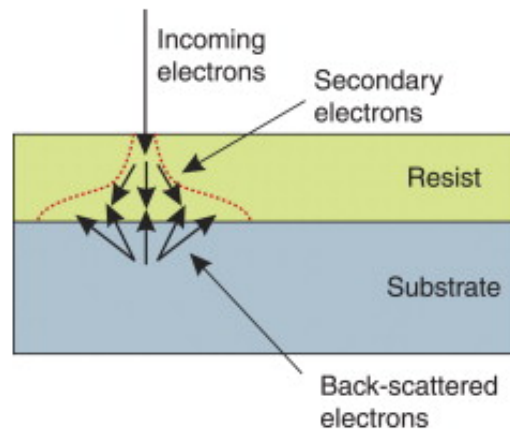


Figure 47: Simple scheme of different electrons-substrate interactions

The EBL relies on the direct exposure and alteration of a very thin positive resist (PMMA in this case) after the passage of a focused beam of fast electrons. Once the process is over the altered resist is removed by means of a so called developer in this case composed by a mixture of methyl isobutyl ketone (**MIBK**) solvent and IPA

In this case before starting the patterning of the final device a calibration step was needed. It was done on flakes and PMMA film with different thicknesses adjusting every time the exposure time, the dose and the acceleration voltage in order to obtain the desired features up to 5nm. In the following images are shown some results:

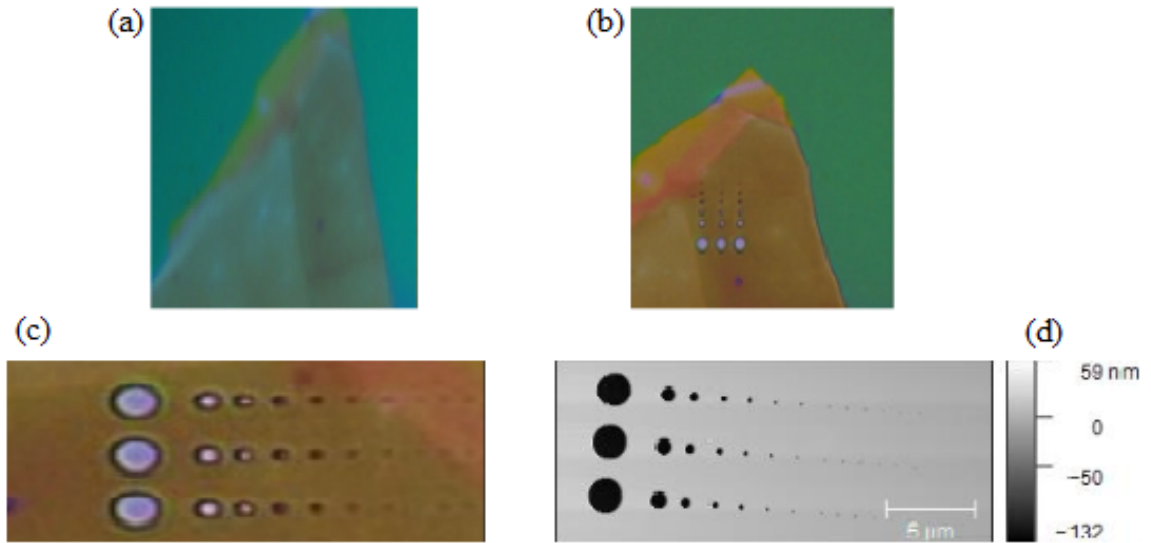


Figure 48: (a) and (b) Respectively are the optical images of the flake before and after the electron beam lithography. (c) Optical particular of the EBL-patterned nanopore's array. (d) Atomic force microscopy image of the EBL-patterned nanopore's array.

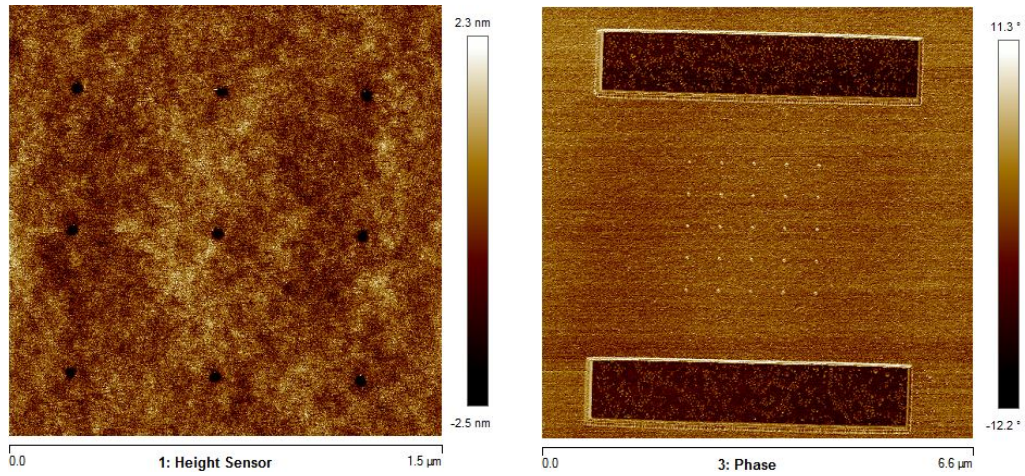


Figure 49: AFM phase and height images of nanochannels after the EBL step

4.6 TEM lithography

As already presented by *Goyal et al.*⁶¹ or by *Song Liu et al.*⁶² a valid alternative to the EBL process, always starting from the PDMS-assisted dry transfer, is the *Transmission electron microscope* (TEM) lithography. Using this technique it is possible to easily obtain graphene's nanopores with a diameter in a range of 3 to 20 nanometers, with a very high control and reproducibility. When the high-energy beam of a TEM interacts with the graphene's surface, carbon atoms are directly removed out of plane, resulting in few membrane defects. If the electron beam is thus collimated and focused on a specific zone of the graphene's flake, all these sub-nanometric defects may sum up creating what it is at the end the resulting nanopore. The acceleration energy must be properly tuned at a value of 80 keV, this permits to effectively remove the atoms out of the Graphene's lattice⁶³ whilst preventing the beam to generate any unwanted damage (pinholes, larger pores, side-ways). Anyway it was also reported that using acceleration energies above 140 keV can still produce defect free graphene's nanopores.⁶⁴

In the following images are presented some of the nanopores obtained with this process:

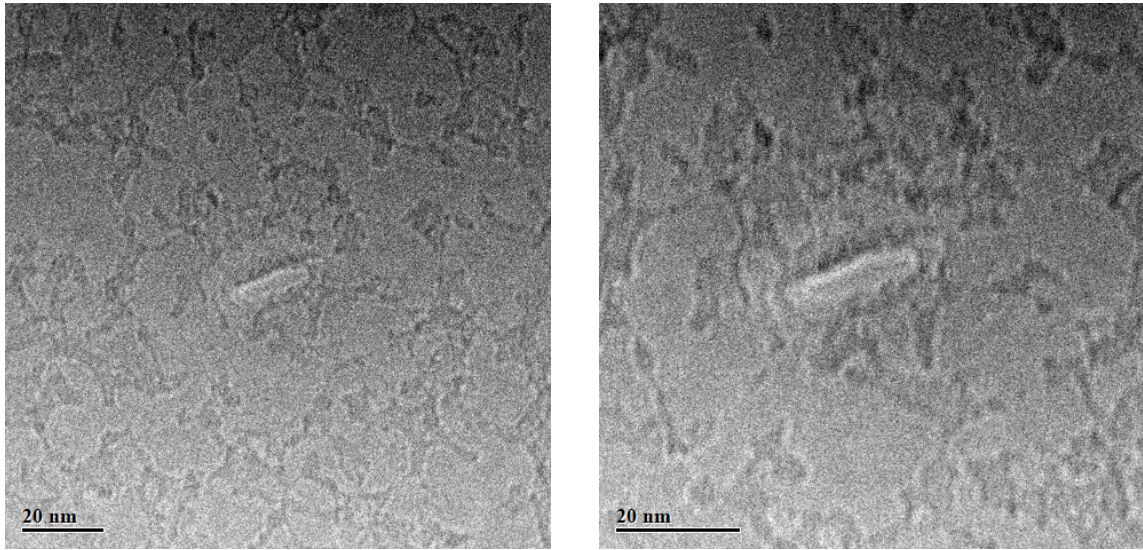


Figure 50: *Slit-like TEM-drilled pore. By slightly unfocusing the electron beam it was possible to obtain a slit-shaped pore whose dimensions are roughly 20 nm in length by 5 nm in width*

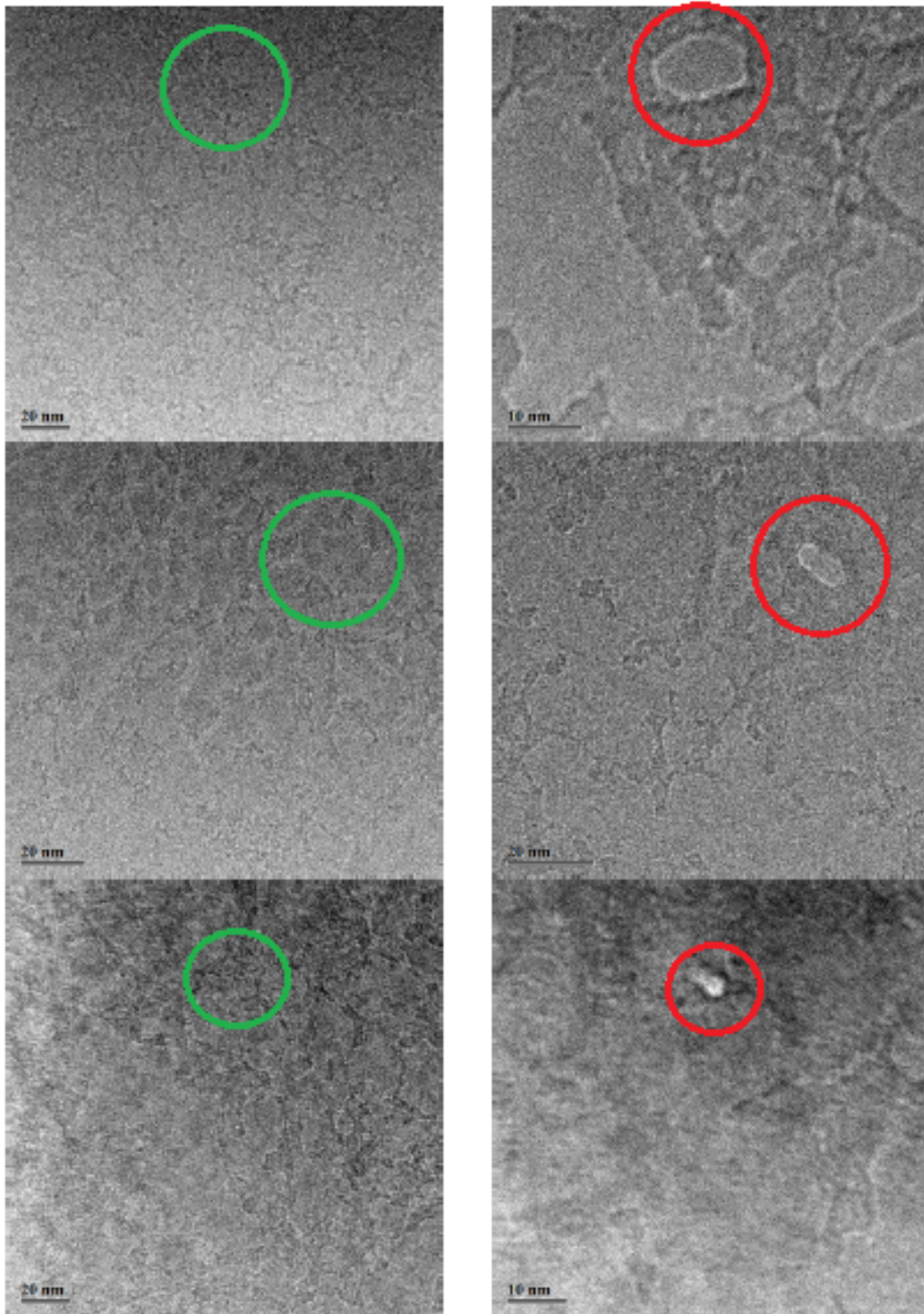


Figure 51: Collection of pore's images before (zone circled in **GREEN**) and after the TEM drilling in a Graphene's flake (zone circled in **RED**)

4.7 Plasma Etching

Once the EBL step is over the only thing left is to open the patterned nanochannels through the entire flake's thickness or, in case of a direct TEM drilling, if one wants to functionalize the nanochannel. To do so it was decided to exploit a VITAMINI plasma etching system.

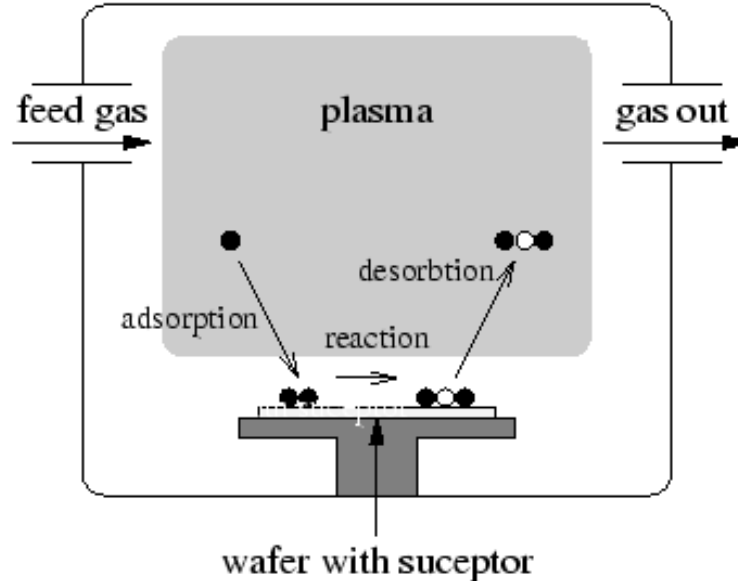


Figure 52: Sketch of a basic plasma-etching system

In general it is possible to decide if the etching process, to open the exposed resist, should be more physical (anisotropic, precise but paying with a higher inner roughness due to the direct damaging of the material) or chemical (isotropic, harder to control, but safer in term of roughness conservation). Practically the choice between one or the other can be done just adjusting some technical parameters such as the presence and the intensity of an accelerating voltage and the chemical species involved to create the plasma. In our case it was decided to use a purely chemical etching process. The gases's choice depends mainly on the type of functionalization that is required (positive or negative surface charge) and the used material (Graphene, MoS_2 , hBN). For instance, as presented in many papers^{65,66}, an oxygen plasma permits to obtain a negative surface charge while contemporary etching the nanochannel along the flake's thickness. What is happening is that after the PDMS stripping, post EBL, the sp^2

bonded carbon network of the flake is chemically disrupted by the O_2/Ar atoms in the plasma generating some terminations mainly composed by carbonyl groups that may be created also in form of polar covalent bonds, leaving the 4 nonbonding electrons in 2 lone pairs thus effectively generating a negative charged inner surface or edges as roughly sketched in **Fig.53**. That will bring to charge-specific effects, already presented in the *Physics* chapter.

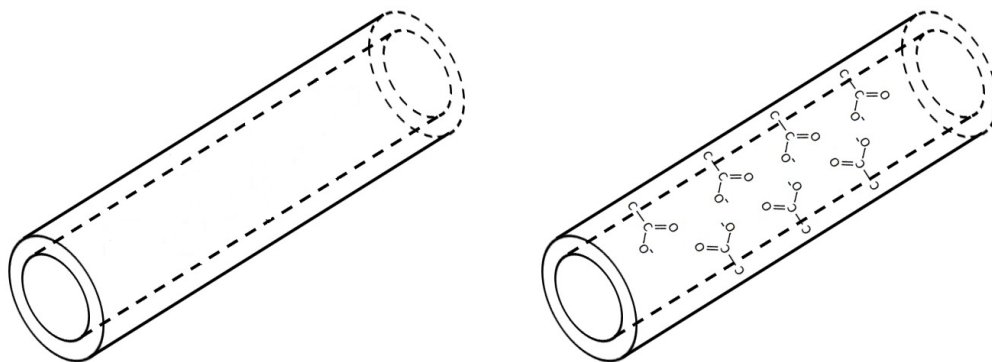


Figure 53: Sketch of a nanochannel before and after the plasma functionalization for Surface Charge tuning

Despite it could be considered a rather simple solution, the main drawbacks of this choice stand in a not so optimal and easy etching control of the conduit's geometry and in a slight enhanced surface roughness.

4.7.1 Etching analysis

For the issues presented above this step in particular deserved, and still deserves, many tryouts and checks. Every device etched or functionalized by this method was subjected to an attentive AFM or optical analysis prior and after each plasma cycle. It was already mentioned in the *physics* chapter how much important is the diameter of the channel if one wants to experience new nanofluidic effects such as, just to remind, the electrostatic screening operated by the surface charge. Since the etching stop is decided just by optical inspection, as presented in **Fig.54**

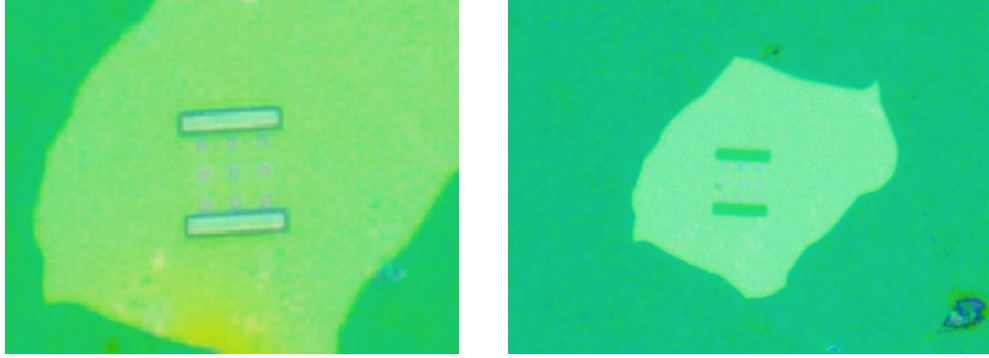


Figure 54: *The same sample before and after the etching step. The reduction in thickness determines a change in the color of the optically imaged sample. It is also possible to see that in the etched stripes the color is the same as the SiN membrane, sign of a complete etching of the flake.*

if there is not a clear idea on how much the etching rate is or the plasma parameters are not properly set, it could happen to over etch the flake risking to completely remove the device, to over-etch the channel increasing its diameter, the inner roughness of the channel, which brings to a flow resistance enhancement, or even introduce defects that mine and change the design of the device and thus misleading the comprehension of many results or specific behaviours.

After different AFM thickness inspection on many samples, prior and after each etching cycle, it was calculated the etching rate of the graphene and hBN when using our recipe.

Always thank to the AFM analysis, TEM imaging and some rational thinking we understood that, starting from the assumption that the etching process is purely chemical and thus isotropic, which means that the etching rate is the same along each direction of the space this brings to have a device conically-shaped, like in **Fig.55**, in which the first diameter on top, given by the EBL process and resist stripping will be transferred to the bottom of the flake practically unaltered, whilst the effective final top diameter will be as a first approximation equal to:

$$d_{top} = d_{bottom} + e_r * t_{etching} \quad (38)$$

where e_r is the specific etching rate and $t_{etching}$ is the etching time.

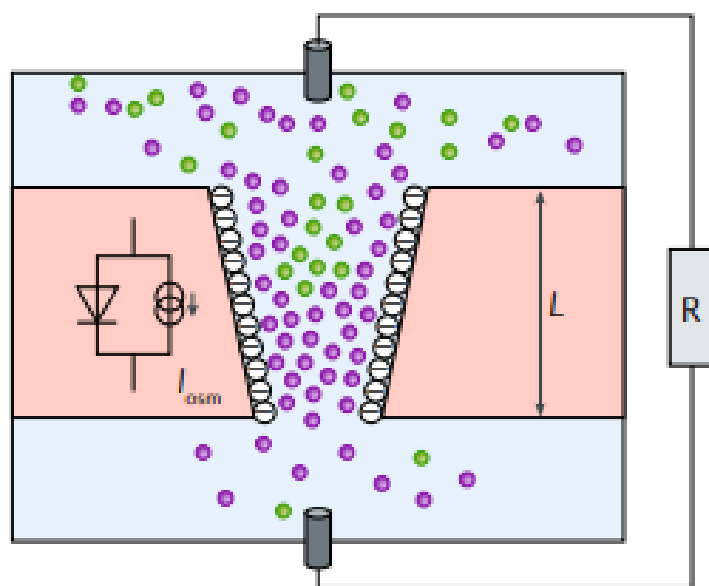


Figure 55: *Example of a Conical-shaped nanopore*

5 Measurements and Results

In this Chapter, are presented the measurements done on the fabricated devices and what it was obtained as confined ionic transport in graphite-based nanochannels. To perform such task, the device was inserted between two reservoirs containing aqueous salt solutions, mimicking a RED system. firstly is described the specific experimental setup used to measure ionic currents of the order of pico and nanoamperes, then the resulting findings are thus presented.

5.1 Experimental setup

The measurements were conducted on seven different devices, all produced with the same techniques explained in the previous chapter, but with different geometrical characteristics and materials. The measurement's protocol was developed in our group and it is presented in the following.⁶⁷ Since the topic deals with nanometric structures, the cleanliness during both the fabrication and then the final assembling of the entire measurement system is very important.

That is why, prior to any possible assembly, all the cell's components are precisely cleaned with an ultra-pure deionized water and then sonicated, in an ultrasonication system, in a "bath" lasting for half an hour at a controlled temperature of $T = 50^{\circ}\text{C}$. The silver chloride (Ag/AgCl) electrodes are mechanically scratched and regenerated using normal bleach. At this point the 1 cm x 1 cm chip with the fabricated nanofluidic device is placed between two PDMS gaskets that present access holes for the ionic solution. The resulting PDMS/Chip/PDMS stack is consequently inserted inside a custom-made fluidic cell whose two parts are sealed together by means of two tightly screwed rivets permitting to avoid any possible contamination or leakage. Now 4 access tubes and 2 Ag/AgCl electrodes are manually placed inside a clean DI bath to complete the total measurement cell. Finally as a preventive step useful to clean and wet the inner part of the cell, but also remove air bubbles in excess, both chambers are firstly degassed for a hour and half by means of a vacuum pump and after that directly flushed with 50 ml of ethanol, then with a 50 ml deionized water/ethanol mix and finally with 100 ml of deionized water. Avoid bubbles is funda-

mental to conduct this type of measurements since, if present, they do not permit the generation of a current acting as a huge resistance. Once all of the critical previous steps are completed the device is thus ready for measurement upon accurately and slowly flushing the chosen salt solutions in the reservoirs, of course paying attention to not inject additional micro-bubbles.

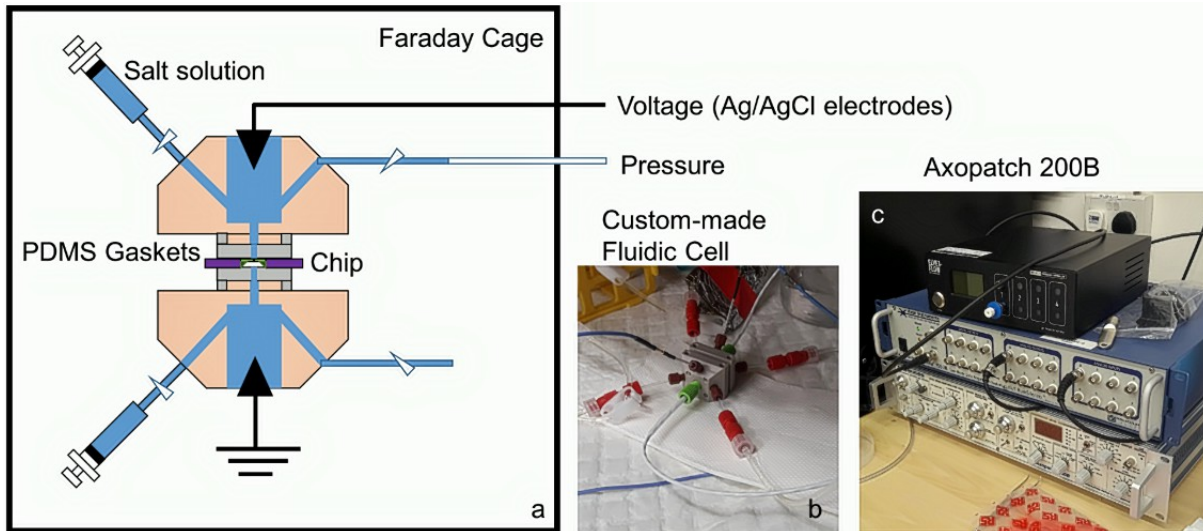


Figure 56: (a) Sketch of the completed fluidic cell (b) photo of the fluidic cell during fluidic measurements (c) 2-channel fully configurable oscilloscope (Time span, voltage applied, waveform), a pressure controller and a external-noise suppression system

Since the measuring system deals with current intensities in a range comprised within few picoamperes to nanoamperes an extremely sensitive hardware and setup is needed to correctly perform the measurements with the highest resolution possible. Such goal is properly achieved using an **electrophysiology** setup, an apparatus created to measure biological membrane potentials using the **patch-clamp** technique.⁶⁸

5.1.1 Characterization routine

Once everything is correctly assembled the measurement can be performed. The characterization routine is pretty simple to describe. It collects a total of 5 main aspects to analyze, each one extracted by a precise set of specific measurements as presented in table of **Fig.57**

	Set of measurements
<i>I/V characteristic</i>	<ul style="list-style-type: none"> ➤ <i>Electrophoretic transport in equimolar medium</i> ➤ <i>Electro-osmotic flow</i>
<i>Ionic conductance</i>	<ul style="list-style-type: none"> ➤ <i>Electrophoretic transport in equimolar medium</i>
<i>Streaming current</i>	<ul style="list-style-type: none"> ➤ <i>Pressure-driven ionic transport</i>
<i>Osmotic power generation</i>	<ul style="list-style-type: none"> ➤ <i>Electro-osmotic flow</i>
<i>Power generation efficiency</i>	<ul style="list-style-type: none"> ➤ <i>Electrophoretic transport in equimolar medium</i>

Figure 57: Table collecting the main characteristics analyzed in a fabricated device (left column) and the respectively experiments useful to extrapolate the values or the general behaviour (right column)

5.2 Electrophoretic transport in equimolar medium

This test is fundamental to obtain the first two figures of merit of our device: The *I-V characteristic* and consequently the system *Conductance*, thus permitting to extract the overall behaviour of the system under-test when an electrical stimulus is applied also highlighting peculiar ion-nanopore interactions. It is entirely based on the electrophoretic transport and separation of charged species like cations and anions, through the nanofluidic membrane, only when applying a voltage drop between the two electrodes. To completely ensure a drift-based motion, the electrolyte concentration is either kept in an equimolar or in a soft salt concentration gradient condition. A specific description of the measuring protocol is given below.

Starting with DI in both reservoirs, to set the reference point, as previously introduced a voltage sweep is applied to the cell electrodes in a range within -200mV and +200mV, each voltage pulse is formed by a transition time of 10 ms and a static time that lasts 2 seconds to ensure the achievement of an equilibrium condition. The measure is repeated and saved 3 times. The same procedure is maintained for the consecutive measurements, with the only difference that subsequently a specific salt solution will be injected in

the two fluidic chambers of the cell substituting the DI.

Starting with the lower concentration of 0.1 mM it is possible to pass to the successive one just generating salt concentration gradients whose ratio is not higher than $1 \leq \frac{c_{high}}{c_{low}} \leq 3$. Doing this way the transition from a specific concentration to the other, up to the final 3 M concentration, can be done smoothly and moreover having the possibility to substitute the concentration difference with an averaged value, thus increasing the number of available experimental points.

5.2.1 I/V Characteristics

To obtain the I/V curves, two types of concentration tests were conducted, which are described in chapters 5.2 and 5.3. From this type of information it is possible to extract many other parameters, which will be described in the following chapter, useful for a complete behavioural description of the device under scrutiny.

To do so, as already introduced in chapter 5.1, we used as the main source of excitation an Axon Axopatch. The output pin of the signal generator was directly connected to the Ag/AgCl electrode placed in the backside of the membrane while the electrode placed in the top part, toward the graphitic flake, was instead connected to ground.

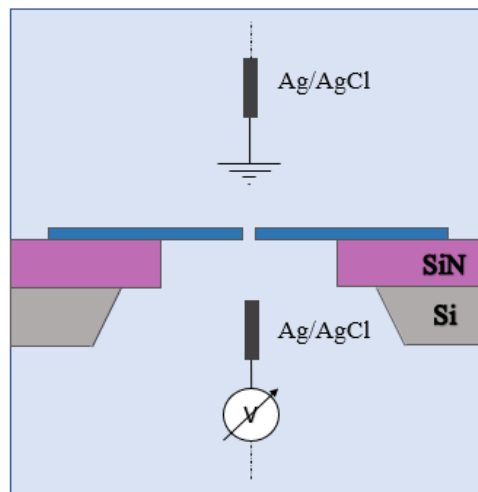


Figure 58: Simple representation of the electrodes connection

In particular it was applied 21 times a two-second long constant voltage ΔV in form of steps of 20 mV per measurement, starting from an initial voltage drop of -200 mV up to +200 mV. Each time the signal was applied the current vs voltage curve (I-V) is obtained and plotted by considering the average of the resulting current trace, furthermore excluding the first 0.1 s to bar any capacitive response of the system to voltage changes. The low-pass filter frequency was set to 10-100 kHz in all the experiments, using a sampling rate of 20 kHz. This specific filtering at relatively high frequencies was useful to obtain information by the spectral analysis. As a matter of fact slow time responses and high noise levels can be generated by capacitive effects linked to the bubbles that are partially clogging the channel.^{69,70} In **Fig.59** and **Fig.60** are showed some very interesting results:

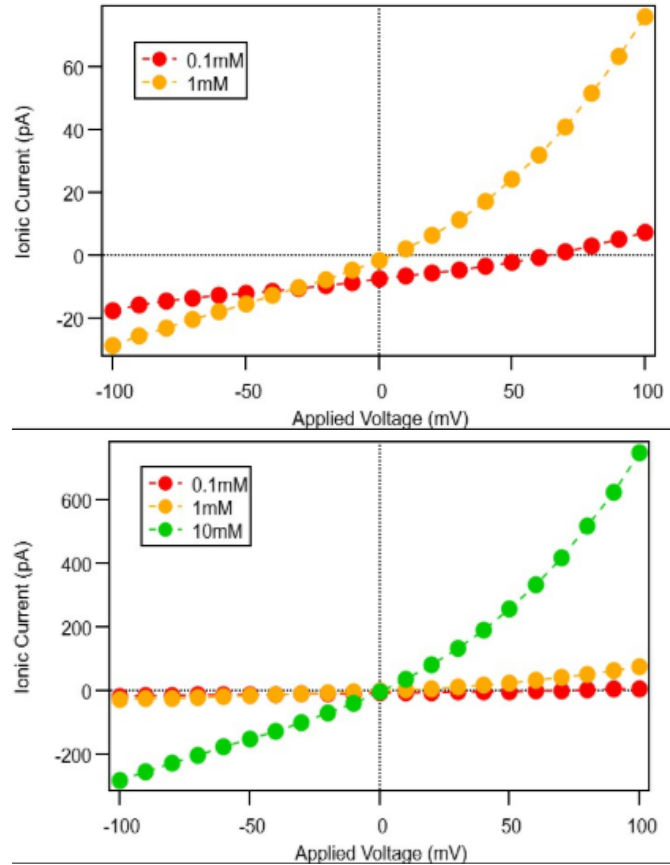


Figure 59: Example of I/V curves for low and medium concentrated solution. 0.1mM (red), 1mM (yellow), 10mM (green). The device under test dimensions are: $D = 20$ nm, $L = 60$ nm, number of pores = 9

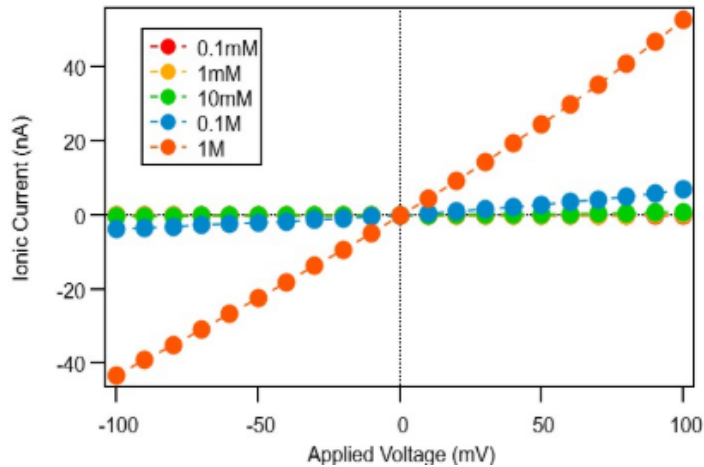


Figure 60: I/V curve for a high concentrated solution. 1M (orange). The device under test dimensions are: $D = 20$ nm, $L = 60$ nm, number of pores = 9

The first thing that immediately appears pretty obvious is a behaviour similar to a well-known device of the semiconductor field, the Diode-like behaviour. By analyzing the images is possible to clearly see that similarly to semiconducting systems, a nanofluidic diode is identified by a remarked nonlinear response to the applied electric signal (ΔV). The ionic current characteristic reflects the asymmetry of the system, in particular showing high conductance values for all the positive voltage drop, with a current that increases exponentially, while a very low conductance for the opposite voltage sign. The ionic transport is thus said to be rectified and ions "prefers", or better it is less expensive in term of energy, to move throughout the entire channel's length along one preferential direction.²⁴ Must be underlined that the causes or the ways to achieve such peculiar behaviour are different. In literature the reported ones mainly are: the geometrical asymmetry of the device, as reported by Siwy et al.⁴⁸, or by an asymmetric surface charge distribution, as reported years later by Karnik et al.⁷¹. In our case the underlying cause lies, as in the former case, in the asymmetrical conical shape of the conduit coupled with the electrostatic exclusion process typical of a Debye length (λ_D) overlap. This specific geometry appears to determine a preferential way of drifting that is much more facilitated towards the direction in which the diameter of the channel keeps increasing, so from the ending tip up to the top larger base. It is also possible to confirm that is not due to an uneven surface charge distribution

because, considering that the oxygen plasma etching, used to open and shape the channel, acts isotropically over the whole conduit's extension, at the best of my knowledge there is any other cause that would determine an irregular surface charge. Instead the typical current response asymmetry, which would have been determined by a varying surface charge, in this case is simply given by the fact, as already introduced, that the λ_D can effectively overlap only at the tip side. Specifically for this device the **Tip** diameter (D_{tip}) is equal to 20nm, while the typical λ_D extension at different electrolyte concentration is collected in **Tab.2**.

$[c_s]$	10^{-4} M	10^{-3} M	10^{-2} M	10^{-1} M	1 M
λ_D	60 nm	30 nm	10 nm	3 nm	1 nm

Table 2: Table containing the approximated values of the Debye screening length (λ_D) for different salt concentration values. The 10 nm screening length, comparable to the device radius, is enough to permit a selective passage of ions at the Tip side.

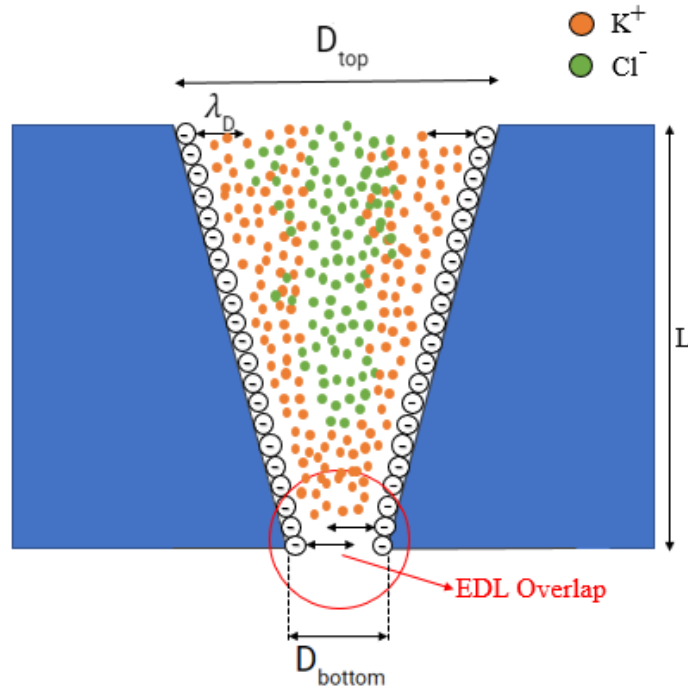


Figure 61: Sketch of a conical nanochannel. It is common to refer at the larger diameter at **Base** while at the smaller one, where the Debye layer overlaps, as **Tip**.

From **Fig.59** and **Fig.60** is also possible to notice that the rectification

effect appears to be higher at a medium salt concentration. Is that so because, comparing the Debye length extension with the nanochannel's smaller diameter, is still possible to have an effective electrostatic screening while ensuring a higher number of a certain specie of ions, due to the higher salt concentration. At very low molarities an overlap of the electrical double-layer is still present, but in general the overall number of ions useful to generate a net current is reduced, that is why the current reach a very low value. On the contrary when the salt concentration becomes higher, the surface charge screening length is not extended enough to present any selective passage, and even though there is still a geometrical preferential way for the current flow, the overall current cannot be determined just by a charge-specific surface transport. Consequently any rectification effect is thus drastically reduced or even lost. From the above analysis it is thus possible to assert that, as presented in **3.3.1** (Donnan theory), using such type of structure the ionic concentrations inside the channel are mainly determined by the surface charge density of the inner walls, the electroneutrality requirement and in this case the peculiar geometry of the system, but only weakly by the external applied voltage.

5.2.2 Diode-based effects on power generation

But why having such type of nonlinear ionic transport is fundamental or of any practical value for Blue energy power generation? Generally speaking the maximum extractable power P_{Max} of such systems strictly depends on the intrinsic characteristic of the membrane. From **Eq.36** that can be restated as:

$$P_{Max} = \frac{R_M \times I_{Osm}^2}{4} \quad (39)$$

it appears clear that the membrane resistance, R_M and the generated osmotic current, I_{Osm} , play a fundamental role in the overall power generation process under an applied salinity gradient. Nevertheless if any electrical load, R_L is associated to the system, the above discussed power could not be collected and eventually used. In this picture the equivalent electrical circuit, represented in **Fig.62**, associated to the system presents

two possible working "regimes".

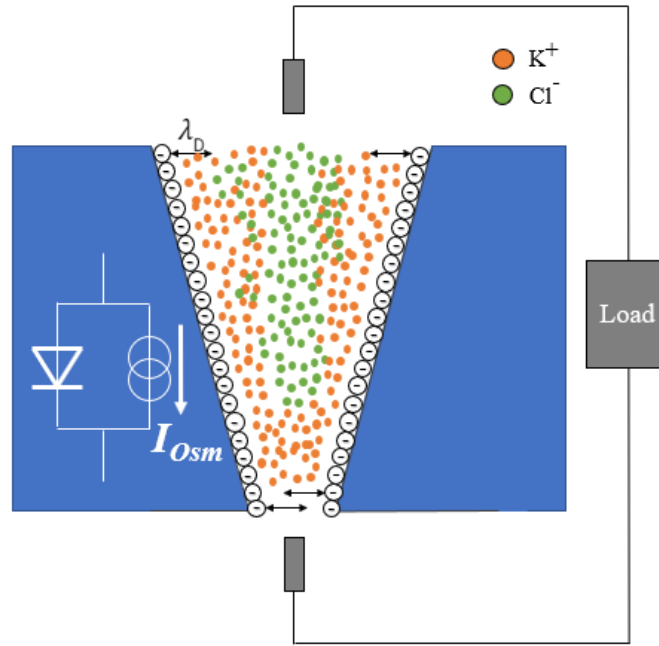


Figure 62: *Equivalent electrical circuit for an asymmetric osmotic power generator. The membrane generates an osmotic current that goes in parallel to a diode. The attached load acts as a power extractor*

The first one is associated to a low load resistance, in which case the greatest part of the generated ion current flows and dissipates directly on the load. Consequently the harvested power will scale as:

$$P_{Osm} = R_L \times I_{Osm}^2 \quad (40)$$

The second regime is instead associated to a high R_L and the osmotic power will reduce to:

$$P_{Osm} = \frac{R_M^2 \times I_{Osm}^2}{R_L} \quad (41)$$

In this opposite situation the I_{Osm} will almost completely circulates in a sort of loop within the membrane, with a maximum extractable power achievable only in the case that $R_M = R_L$. This means that for high load resistance values, a large part of the osmotic power generated from the system is directly lost due to the membrane itself, particularly converting

the energy of mixing into Joule heating. Just presenting this simple electrical representation immediately appears clear the importance to have a system that under controlled circumstances, for instance in the reversed bias regime of the diode, can presents very high levels of membrane resistance. This would block the back current in the nanochannel avoiding the above cited Joule dissipation, thus reaching the maximum harvestable power working as an ideal current generator.^{52,24}

Despite the fact that this digression did not considered a real world application, in fact having a membrane completely and constantly working in the "blocking" regime is only ideal speculation, describing such analogy and implication paints perfectly how uncommon behaviours of complex nanofluidic systems can be exploited to overcome the osmotic power generation limits, being able to boost it at its practical maximum.²⁴

5.2.3 Ionic conductance

From the previous I-V curve raw data, thanks to a python code, it is possible to extract the device's conductance. One example among many other results is presented in **Fig.63**:

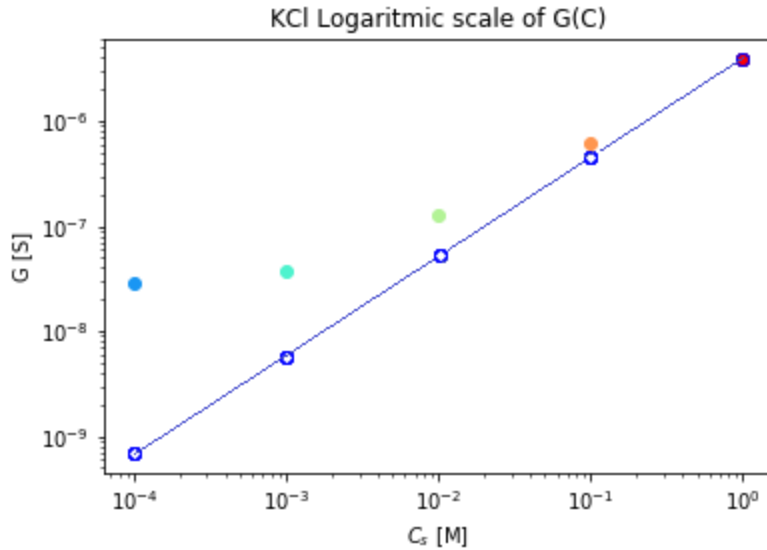


Figure 63: G [S] vs C [M] curves for a hBN nanopore. $D = 55\text{nm}$, $L = 10\text{ nm}$, $\text{pH} = 10.6$, number of pores = 9. The blue line represents the classical bulk-driven conductance without considering any surface conductance effect (**Eq.43**). The colored dot instead represents the experimental conductance extracted from the device's analysis.

Analyzing the conductance behaviour is possible to obtain different information about the result of the nanofabrication process or extract important parameters, for instance one can determine if the channel's diameter is of the same width as the expected one from the EBL and etching processes, or determine the overall inner surface charge. Even though this could appear trivial, in reality when talking about such nanofluidic systems everything becomes much more complex and one must account for many others side-effects, such as the **Access resistance** effect and the **Surface conductance** process. Anticipating the much more thorough explanation in **5.2.4**, at the beginning it was thought that **Eq.43** perfectly described the nanopore's electrical behaviour.

$$R_p = \frac{4L}{\pi D^2 \kappa_B} \quad (42)$$

Nevertheless in many other papers analysing different devices such as BN nanotubes or other solid-state nanopores^{21,72,73} and also in our device, refer to **Fig.63**, if one looks at the experimental electrical behaviour, it is possible to assert that the above cited equation is not working at all. Yes, it represents correctly the linear behaviour of the conductance with respect the increasing solution's concentration C , mainly due to the bulk conductivity, but misses completely the conductance plateau at low molarities and furthermore gives back values at least one order of magnitude lower than the experimental results.

At this point one may think that it is not a problem of the physical model, but rather something that is not working in the device or in the measurement system, nevertheless, as reported in literature⁷⁴, the saturation of the conductance correctly shows the surface charge effect. Having a constant conductance means that the concentration of the ion in the conduit is no more determined by the bulk solution conductivity, but instead it is maintained constant by the surface charge selectivity that permits only the passage of counterions through the channel, which amount is fixed. It is also interesting to anticipate that the intrinsic geometrical nature of the nanopore as "0D" object will have a huge impact in the behaviour of the system

How to properly account for this effect and the peculiar geometry of the nanopore over the overall conductance of the device is deeply explained in

the following chapter.

5.2.4 Access Resistance and Surface Conductance

In general the easiest way to electrically model a nanopore is to describe it as a cylindrical hole drilled through an insulating membrane, which divides two reservoirs filled with a uniform conducting medium (the electrolyte). The main parameters to consider are the flake's thickness, which determines the membrane length (L), the nanopore diameter (D), and the bulk electrical conductivity of the electrolyte (κ_B).

In the assumption of uniform electric conductivity that is valid only if these two experimental condition are respected:

- The **Debye length** is much smaller than the pore diameter, so that the cations and anions distribution inside the pore do not need to be correct for the selective screening
- The importance of surface conductance relatively to the bulk conductance, which is measured by the Dukhin number ($Du = \frac{\kappa_S}{\kappa_B}$), is small ($Du \ll 1$)

the nanopore resistance could be expressed as:

$$R_p = \frac{4L}{\pi D^2 \kappa_B} \quad (43)$$

It comes by itself that if $L \rightarrow 0$ then also $R \rightarrow 0$ that is in total contradiction with the reality, in which it was seen that experimentally reducing the length to the atomically-thick level the resistance saturates at a constant value called "Access Resistance" (R_{acc}). The equation for this specific resistance was firstly proposed from Hille⁷⁵, starting assuming a radially convergent electric field and successively refined by Hall⁷⁶, leading to the final equation:

$$R_{acc} = \frac{1}{D \kappa_B} \quad (44)$$

From this quick analysis we understand that all the descriptions for the entrance effects relies on the assumption that the pore can be considered

as resistances of different nature in series^{76,75}, with the resistance inside the pore R_p directly extended by the inlet and outlet access resistances $\frac{R_{acc}}{2} = R_{acc,in} = R_{acc,out}$ on each side of the pore, thus presenting an overall resistance of:

$$R = R_p + R_{acc} = \frac{4L}{\pi D^2 \kappa_B} + \frac{1}{D \kappa_B} \quad (45)$$

or equivalently the overall conductance:

$$G = (G_p^{-1} + G_{acc}^{-1})^{-1} \quad (46)$$

So what was missing in all the previous models, the nanochannel one or the one proposed by Hille and Hall, is that the geometrical nature of the nanopore, in which the both the length (L) of the conduit and the Debye layer (λ_D) is comparable to the nanopore's diameter (D), does not permit to exclude the surface charge perturbation on the electric field deep into the bulk of the reservoirs, as presented in **Fig.64** ($Du \gg 1$).

The 3D entrance effects directly in the area outside the nanopore's rim that couples directly to the surface-based conduction inside the nanopore. This unpredicted coupling, which occurs in order to respect the charge conservation rule at the pore entrance, broadly perturbs the external electric current streamlines, consequently creating new paths at high conductance even when dealing with low salt concentrations.

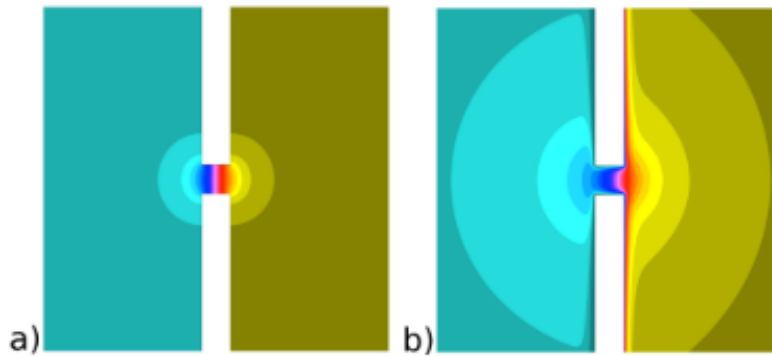


Figure 64: COMSOL 2D representation of the potential distribution around a nanopore (a) not considering any surface charge and (b) considering non-null surface charge distribution inside the nanopore.⁷⁴

Typically this perturbation extends for a length which is equal to the

Dukhin length L_{Du} already introduced in **3.1.2**. Surface transport of ions impose that ions need to be present within the diffuse interface range to respect the charge conservation rule, as a physical result the electric streamlines are totally bent against the pore outer and inner surface.⁷⁷ The access conductance outside the pore depends thus intimately on the surface conductance inside the pore:

$$G_{out} = \alpha\kappa_b D + \beta\kappa_s \quad (47)$$

where α and β are two experimental geometrical prefactors, while the two κ represent respectively the bulk and the surface conductivity, D is of course the pore's diameter. After some math then is possible to retrieve the final total pore conductance, which can be described as:

$$G = \kappa_b \left[\frac{4L}{\pi D^2} \frac{1}{1 + 4\frac{l_{Du}}{D}} + \frac{2}{\alpha D} \right]^{-1} \quad (48)$$

Starting from this equation is interesting to analyze the condition of a large Dukhin length ($l_{Du} \gg D$) that, just to recall, can be expressed as $l_{Du} = |\Sigma|/2c_s$, with $|\Sigma|$ being of course the surface charge and c_s the solution bulk conductivity. It is clear that such condition could be obtained in the case of a surface charge higher then mC/m^2 , which is specifically the case our device whose Σ was enhanced both by a plasma etching process and imposing a pH of 10.6 to the solution adding a basic compound to the electrolyte. In this condition **Eq.48** can be expressed as:

$$G(l_{Du} \rightarrow \infty) = \kappa_s \left[\frac{4L}{\pi D^2} + \frac{2}{\beta} \right]^{-1} \quad (49)$$

predicting a saturation of the conductance at small salt concentration values. It is possible to explain this effect from the fact that this type of coupled conduction enhancement can be interpreted in terms of an increased *apparent* pore size (D_{app}). The amount of the increase is directly proportional to the entity of the surface conduction as:

$$D_{app} = D + \frac{\beta}{\alpha} l_{Du} \quad (50)$$

Moreover **Eq.48** enlighten the dependency of the overall conductance only on the geometrical aspect ratio L/D of the specific pore, but not explicitly only on its diameter D . This suggest that, with a proper nanofabrication control and design, small pores can conduct as efficiently as larger pores or highly-charged nanotubes.⁷⁴

From equation **Eq.48**, thanks to a custom-made python code, it was also possible to extract and measure an important parameter of the nanopore, the surface charge (Σ).

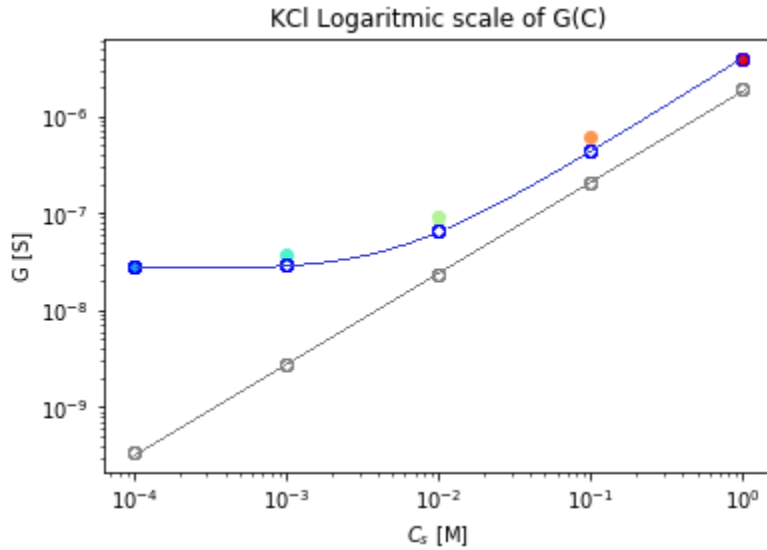


Figure 65: G vs C curves for a hBN nanopore. $D = 55$ nm, $L = 10$ nm, $pH = 10.6$. The grey line represents the classical bulk-driven conductance without considering any surface conductance effect, the colored dots the experimental conductance, while the blue represents the theoretical conductance from **Eq.48**. It can be seen that a nearly perfect fitting is obtained, the correspondent value for Σ is equal to $65 mC/m^2$

For the graphitic flakes were estimated values comprised within $0.5 mC/m^2$ and $1.5 mC/m^2$. This could be explained by the fact that for some devices the TEM irradiation, used to pierce the membrane, could have generated inner surface defects.⁷⁸ In the case of those nanopores obtained instead through a plasma-oxygen etching process, the inner etched surface can be terminated with a variety of charged chemical groups such as hydroxyl, ketones and ethers.⁷⁹ for hBN nanopores instead the measured Σ was in a range comprised $0.5 - 65 mC/m^2$ according to the imposed pH.

5.3 Electro-Osmotic transport

In the previous chapters it was described only a condition in which the ions inside the channel were directly driven by voltage gradients, by means of the electrophoresis process or voltage-induced “drift”. In the following chapters instead it will be presented an additional way to drive the ions, we are talking about the diffusive motion that is obtained by imposing a salt concentration gradient. The ions whose are much more concentrated in the high salt concentration (c_h) reservoir will naturally diffuse toward the reservoir with the lower salt concentration (c_l). For this reason the whole process is commonly know as *Ionic diffusion*.

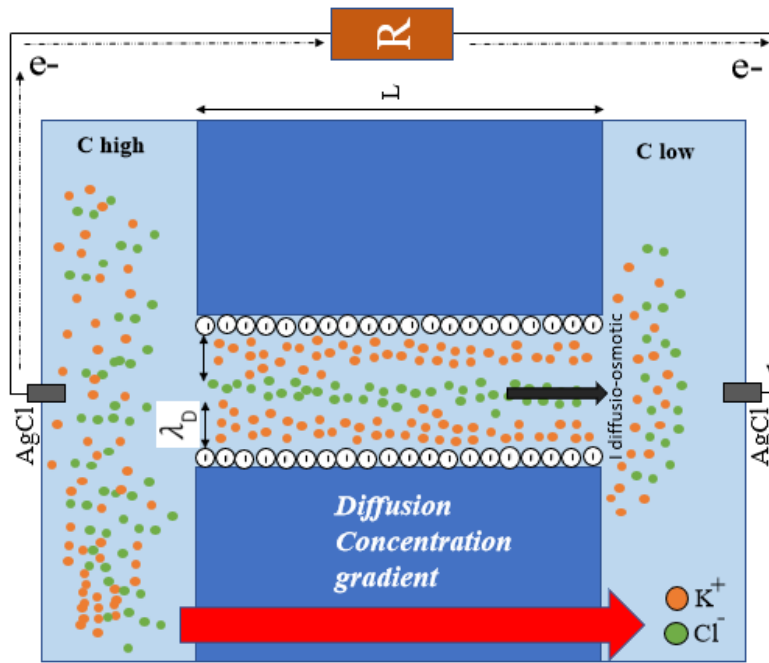


Figure 66: Example of a solid state nanopore under salt concentration gradient condition.

In **Fig.67** is presented a typical drift-diffusion IV curve when passing from a symmetric concentration condition (line passing from the origin) to an asymmetric one, which is practically imposed by filling the inlet (top side) and the outlet (bottom side) with the same solution but, as described, at different concentrations. This experiment is fundamental to extract the two main figure of merit specifically related to my research goal: The generated **electrical power** and the **power conversion efficiency**.

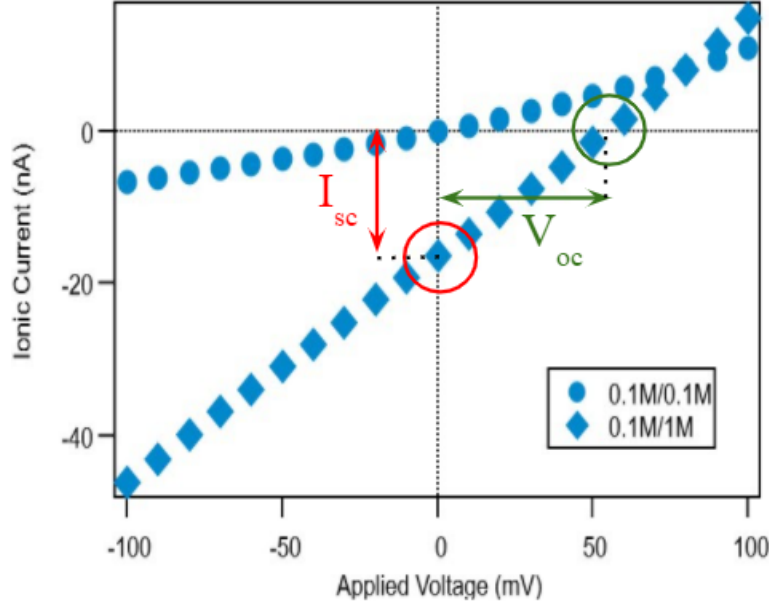


Figure 67: Drift-diffusion I-V curve for a KCl solution in a device composed by a matrix of 9 graphitic nanopores whose geometrical characteristics are: $L = 60$ nm, $D_{eff} = 20$ nm

Specifically analysing the I-V curve it is possible to obtain two fundamental parameters: the open-circuit voltage V_{oc} and the *short-circuit current* I_{sc} . They can be directly extracted from the graph by looking at the interception with the x and the y axis respectively, as reported in **Fig.67**.

It was already briefly introduced in **3.3.3** and **3.3.4** the importance of the permselectivity (S) parameter in the picture of the osmotic power generation. It is now the moment to recover those theoretical basic insights and properly apply them to our case. The coupled drift-diffusion process of current generation can be described by the Nernst-Planck (NP) equation, as expressed in **Eq.51**, the total current density generated inside the layered nanopore is the added effect of two main contributions, the voltage and concentration difference:

$$J_{\pm} = -\mu_{\pm}(RT\nabla c_{\pm} \pm Fc_{\pm}\nabla V) \quad (51)$$

Contrary to **Eq.33** this can be applied only to univalent electrolytes. Another change stands in the choice of substituting the diffusion constant D_i with $\mu \times k_B T$ by exploiting the Einstein's relation. What it is not

changed instead is the intrinsic physical meaning of the quantities that comes into play. The first term is related again to a diffusion current while the second one to a drift current. Nevertheless before applying this framework to the experimental I-V curves, it is needed to correct some data. In fact to truly obtain the selective ion transport signature, or the *Osmotic Potential*, what is missing is the compensation of the contribution given by the presence of the electrode through the red-ox potential. Starting from the fact that the potential of the Ag/AgCl electrode directly depends on the Chlorine anion concentration $[Cl^-]$, it can be expressed as:

$$V_{Ag/AgCl} = V_{std} - \frac{RT}{F} \ln(\gamma_{Cl^-} [Cl^-]) \quad (52)$$

where V_{std} is the electrode standard potential, measured with respect the standard H_2 electrode and γ_{Cl^-} the Cl activity coefficient.⁸⁰ If we consider that our system is composed by two Ag/AgCl electrodes usually immersed in KCl solutions with different concentrations it possible to express the electrodes potential difference with:

$$V_{el} = V_{Ag/AgCl}(c_i) - V_{Ag/AgCl}(c_o) = \frac{RT}{F} \ln \left(\frac{\gamma_o c_o}{\gamma_i c_i} \right) \quad (53)$$

At this point subtracting this value to the open-circuit voltage is thus possible to simply obtain the device's osmotic potential:

$$V_{Osm} = V_{oc} - V_{el} \quad (54)$$

Through the ion selection process that determines the effective osmotic potential, the nanopore transduces the Gibbs free energy of mixing into an *Osmotic Current* ($I_{Osm} = G \times V_{Osm}$). The result of this process, as already discussed in **3.3.3** or **2.2.1**, can be harvested by an electrical load.

In **Fig.68** are showed the measured osmotic potential and current in a Graphite-based nanopore when imposing different concentration ratios. In particular starting from an equimolar concentration of 0.1mM, c_i is varied from 0.1mM up to 1M while keeping c_o constant to 0.1mM. Once this first set of measurements is over, the top side concentration (i.e. c_i) is kept constant while the bottom concentration c_o is gradually increased up to reach again an equimolar condition at 1M/1M. Of course this creates a double

pair of the same c_i/c_o ratio, but each one related to the high salt concentration region or the low salt concentration one. To better understand it just imagine that 1M/10mM or 10mM/0.1mM gradients presents the same concentration ratio, but in two completely opposite ionic concentration regions.

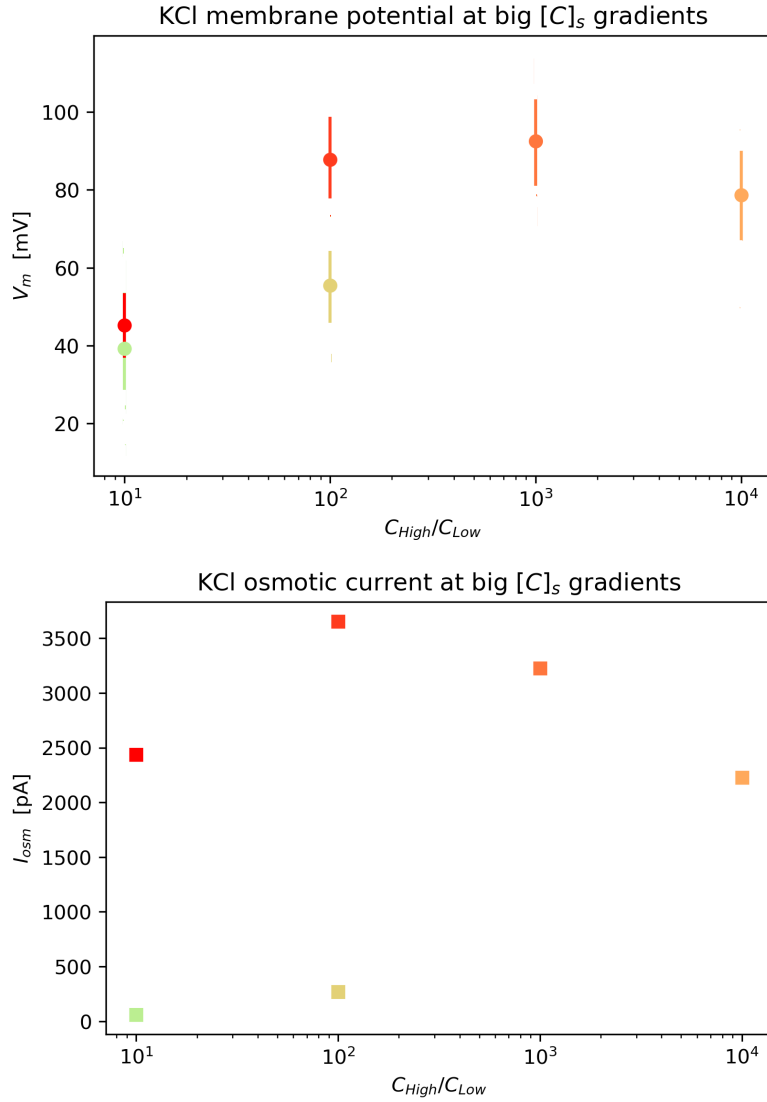


Figure 68: V_{Osm} and I_{Osm} for a Graphite-based TEM-drilled device as a function of the concentration ratio. $D = 10\text{nm}$, $L = 7\text{nm}$. The Red-gradient data points refers to the high concentration region ($c_i = 1\text{M}$ and c_o gradually increased). The Green-gradient data points refers to the low concentration region ($c_o = 0.1\text{mM}$ and c_i gradually increased)

Analyzing the images we immediately notice a maximum in the os-

otic potential, $V_{Osm} = 92mV$, imposing a concentration gradient at 1000-fold (1M/1mM). The osmotic current instead presents its peak value, $I_{Osm} = 3650pA$, for a concentration gradient at 100-fold (1M/10mM). What is interesting to analyse, in my opinion, is the huge discrepancy of potential and current values at the same salt concentration ratio.

For the osmotic current a first fast explanation could be that, if we consider inside the pore an average concentration within the two solution in the reservoirs, the overall number of available ions in the channel, thus the bulk conductivity, is drastically reduced. Although this explains the current difference, there is no connection with the osmotic potential difference. It is thus needed to search for another possible mechanism that affects both the two parameters. The latter indeed exists and will be presented after in the chapter.

Starting from the osmotic potential analysis, theoretically speaking, if one considers the same electrolyte, formed by univalent ion species with diffusion constant D_i , injected in the two reservoir with a difference in salt concentration, owing to a net flux of ion as already expressed in **Eq.51**. At this point the models used to describe the resulting osmotic electrostatic potential difference are several⁸¹, each one of them relying on different assumptions in relation to the ion distribution and local electric field profiles inside the channel. The Goldman–Hodgkin–Katz (GHK) model⁸² is the best suited for short nanopores and assumes a constant electric field along the channel, so that if one requires the system electroneutrality, after some math, finds the resulting osmotic electrostatic potential difference expressed as:

$$V_{Osm} = \frac{k_B T}{e} \ln \left(\frac{P_+ c_h - P_- c_l}{P_+ c_l + P_- c_h} \right) \quad (55)$$

where $P_{\pm} \sim D_{\pm}/L$ is the permeability of the ion species. This result, having in mind what was explained earlier, clarifies that the osmotic potential value does not only depend on the salt concentration ratio imposed in the two reservoirs, but also on the permeability of the single ion species thus in the specific charge-wall interaction dictated by the nanopore permselectivity. When working in the low concentration regime some subtle mechanism related to the interplay within charges and the nanopore walls undermines the ion motion through the membrane. The reasons

could be different, but what I found in literature to explain realistically those results is, for the higher values the combination of:

- **Surface conductance** - which was abundantly explained in **5.2.4**
- **Debye layer overlap** - which, as presented in many previous chapter, determines a selective passage of ions.

whilst for the lower values the so called:

- **Debye layer (λ_D) overspill**

Before explaining the effects of those mechanisms on the experimental results one needs to analyse the geometrical properties of this device to have a clear picture of the experimental conditions. The length ($L = 7nm$), determined by the flake thickness, is slightly smaller than the nanopore diameter ($D = 10nm$), which in this case is comparable to or even smaller than most of the electrostatic screening length (λ_D), whose typical approximated values are collected in **Tab.2**.

At this point is clear, also from what it was stated previously, that the device can operate at two different salt concentration condition even if characterized by the same driving process (osmotic flow) with the same concentration ratio ($\frac{c_h}{c_l} = 10^2$). In those two pictures happens that:

- If we consider the high-medium salt concentration gradient with $c_h = 1M$ and $c_l = 10mM$ the resulting relation within L , D and λ_D is: $L \sim D \sim \lambda_D$. The Debye layer overlaps in the low concentration side, assuring the selective passage of ions and contemporary the surface charge combined with the slightly bigger diameter is enough to generate surface conduction and thus a higher net ionic current (as explained in **5.2.4**). Furthermore due to the $c_h = 1M$ the availability of ions is at least 100 to 1000 times higher than in the lower concentration regime, thus highly sustaining the surface current. The result is an osmotic current of $I_{Osm} = 3650pA$ and a higher V_{Osm}
- If instead we consider the medium-low salt concentration gradient with $c_h = 10mM$ and $c_l = 0.1mM$ the resulting relation within

L , D and λ_D becomes: $L < D \ll \lambda_D$. In this specific case the Debye layer extension, especially in the c_l reservoir, greatly exceed the nanopore diameter. In **Fig.69** it is presented a sketch that describes this situation.⁸³

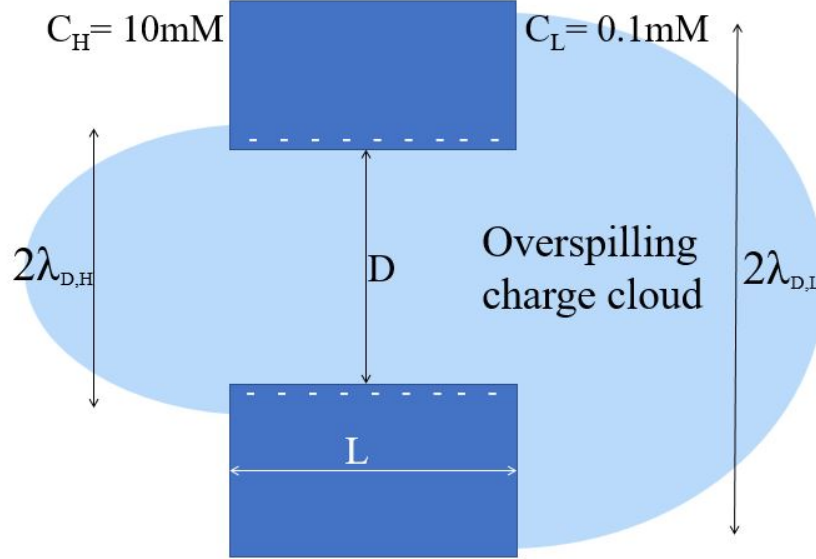


Figure 69: Sketch representing the overspilling of the counterion cloud due to an excessive extension of the Debye layer with respect the nanopore diameter.

When $\lambda_d \sim D$ The Debye layer at the walls as we said overlaps and part of the resulting counterion aggregate “spills” out at the end of the pore’s rim. The spilled charge could be considered negligible compared to the total charge inside the pore when $L \gg D$, but this cannot be considered the case ($L \sim D$). The applied voltage drops mainly across the nanopore extension, thus not permitting to the “spilled” charges, which are lost at the entrance and the end of the nanopore edges, to actively contribute at the ionic current stream, mining the overall power generation efficiency and intensity.⁸³

5.3.1 Osmotic power generation and conversion efficiency

Once the osmotic current and the osmotic potential are defined, the step to extract the nanopore-generated power density is straightforward. The

osmotic power P_{Osm} assumes the well-know value of:

$$P_{Osm} = V_{Osm} \times I_{Osm} \quad (56)$$

In **5.2.2** it was seen that the maximum osmotic power could be expressed as in **Eq.39**. Considering the classical ohmic law ($V = I \times R$) and dividing the value for the nanopore cross-section A_{pore} and the total number of channels composing the membrane N_{pore} , one obtains the equation for the maximum osmotic power density:

$$P_{Max} = G_{Osm} \frac{V_{Osm}^2}{4} \times \frac{1}{N_{pore} A_{pore}} \quad (57)$$

In **Fig.70** is presented the maximum osmotic power density obtained by the device whose osmotic current and potential were previously displayed in **Fig.68**

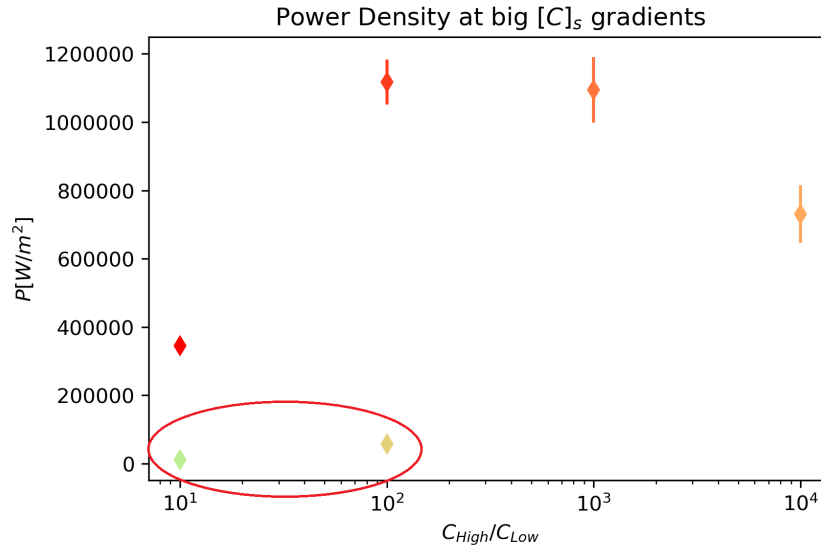


Figure 70: Graph representing the maximum osmotic power density for a Graphite-based TEM drilled device as a function of the concentration ratio. $D = 10nm$, $L = 7nm$. The Red-gradient data points refers to the high concentration region ($c_i = 1M$ and c_o gradually increased). The Green-gradient data points refers to the low concentration region ($c_o = 0.1mM$ and c_i gradually increased)

As expected the maximum generated power density is obtained for a concentration ratio equal to 100 (1M/100mM). The value of $1.1MW/m^2$

or 176 pW per nanopore is outstanding. What we obtained is directly comparable to the best results obtained by Feng J. et al. with MoS_2 nanopore, two orders of magnitude higher than the hBN nanotubes²¹ and several orders if compared with classical RED systems based on alternative exchange membranes⁸⁴.

The last figure of merit to present is the power generation efficiency η . Fair and Osterle²⁸ theorized that nanopore's η can be expressed as the ratio between the energy in output from the system and the energy used as input to perturb it. In this case it is possible to consider the output energy as the harvestable electric power, whilst the input energy as the Gibbs free energy of mixing. In other words only the part of the current coming in the form of net diffusion may be harvested into electrical work. This further remarks that the **selective** transport of ion is a key parameter that will be represented by the transference number.

$$\eta = \frac{dW}{dG} = \frac{V \times I}{(J_+ + J_-)RT \ln \left(\frac{\lambda_i c_i}{\lambda_o c_o} \right)} \quad (58)$$

with J_+ and J_- being respectively the cation and anion current's fluxes.

At this point if one define the transference number t as the value that represent if the ionic current is cation ($t > 0.5$) or anion ($t < 0.5$) sustained, and consider **Eq.36**, the resulting maximum osmotic power generation efficiency can be expressed as:

$$\eta_{max} = \frac{(2t - 1)^2}{2} \quad (59)$$

In **Fig.71** is showed the related result.

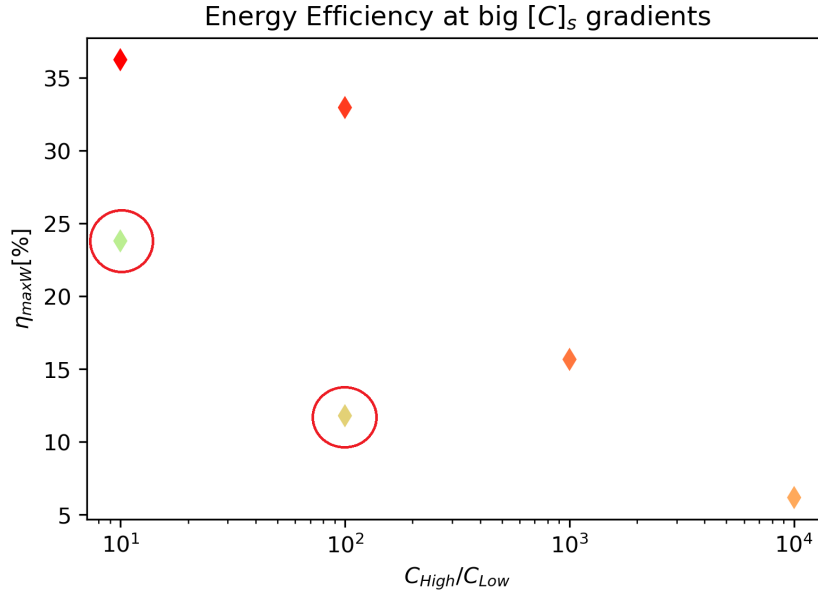


Figure 71: Graph representing the maximum osmotic power generation efficiency for a Graphite-based TEM drilled device as a function of the concentration ratio. $D = 10\text{nm}$, $L = 7\text{nm}$. The Red-gradient data points refers to the high concentration region ($c_i = 1\text{M}$ and c_o gradually increased). The Green-gradient data points refers to the low concentration region ($c_o = 0.1\text{mM}$ and c_i gradually increased)

It is possible to see that the energy efficiency related to the salt concentration ratio at which the device generates the highest osmotic power density is equal to 34%. Also this value results comparable if not even higher than the state-of-the-art monolayer MoS_2 nanopore.²²

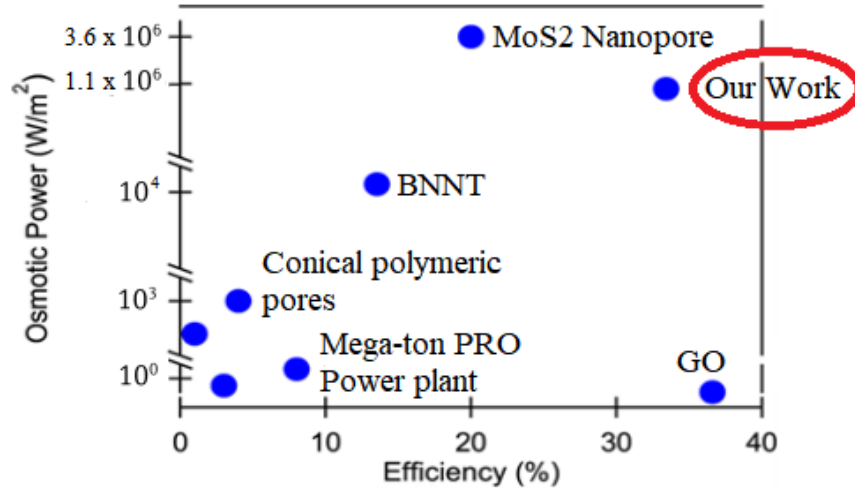


Figure 72: Comparison between power generation vs power generation efficiency for different nanofluidic systems. BNNT stands for "Boron Nitride nanotube", GO is the acronym for Graphene Oxide.

5.3.2 Pressure-Driven ionic transport

The last experiment useful to probe ionic transport, which by rights is not directly linked to the power generation analysis, involves the application of a pressure gradient all along the nanopore length. Indeed, it was explained in **3.2.1** and showed through experimental examples, that charged nanopores break the system electroneutrality creating a charged cloud of ions with opposite charge. Under this perspective it is thus not difficult to imagine that, as it is done applying a potential drop, pressure-driven liquid flow can drag that charged cloud of counterions, resulting in a net current generation known as **Streaming Current** (I_{str}). It can be measured with the setup presented in **5.1 (Fig.56)**, with the addition of an Elveflow pressure controller that permits to directly apply a controlled pressure on top side of the device with a custom-made system controlled with Matlab. Since the ions are driven *indirectly* by water, the resulting current is intrinsically small (on the order of the pA), that is why it was also needed to set the built-in analog filter of the patch-clamp system to the lowest value of 1 kHz. In **Fig.73** it is presented the current intensity trace, obtained applying 20 second long pressure steps $\Delta P = 250$ mbar up to reach 1 bar. The reservoir of the system were filled with KCl or NaCl solutions at different

concentrations.

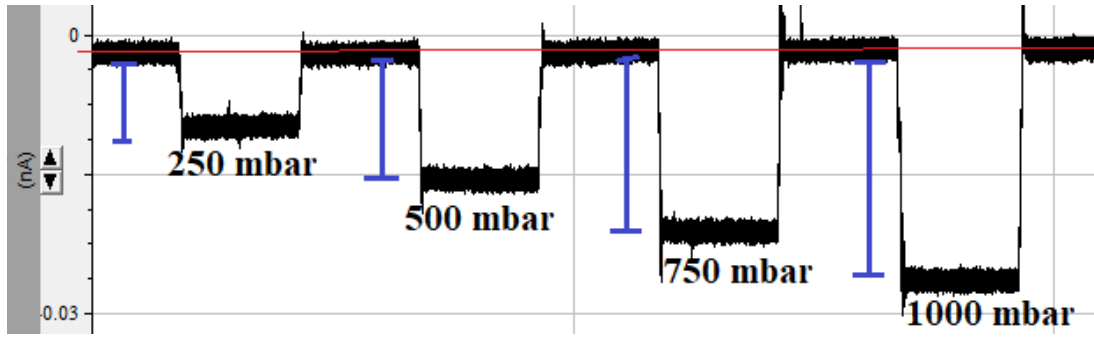


Figure 73: Current intensity trace when applying increasing pressure at fixed pressure drop steps and KCl concentration ($c_h = c_l = 10\text{mM}$). The streaming current (highlighted by the blue intervals) is the additional current generated from the baseline current (highlighted by the red line)

In **Fig.74** is instead showed the net generated $I_{str} - P$ relation per unit of length). The streaming conductance (G_{str}) equal to $G_{str} = I_{str}/\Delta P$, corresponds to the slope of the characteristic times the specific device length (L) and assumes a value that ranges in picoamperes per bar.

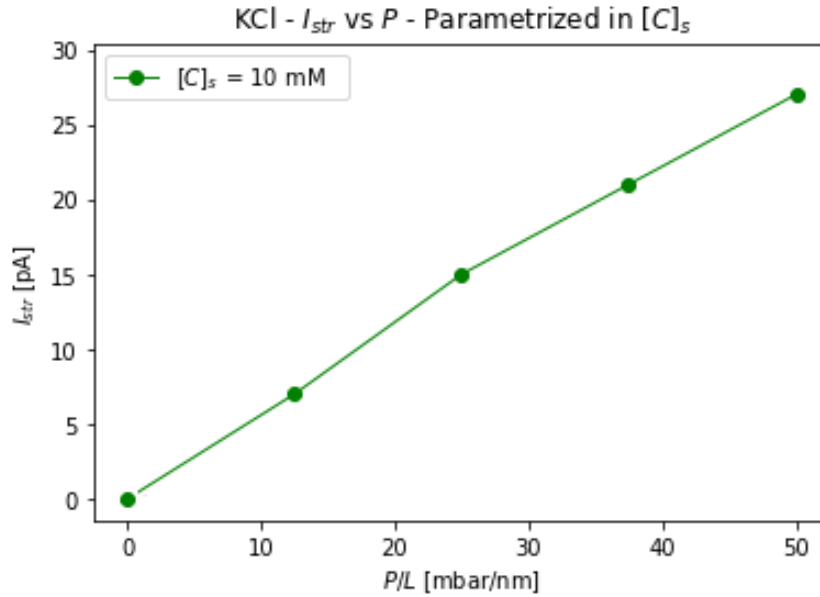


Figure 74: I_{str} vs P per unit of length relation. The device is a TEM drilled nanopore with $D = 10 \text{ nm}$, $L = 20 \text{ nm}$ and resulting $G_{str} = 27 \text{ pA/bar}$

What we obtained with a single TEM drilled pore, in terms of streaming current amplitude, is at least 1 to 2 orders of magnitude higher of what has been obtained in the Angstrom scale slit-shaped nanochannels array.⁸⁵ Probably the streaming current enhancement could be determined by the same processes and effect explained in **5.3**. As a matter of fact if one analyses the results obtained in **Fig.75**, which shows the I_{str} vs C for different applied pressures, one sees that the maximum of the streaming current is obtained with salt concentration within 10 mM and 30 mM.

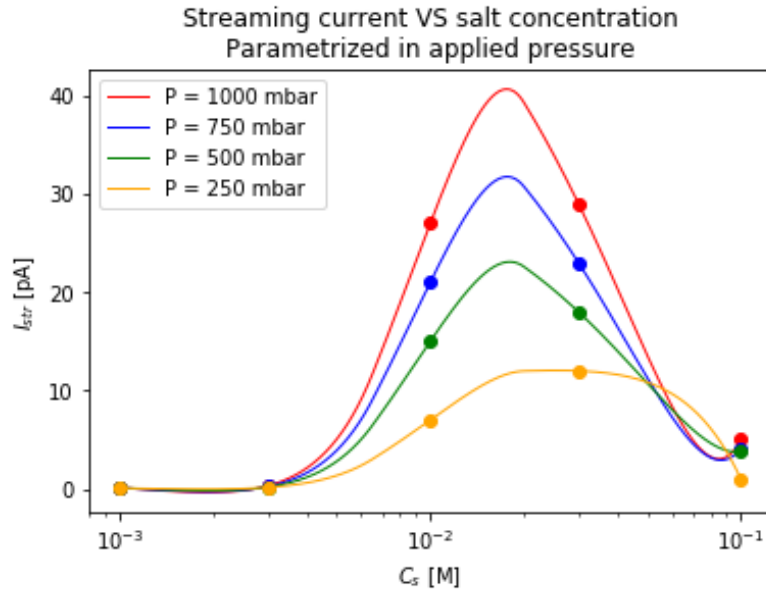
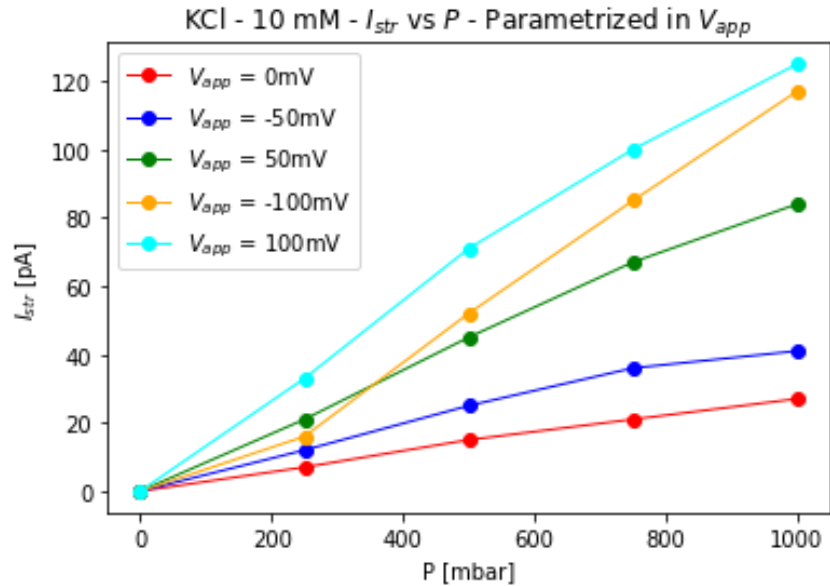


Figure 75: I_{str} vs C_s . The device is a TEM drilled nanopore with $D = 10$ nm, $L = 20$ nm

In this experimental condition the Debye layer overlap occurs (refer to **Tab.2**) and the geometrical properties of the device permits to couple this effect also with a surface conductance process that sustain an easier ionic transport along the nanopore. Instead the lower values obtained at a low or high salt concentration regime may be justified, in the former case by the counterion cloud overspilling and a low availability of ions to sustain the current, whilst in the latter one in a thinned or almost null Debye layer extension over the conduit transverse direction.

As a last investigation it was also analyzed the modulation of an applied voltage on the I-P relation. It was found that applying a higher voltage

drop generates a higher streaming current at the same salt concentration and furthermore this effect is much more marked with respect an increasing salt concentration. These results are presented in **Fig.76**. As shown, what was found indicates that the applied bias voltage, acts as a sort of gating effect for pressure-driven streaming currents, with an enhancement that could reach, in the best case, 2 to 3 orders of magnitude. The results are in line with what has been presented by *Mouterde et al.*⁸⁶ Theoretically this effect is explained by the complicated and subtle interplay that exists within the concentration dependent flow and ionic species profile along the conduit when applying a bias voltage. Making it simple, the application of a potential difference tends to reduce the friction between ions and the inner walls of the nanochannel, thus facilitating the overall ion dragging by means of the application of a pressure difference.



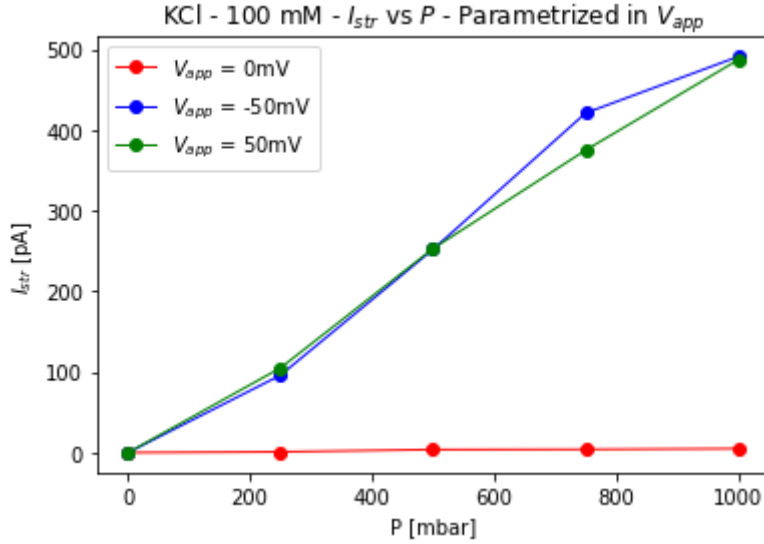


Figure 76: I_{str} vs P parametrized with respect an applied voltage. The device is a TEM drilled nanopore with $D = 10$ nm, $L = 20$ nm. The case presented refers to a 10 mM (upper) and 100 mM (lower) KCl solution.

To further underline the dependence of the measured streaming current on the applied voltage, and how much this effect is intensified by an increasing concentration, **Fig.77** and **Fig.78** are thus presented.

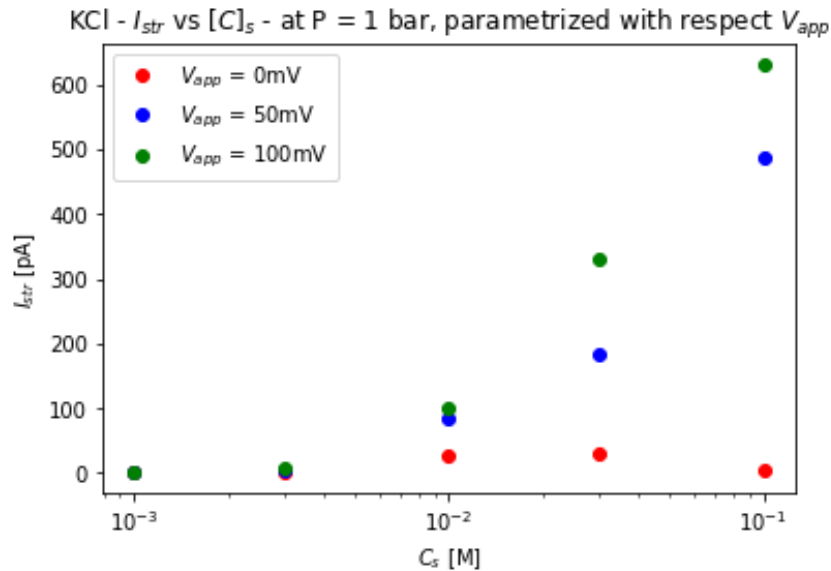


Figure 77: I_{str} vs C at fixed $P = 1$ bar parametrized with respect V_{app} . The device is a TEM drilled nanopore with $D = 10$ nm, $L = 20$ nm. Essentially it shows how the I_{str} - C red curve of Fig.75 is influenced by applying an increasing bias voltage

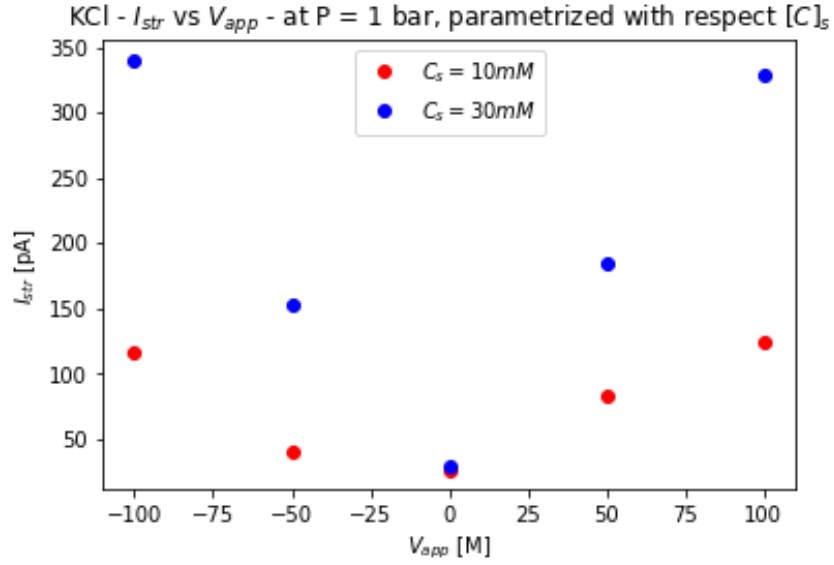


Figure 78: I_{str} vs V_{app} at fixed $P = 1bar$ parametrized with respect C . The device is a TEM drilled nanopore with $D = 10$ nm, $L = 20$ nm. Essentially it shows how much the peak streaming current (**Fig.75**) is influenced by an applied bias voltage at different salt concentrations

The presented results, at the best of my knowledge, represent the first proof-of-concept for a nanopore-based Iontronic pressure sensor. Nevertheless further studies are still needed to properly model and refine such systems.

6 Conclusion

In conclusion, we successfully investigated how the surface properties of 2D materials and the designed nanopore geometry influence the ionic transport and osmotic power generation of the system.

Despite it was the first time approaching such a wide project characterized by a difficult underlying physics, I was able to carry out and go through the whole processes starting from the nanofabrication of those devices, experimenting very different techniques, until their final characterization and analysis of the results, thus acquiring the right mindset that one needs to have when dealing with fundamental research.

The results obtained in the field of the power generation were comparable to the leading devices in the osmotic power generation field reaching ipso facto a state-of-the-art spot as depicted in the following image:

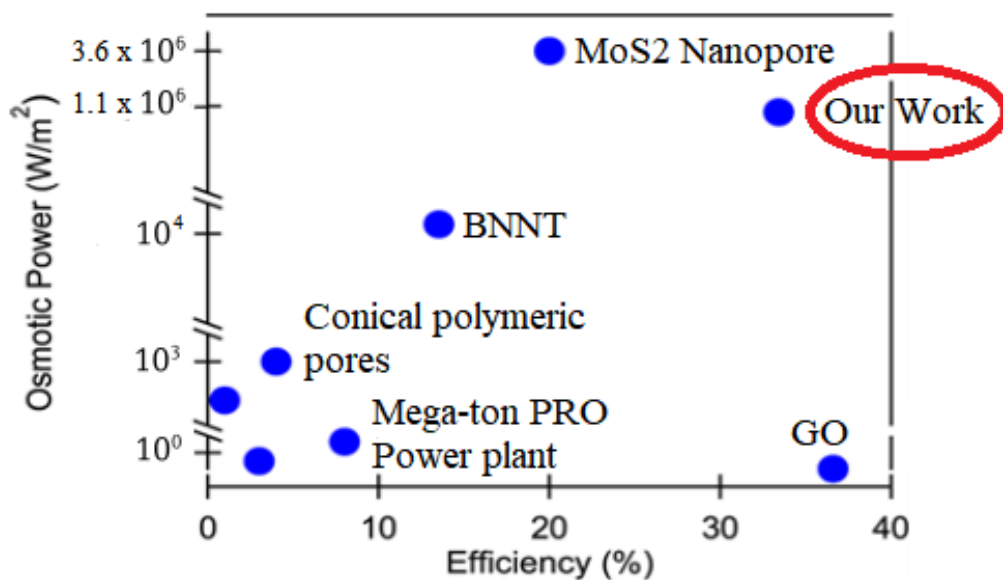


Figure 79: Comparison between power generation vs power generation efficiency for different nanofluidic systems. BNNT stands for "Boron Nitride nanotube", GO is the acronym for Graphene Oxide.

Finally, it is important to know that this project opens the way to a new wide field of research which is still unexplored, furthermore we proved to have a simpler, faster and cheaper way of fabricating nanopore in a repro-

ducible and scalable way. We also built highly selective ionic conductors, nanofluidic diodes and a novel nanofluidic pressure sensor, all fundamental building blocks of the emerging field of iontronics and with an open range of actual applications like: DNA sequencing, nanofluidic transistors, bio-compatible logic circuits or nanopower generators and brain-machine interfacing.

Bibliography

- [1] J. Ellem G. Ward J. Giurco D. Mohr S.H. Wang. “Projection of world fossil fuels by country”. In: *Fuel* 141, 120–135 (2015).
- [2] E. Shafiee S. Topal. “When will fossil fuel reserves be diminished?” In: *Energy Policy* 37, 181–189 (2009).
- [3] “causes-and-solutions-to-the-global-energy-crisis”. In: ().
- [4] J.D Li W.J Fei F. Mai. “A wind-flutter energy converter for powering wireless sensors.” In: *Sensors and Actuators A: Physical*, 173, 1, 163–171 (2012).
- [5] Longnan Li Changheon Han Daejoong Kim Kilsung Kwon Seung Jun Lee. “Energy harvesting system using reverse electro dialysis with nanoporous polycarbonate track-etch membranes”. In: *International Journal Of Energy Research*, 28,4, 530-537 (2013).
- [6] Osorio A. F. Winter C. Alvarez-Silva O. A. “Practical global salinity gradient energy potential”. In: *Renew. Sustain. Energy Rev.* 60, 1387–1395 (2016).
- [7] Tufa R. A. Macedonio F. Curcio E. Drioli E. Ali A. “Membrane technology in renewable-energy-driven”. In: *Nature Reviews — Materials Reviews desalination. Renew. Sustain. Energy Rev.* 81, 1–21 (2018).
- [8] R. J. Isaacs J. D. Seymour. “The ocean as a power resource”. In: *Int. J. Environ. Stud.* 4, 201–205 (1973).
- [9] Veerman J. Hamelers H.V.M Euverink G.J.W Metz SJ Nymeijer K et al. Post J.W. “Salinity-gradient power: evaluation of pressure-retarded osmosis and reverse electro dialysis”. In: *Journal of Membrane Science*, 288, 1-2, 218-230 (2007).
- [10] C. J. N. Schaezle O. Buisman. “Salinity gradient energy: current state and new trends”. In: *Engineering* 1,164–166 (2015).
- [11] K. Tomabechi. “Energy resources in the future”. In: *Energies* 3, 686–695 (2010).

- [12] S. Loeb. “One hundred and thirty benign and renewable megawatts from great salt lake? The possibilities of hydroelectric power by pressure-retarded osmosis”. In: *Desalination* 141, 1, 85-91 (2001).
- [13] G. Cipollina A. Micale. “Sustainable Energy from Salinity Gradients”. In: *Salinity gradient energy*, 1, 1-17 (2016).
- [14] X. Liu Y. Chen. “Mechanical properties of nanoporous graphene membrane”. In: *J. Appl. Phys.* 115, 034303 (2014).
- [15] Brogioli D. Hamelers H. V. M. Nijmeijer K. Yip N. Y. “Salinity gradients for sustainable energy: primer, progress, and prospects.” In: *Environ. Sci. Technol.* 50, 12072–12094 (2016).
- [16] Singh J. Yamamoto N. Dai J. “Mechanical properties of nanoporous graphene membrane”. In: *J. Appl. Phys.* 115, 034303 (2014).
- [17] Kim H. J. Kim D. K. Lee S. W. “Power generation from concentration gradient by reverse electrodialysis in dense silica membranes for microfluidic and nanofluidic systems”. In: *Energies* 9, 49 (2016).
- [18] C.-R. et al. Chang. “Energy conversion from salinity gradient using microchip with Nafion membrane”. In: *Int.J. Mod. Phys. Conf. Ser.* 42, 1660183 (2016).
- [19] Y. M. Kim S. Lee. “Rigid and microporous polymers for gas separation membranes”. In: *Prog. Polym. Sci.* 43, 1–32 (2015).
- [20] J.-C. Ryder M. R. Tan. “Nanoporous metal organic framework materials for smart applications”. In: *Mater. Sci. Technol.* 30, 1598–1612 (2014).
- [21] Siria A. et al. “Giant osmotic energy conversion measured in a single transmembrane boron nitride nanotube”. In: *Nature* 494, 455–458 (2013).
- [22] Graf M. Liu K. et al. Feng J. “Single-layer MoS2 nanopores as nanopower generators”. In: *Nature* 536, 197–200 (2016).
- [23] Fua et al. Yanjun. “An atomically-thin graphene reverse electrodialysis system for efficient energy harvesting from salinity gradient”. In: *Nano Energy*, 57, 783-790 (2019).

- [24] Bocquet M.-L. Bocquet L. Siria A. “New avenues for the large-scale harvesting of blue energy”. In: *Nat. Rev. Chem.* 1, 0091 (2017).
- [25] M. et al. Graf. “Fabrication and practical applications of molybdenum disulfide nanopores”. In: *Nat. Protoc.* 14, 1130–1168 (2016).
- [26] Kuan-A. T. Golovchenko J. A. Rollings R. C. “Ion selectivity of graphene nanopores”. In: *Nat. Commun.* 7, 11408 (2016).
- [27] de Jong-R. M. Saakes M. Metz S. J. Harmsen G. J. Veerman J. “Reverse electrodialysis: comparison of six commercial membrane pairs on the thermodynamic efficiency and power density”. In: *J. Membr. Sci.* 343, 7–15 (2009).
- [28] J. F. Fair J. C. Osterle. “Reverse electrodialysis in charged capillary membranes”. In: *J. Chem. Phys.* 54, 3307–3316 (1971).
- [29] F. et al. Fornasiero. “Ion exclusion by sub-2-nm carbon nanotube pores”. In: *Proc. Natl Acad. Sci. USA* 105, 17250–17255 (2008).
- [30] Smirnov S. Siwy Z. Vlassiuk I. “Ionic selectivity of single nanochannels”. In: *Nano Lett.* 8, 1978–1985 (2008).
- [31] R. B. Schoch A. Plecis and P. Renaud. “Ionic selectivity of single nanochannels”. In: *Nano Lett.*, 2005, 5, 1147–1155 (2005).
- [32] J. C. T. Eijkel and A. van den Berg. In: *Microfluid. Nanofluid.*, 2005, 1, 249–267 (2005).
- [33] E. Charlaix L. Bocquet. “Nanofluidics, from bulk to interfaces”. In: *Chem. Soc. Reviews*, 2009 39, 1073–1095 (1999).
- [34] J. Hendrikse R. B. M. Schasfoort S. Schlautmann and A. van den Berg. In: *Science*, 286, 942 (1999).
- [35] M. Yue D. Li P. Yang R. Karnik R. Fan and A. Majumdar. In: *Nano Lett.*, 5, 943–948 (2005).
- [36] R. Szoszkiewicz U. Landman T.D. Li J. Gao and E. Riedo. In: *Phys. Rev. B: Condens. Matter Mater. Phys.*, 75, 115415 (2007).
- [37] J. Klein U. Raviv. In: *Science*, 295, 1540 (2002).
- [38] E. Helfand. In: *Phys. Rev.*, 119,1. (1960).

- [39] M. Kruithof D. Stein and C. Dekker. In: *Phys. Rev. Lett.*, *93*, 035901 (2004).
- [40] et al. M. Majumder. In: *Nature*, *438*, 44 (2005).
- [41] D. Andelman ed. R. Lipowsky and E. Sackmann. In: *Handbook of Biological Physics ed. Science B.V., vol. 1* (1995).
- [42] R. Fan P. Yang R. Karnik K. Castelino and A. Majumdar. In: *Nano Lett.*, *5*, 1638–1642 (2005).
- [43] J-L. Barrat and L. Bocquet. “Large slip effect at a nonwetting fluid-solid interface”. In: *Phys. Rev. Lett.*, *82*:4671–4674 (1999).
- [44] P. Tabeling C. I. Bouzigues and L. Bocquet. “Nanofluidics in the debye layer at hydrophilic and hydrophobic surfaces”. In: *Phys. Rev. Lett.*, *101*:114503 (2008).
- [45] R. J. Hunter. “Foundations of Colloid Science”. In: *1, 2* (2001).
- [46] Y. Ren and D. Stein. In: *anotechnology*, *19*, 195707 (2008).
- [47] E. Eijkel S. Pennathur and A. Ven der Berg. In: *Lab Chip*, *7*, 1234 (2007).
- [48] Z. Siwy and A. Fulinski. In: *Phys. Rev. Lett.*, *89*, 198103 (2002).
- [49] C.-C. Chang H.-C Yeh and R.-J. Yang. “Reverse electrodialysis in conical-shaped nanopores: salinity gradient-driven power generation”. In: *RSC Adv.*, *4*, 2705 (2014).
- [50] Stein D. Meyer C. Heyden F. H. J. Bonthuis D. J. and Dekker C. In: *Nano Lett.* *7* 1022 (2007).
- [51] Y.-F. Chen D.-K. Kim C. Duan and A. Majumdar. In: *Microfluidics and Nanofluidics*, *9*, 1215–1224 (2010).
- [52] Vishal V. R. Nandigana Aleksandra Radenovic Michal Macha Sanjin Marion. “2D materials as an emerging platform for nanopore-based power generation”. In: *Nature Reviews Materials*, *vol.4*, 588–605 (2019).
- [53] G. Cravotto and P. Cintas. “Sonication-assisted fabrication and post-synthetic modifications of graphene-like materials”. In: *Chemistry–A European Journal*, *16*(18), 5246–5259 (2010).

- [54] S. Park and R. S. Ruoff. “Chemical methods for the production of graphenes”. In: *Nature nanotechnology*, 4(4), 217 (2009).
- [55] P. Avouris and C. Dimitrakopoulos. “Graphene: synthesis and applications”. In: *Materials today*, 15(3), 86–97 (2012).
- [56] W. A. Algozeeb M. G. Stanford C. Kittrell W. Chen R. V. Salvatierra M. Ren E. A. McHugh-P. A. Advincula et al. D. X. Luong K. V. Bets. “Gram-scale bottom-up flash graphene synthesis”. In: *Nature*, 577(7792), 647–651 (2020).
- [57] A. H. Castro Neto K. S. Novoselov D. Jiang R. Yang T. J. Booth A. K. Geim P. Blake E. W. Hill. “Making graphene visible”. In: *Appl. Phys. Lett.* 91, 063124 (2007).
- [58] P. Gant D. P. De Lara P. Jarillo-Herrero R. V. Gorbachev A. Castellanos-Gomez Riccardo Frisenda E. N. Moratalla. “Recent progress in the assembly of nanodevices and van der waals heterostructures by deterministic placement of 2d materials”. In: *Chemical Society Reviews*, 47(1), 53–68 (2018).
- [59] A. Carvalho K. Novoselov A. Mishchenko and A.H. Castro Neto. “2D materials and Van Der Waals heterostructures”. In: *Science*, 353(6298), 9439 (2016).
- [60] C. McMullan D. Branton M. J. Aziz J. A. Golovchenko J. Li D. Stein. “Ion-beam sculpting at nanometre length scales”. In: *Nature*, 412(6843), 166–169 (2001).
- [61] Gaurav Goyal et al. In: *Nanotechnology*, 27, 495301 (2016).
- [62] Song Liu et al. In: *Nanotechnology*, 23, 085301 (2012).
- [63] D.E. Luzzi B.W. Smith. “Electron irradiation effects in single wall carbon nanotubes”. In: *Appl. Phys.*, 90, 3509–15 (2001).
- [64] Q. Xu G. Pandraud C. Dekker H. Zandbergen B. Song G.F. Schneider. “Atomic-scale electron-beam sculpting of near-defect-free graphene nanostructures”. In: *Nano Lett.*, 11, 2247–50 (2011).
- [65] F. Molitor D. Graf T. Ihn K. Ensslin C. Stampfer J. Guttinger. In: *Appl. Phys. Lett.* 2008, 92, 012102 (2008).

- [66] G.H.B Dommett K.M. Kohlhaas E.J Zimney E.A. Stach R.D. Piner S.T. Nguyen R.S. Ruoff S. Stankovich D.A. Dikin. In: *Nature*, 442, 282–286 (2006).
- [67] Marcos Vinicius Surmani Martins Yong Chin Seow Juan Alfredo Guevara Carrio Seunghyun Hong Charlotte Constans and Slaven Garaj. “Scalable graphene-based membranes for ionic sieving with ultrahigh charge selectivity”. In: *Nano letters*, 17(2):728–732 (2017).
- [68] Bert Sakmann and Erwin Neher. “Patch clamp techniques for studying ionic channels in excitable membranes”. In: *Annual review of physiology*, 46(1), 455–472 (1984).
- [69] N. V. Suyazov V. A. Babenko A. A. Sychev N. V. Penkov K. N. Belosludtsev S. V. Gudkov N. F. Bunkin A. V. Shkirin. “Formation and dynamics of ion-stabilized gas nanobubble phase in the bulk of aqueous NaCl solutions”. In: *The Journal of Physical Chemistry B*, 120(7), 1291–1303 (2016).
- [70] M.Y. Wu N.H. Dekker C. Dekker R. M.M. Smeets U.F. Keyser. “Nanobubbles in solid-state nanopores”. In: *Physical Review Letters*, 97(8), 088101 (2006).
- [71] K. Castelino H. Daiguji R. Karnik C. Duan and A. Majumdar. In: *Nano Lett.*, 2007, 7, 547 (2006).
- [72] S. M. Vodyanoy I.; Bezrukov. In: *Biophys. J.*, 62,1011 (1992).
- [73] Smith B. B. Willmott G. R. In: *Nanotechnology*, 23, 088001 (2012).
- [74] Alessandro Siria Anne-Laure Biance Remy Fulcrand Choongyeop Lee Laurent Joly and Lyderic Bocque. “MoS2 or Large Apparent Electric Size of Solid-State Nanopores Due to Spatially Extended Surface Conduction”. In: *Nano Lett.*, 12(8), 4037-44 (2012).
- [75] B. Hille. In: *NJ. Gen. Physiol.*, 51, 199219 (1968).
- [76] J. E. Hall. In: *J. Gen. Physiol.*, 66, 531532 (1975).
- [77] Squires T. M. Khair A. S. In: *J. Fluid Mech.*, 615, 323334 (2008).

- [78] F. C. Wang-A. P. Rooney K. Gopinadhan A. Keerthi A. Mishchenko A. Janardanan P. Blake L. Fumagalli M. Lozada-Hidalgo S. Garaj S. J. Haigh I. V. Grigorieva H. A. Wu A. K. Geim B. Radha A. Esfandiari. “Molecular transport through capillaries made with atomic-scale precision”. In: *Nature*, 538, 222–225 (2016).
- [79] Yanina Cesa-Gregory F. Schneider Amedeo Bellunato Hadi Arjmandi Tash. “Chemistry at the edge of graphene”. In: *ChemPhysChem*, 17(6), 785–801 (2016).
- [80] R.G Bates and J.B Macaskill. “Standard potential of the silver-silver chloride electrode”. In: *Pure Appl. Chem*, 50, 1701–1706 (1978).
- [81] Peter J. Stiles John W. Perram. “On the nature of liquid junction and membrane potentials”. In: *Physical Chemistry Chemical Physics*, 8(36), 4200–4213 (2006).
- [82] David E Goldman. “Potential, impedance, and rectification in membranes”. In: *The Journal of general physiology*, 27(1), 37–60 (1943).
- [83] Hsueh-Chia Chang Sandip Ghosal John D. Sherwood. “Solid-state nanopore hydrodynamics and transport”. In: *Biomicrofluidics* 13, 011301 (2019).
- [84] B. E. Logan and M. Elimelech. “Membrane-based processes for sustainable power generation using water”. In: *Nature* 488, 313–319 (2012).
- [85] Mouterde T. Niguès A. et al. Marcotte A. “Mechanically activated ionic transport across single-digit carbon nanotubes”. In: *Nat. Mater.* 19, 1057–1061 (2020).
- [86] A. r. Poggioli S. A. Dar A. Siria A. K. Geim² L. Bocquet t. Mouterde A. Keerthi² and B. radha. “Molecular streaming and its voltage control in ångström-scale channels”. In: *Nature*, vol. 567, 87–90 (2019).